E pur si muove: Galiliean-invariant cosmological hydrodynamical simulations on a moving mesh

Volker Springel⋆

Max-Planck-Institut für Astrophysik, Karl-Schwarzschild-Straße 1, 85740 Garching bei München, Germany

31 October 2009

ABSTRACT
Hydrodynamic cosmological simulations at present usually employ either the Lagrangian smoothed particle hydrodynamics (SPH) technique, or Eulerian hydrodynamics on a Cartesian mesh with (optional) adaptive mesh refinement (AMR). Both of these methods have disadvantages that negatively impact their accuracy in certain situations, for example the suppression of fluid instabilities in the case of SPH, and the lack of Galilean-invariance and the presence of overmixing in the case of AMR. We here propose a novel scheme which largely eliminates these weaknesses. It is based on a moving unstructured mesh defined by the Voronoi tessellation of a set of discrete points. The mesh is used to solve the hyperbolic conservation laws of ideal hydrodynamics with a finite volume approach, based on a second-order unsplit Godunov scheme with an exact Riemann solver. The mesh-generating points can in principle be moved arbitrarily. If they are chosen to be stationary, the scheme is equivalent to an ordinary Eulerian method with second order accuracy. If they instead move with the velocity of the local flow, one obtains a Lagrangian formulation of continuum hydrodynamics that does not suffer from the mesh distortion limitations inherent in other mesh-based Lagrangian schemes. In this mode, our new method is fully Galilean-invariant, unlike ordinary Eulerian codes, a property that is of significant importance for cosmological simulations where highly supersonic bulk flows are common. In addition, the new scheme can adjust its spatial resolution automatically and continuously, and hence inherits the principal advantage of SPH for simulations of cosmological structure growth. The high accuracy of Eulerian methods in the treatment of shocks is also retained, while the treatment of contact discontinuities improves. We discuss how this approach is implemented in our new code AREPO, both in 2D and 3D, and is parallelized for distributed memory computers. We also discuss techniques for adaptive refinement or derefinement of the unstructured mesh. We introduce an individual time-step approach for finite volume hydrodynamics, and present a high-accuracy treatment of self-gravity for the gas that allows the new method to be seamlessly combined with a high-resolution treatment of collisionless dark matter. We use a suite of test problems to examine the performance of the new code and argue that the hydrodynamic moving-mesh scheme proposed here provides an attractive and competitive alternative to current SPH and Eulerian techniques.

Key words: methods: numerical – galaxies: interactions – cosmology: dark matter

1 INTRODUCTION

Numerical simulations have become an indispensable tool to study astrophysical problems of structure formation. They are the method of choice to predict the fully non-linear outcome of the well-specified initial conditions of the standard ΛCDM cosmology. In fact, they have played an instrumental role to establish the viability of the standard cosmogony, and continue to be of crucial importance for theoretical research on galaxy formation.

When only dark matter is considered, the current generation of cosmological codes have reached a high-degree of accuracy, allowing an impressive dynamic range in high-resolution studies of dark matter clustering. There is now a consensus emerging in the field about important key results, such as the central dark matter density profile of col-

⋆ E-mail: volker@mpa-garching.mpg.de

lapsed halos (Navarro et al., 2008; Stadel et al., 2009). This is important progress, which is in part due to the fact that there is little doubt about what is required to achieve high accuracy in collisionless simulations; this is simply an accurate gravitational force calculation (which can be easily and objectively tested), accurate time integration (also easy to check) and use of a large number of particles (to make the collisionless dynamics more faithful, and resolve smaller scales).

However, the situation is different for hydrodynamic cosmological simulations. Here a variety of fundamentally quite different numerical methods are in use, the most prominent ones are Lagrangian smoothed particle hydrodynamics (SPH; Lucy, 1977; Gingold & Monaghan, 1977; Monaghan, 1992) and Eulerian mesh-based hydrodynamics (e.g. Stone & Norman, 1992) with or without adaptive mesh refinement (AMR; Berger & Colella, 1989), but also more exotic schemes have been proposed, such as treating hydrodynamics through an approximation of the *collisional* Boltzmann equation (Xu, 1997; Slyz & Prendergast, 1999). An issue of great concern is that these methods sometimes yield conflicting results even for basic calculations that only consider non-radiative hydrodynamics (e.g. Agertz et al., 2007; Tasker et al., 2008; Mitchell et al., 2009). Perhaps the most famous example is the Santa Barbara cluster comparison project (Frenk et al., 1999), and the systematic offsets in the core entropy that are apparently produced between SPH and AMR codes. The right answer to this problem is presently still unclear (but see Mitchell et al., 2009, for some hints). This uncertainty compromises the trust one would like to have in the predictive power of ab-initio hydrodynamical cosmological simulation, especially when applied to the full problem of galaxy formation, where additional processes such as radiative cooling, star formation and feedback must be included. The latter bring about significant additional complexity, and further extend the dynamic range that needs to be addressed.

It has become clear over recent years that both SPH and AMR suffer from fundamental problems that make them inaccurate in certain regimes. SPH codes have comparatively poor shock resolution, and offer only low-order accuracy for the treatment of contact discontinuities. Worse, they appear to suppress fluid instabilities under certain conditions (Agertz et al., 2007), as a result of a spurious surface tension and inaccurate gradient estimates across density jumps. While it is possible to alleviate these effects by introducing artificial heat conduction or mixing terms (Price, 2008; Wadsley et al., 2008), or a modified treatment of the artificial viscosity (Dolag et al., 2005), it is still unclear whether any of these suggestions provides a universal solution that generally improves the results without introducing significant problems in other situations. In any case, the absence of any entropy production through mixing in SPH, as particularly apparent in the entropy-formulation of SPH (Springel & Hernquist, 2002), is an important conceptual difference to Eulerian codes, where entropy is implicitly produced when fluxes with different thermodynamic state are mixed together in a single cell.

Eulerian methods are the traditional method to solve the system of hyperbolic partial differential equations that constitute ideal hydrodynamics. There are decades of experience with these methods in computational fluid dynamics,

and accurate Godunov schemes exist which offer high-order spatial accuracy, have negligible postshock oscillations, and low numerical diffusivity. However, fundamental problems remain with these methods as well. Perhaps the most serious one is their lack of Galilean-invariance, making the results sensitive to the presence of bulk velocities (e.g. Wadsley et al., 2008; Tasker et al., 2008). This is a source of substantial concern in simulations of galaxy formation, where galaxies move with large speeds relative to each other, speeds that are often orders of magnitude larger than the sound speed of the dense interstellar medium that one wants to follow hydrodynamically. Similarly, it is also challenging with AMR to follow a highly refined region that moves with large velocity relative to the reference frame adopted for the calculation as a whole, because refinement criteria that correctly 'anticipate' the motion of a system across a grid are difficult to construct.

Another concern lies in the mixing inherent in multidimensional Eulerian hydrodynamics. This provides for an implicit source of entropy, with sometimes unclear consequences, a situation that prompted Wadsley et al. (2008) to propose an explicit modeling of the mixing through additional terms in the fluid equations. Even though it is clear that some mixing helps and provides a dissipation scale for the finite resolution, there may well be overmixing if the resolution is limited or the bulk velocities are large. Also, it is rather unclear whether the turbulent cascades that actually happen in nature are correctly captured if the AMR hierarchy is truncated at a certain maximum refinement level (Iapichino et al., 2008; Iapichino & Niemeyer, 2008). It has been suggested that this can lead to unphysical solutions for fluid instabilities like the Rayleigh-Taylor instability, and that recovery of the correct behaviour requires subresolution models for turbulence (Scannapieco & Brüggen, 2008). In any case, the different treatment of mixing is arguably the most fundamental difference between SPH and AMR (see also Trac et al., 2007; Mitchell et al., 2009).

It has also become clear that current cosmological AMR codes presently in use have problems to accurately treat structure formation driven by gravitational instability (O'Shea et al., 2005; Heitmann et al., 2008). This happens because it is quite difficult to refine 'early enough' on *all* the many small density fluctuations that grow at high redshift, and if a refinement is placed, the resolution increases *discontinuously* by a factor of 2 per dimension. In typical calculations, this introduces a subtle suppression of the growth of small halos, such that the halo mass functions show a deficit of small halos at late times. The AMR approach is therefore not ideal for a high accuracy treatment of the N-body problem posed by cosmic structure; only when very fine base meshes and conservative refinement criteria are adopted, do AMR results approximatively recover those obtained comparatively easily by SPH codes, which treat self-gravity in a Lagrangian fashion, and do not have discontinuous jumps in resolution.

As has long been recognized, Eulerian methods have also problems to properly resolve flows where the kinetic energy is much larger than the thermal energy, and both the pre- and postshock gas move supersonically with respect to the grid. This situation is ubiquitous in cosmological applications, and prompted the development of schemes that try to circumvent the problem when necessary, such as the

'dual energy formalism' (Bryan et al., 1995) or schemes that evolve a conservation law for the entropy outside of shocks (Ryu et al., 1993). Usage of such schemes usually means that exact energy conservation is sacrificed in favour of a more accurate treatment of the gas entropy. The need for such fixes is in part a consequence of the choice of a fixed reference frame for describing the flow, and hence is related to the Galilean non-invariance of the Eulerian treatment. Indeed, there have been attempts to solve the bulk-flow problem by formulating the equations such that a more natural reference frame can be adopted. In particular, Trac & Pen (2004) developed a special method where a frame change is introduced when the gas-dynamical equations are coupled to self-gravity. The frame velocity is estimated based on a smoothed large-scale velocity field. This relatively simple approach can reduce the artefacts stemming from large bulk flows, but it does not really render the results invariant of the original reference frame and therefore does not provide a complete solution for the non-Galilean invariance of the underlying Eulerian approach.

A more radical approach is to let the mesh itself move. This is an obvious and old idea, but one fraught with many practical difficulties that have so far prevented any widespread use in astrophysics and cosmology. There have been a number of attempts that seemed promising however. In particular, Whitehurst (1995) presented his first order accurate code FLAME for hydrodynamics based on Delaunay and Voronoi tessellations and his 'signal method' which was able to perform quite well on a number of test problems. Unfortunately no practical applications followed.

Gnedin (1995) and Pen (1998) have presented moving mesh hydrodynamic algorithms that have successfully been applied to a range of cosmological problems. Their methods rely on the continuous deformation of a Cartesian grid. However, the need to limit the maximum grid distortions severely limits the flexibility of the codes for situations in which the mesh becomes heavily distorted, and special measures were required to let the codes evolve cosmological density fields into a highly clustered state. For example, Gnedin (1995) addressed this by letting an Eulerian solver take over in regions where the Lagrangian approach fails due to severe mesh distortions. In general, mesh tangling (manifested in 'bow-tie' cells and hourglass like mesh motions) is the traditional problem of multi-dimensional Lagrangian hydrodynamics. In arbitrary Lagrange-Eulerian (ALE) approaches, remapping techniques to more regular meshes are used to counteract the deteriorating influence of mesh distortions, allowing the calculation to continue past the point where it would otherwise be stopped by mesh twisting. The remapping is a diffusive operation, however, and the task to automatically construct 'good' new regularized meshes is very challenging in general. This appears to have impaired widespread adoption of ALE techniques in astronomy thus far, apart from notable exceptions in stellar astrophysics (Murphy & Burrows, 2008).

Another interesting study directly related to our approach was that of Xu (1997), who presented an N-body and hydro-solver on an *unstructured*, fixed mesh. This work used a Delaunay tessellation, and the hydrodynamic scheme was formulated based on a gas-kinetic approach, with the goal to apply it to cosmological simulations of structure formation. However, the method appears to have not been investigated much further afterwards (except for an unpublished master thesis by M. Ruetalo, U. of Toronto, privately communicated to us by J. R. Bond). We note that unstructured triangular meshes are regularly used in engineering applications, however often in the context of stationary flows, for example around airplane foils (see Mavriplis, 1997, for a review).

We here propose a new formulation of continuum hydrodynamics based on an unstructured mesh. The mesh is defined as the Voronoi tessellation of a set of discrete mesh-generating points, which are in principle allowed to move freely. We show how a finite-volume hydrodynamic scheme with the Voronoi cells as principle control volumes can be consistently defined. Most importantly, due to the mathematical properties of the Voronoi tessellation, the mesh continuously deforms and changes its topology as a result of the point motion, without ever leading to the dreaded mesh-tangling effects that are the curse of traditional ALE methods. Our method therefore retains the principal advantage of the mesh-free SPH approach: It offers free and unrestricted, continuous adjustment of its resolution to local clustering. In addition, we show that our new method is Galilean invariant when the mesh is moved along with the flow. There are no preferred directions in it, unlike in Cartesian grids. Thanks to its Lagrangian nature, mesh refinement is normally not needed when one wants to maintain roughly constant mass resolution, but if desired, the Voronoi mesh may also be adaptively refined or derefined.

With these properties, the moving-mesh approach represents a compromise between SPH and AMR. It inherits the automatic adaptivity, geometric flexibility and Galilean invariance of SPH, while it shares the high-accuracy treatment of shocks, shear waves, and fluid instabilities, as well as the low noise and the absence of artificial viscosity, with AMR. A further advantage of the method lies in its ability to easily handle boundary conditions at curved surfaces that can be stationary, move with the flow, or are governed by a prescribed velocity field. We also show how the method can be made adaptive in time by means of individual timesteps, and how it can be coupled to a high-resolution gravitational solver (a TreePM scheme) that gets around the problems experienced by the current generation of AMR codes in cosmological structure formation calculations. We think this makes the new code AREPO* that we built with this approach a very interesting and competitive method for future applications in cosmology, as well as in other fields.

We demonstrate the performance of AREPO in a number of test problems, which include purely hydrodynamical tests in 1D, 2D, and 3D, as well as simulations where self-gravity is included. We also present comparisons with the state-of-the-art Eulerian code ATHENA (Stone et al., 2008), both to validate our hydrodynamic algorithms, and to discuss issues of Galilean (non)invariance. Because our scheme relies on Voronoi meshes, it is very important to develop algorithms that are able to construct the mesh rapidly and robustly on distributed memory platforms. We will therefore

---

* Named after the enigmatic word AREPO in the Latin palindromic sentence *sator arepo tenet opera rotas*, the 'Sator Square'.

discuss in some detail the solutions we have developed for this problem.

This paper is structured as follows. In Section 2, we discuss our mesh generation algorithms, both in 2D and 3D. In Section 3, we then formulate continuum hydrodynamics on the Voronoi mesh, based on a finite-volume ansatz and a second-order accurate extension of Godunov's method. In Section 4, we discuss how the mesh motion can be steered to maintain constant mass or volume per cell, or to improve mesh regularity. Our treatment of self-gravity is described in Section 5, and the refinement or de-refinement of the unstructured mesh in Section 6. In Section 7, we outline our methods for time-integration, in particular the use of individual timesteps, and we describe the basic architecture of our new simulation code. We then turn to an extensive discussion of test problems, including pure hydrodynamical tests in Section 8, and tests that include the gravitational effects from the gas itself and from a collisionless dark matter component in Section 9. Finally, we summarize and discuss our findings in Section 10.

2   GENERATING DELAUNAY AND VORONOI MESHES

For a given set of points, a Voronoi tessellation of space consists of non-overlapping cells around each of the sites such that each cell contains the region of space closer to it than any of the other sites. This definition holds both in 2D and 3D, and can be readily extended to higher dimensions if desired. A direct consequence of this definition is that the cells are polygons in 2D and polyhedra in 3D, with faces that are equidistant to the mesh-generating points of each pair of neighbouring cells.

Closely related to the Voronoi tessellation is the Delaunay tessellation, which is in fact the topological dual of the Voronoi diagram. In 2D, the Delaunay tessellation for a given set of points is a triangulation of the plane, where the points serve as vertices of the triangles. The defining property of the Delaunay triangulation is that each circumcircle around one of the triangles of the tessellation is not allowed to contain any of the other mesh-generating points in its interior. This *empty circumcircle* property distinguishes the Delaunay triangulation from the many other triangulations of the plane that are possible for the point set. Furthermore, this condition *uniquely* determines the triangulation for points in general position. Similarly, in three dimensions, the Delaunay tessellation is formed by tetrahedra that are not allowed to contain any of the points inside their circumspheres.

As an example, we show in Figure 1 the Delaunay and Voronoi tessellations for a small set of points in 2D, enclosed in a box with imposed periodic boundary conditions. The midpoints of the circumcircles around each Delaunay triangle form the vertices of the Voronoi cells, and for each line in the Delaunay diagram, there is an orthogonal face in the Voronoi tessellation. This topological duality also holds in 3D, where each edge of a tetrahedron lies orthogonal to a face of a Voronoi polyhedron.

Delaunay and Voronoi tessellations are basic constructions in computational geometry, and numerous mathematical properties are known for them (Okabe et al., 2000). For example, the Delaunay triangulation maximises the minimum angle among all possible triangulations for a given point set. For points in general location, the Delaunay and Voronoi tessellations are unique. If there exist circles with more than 3 points on them (or spheres with more than 4 points in 3D), the Delaunay triangulation contains degenerate cases where the triangulation may flip by an infinitesimal motion of one of the points. Note however that the Voronoi tessellation is still unique in this case. In fact, an edge between two degenerate points of the Delaunay triangulation has a dual Voronoi area of zero size. Nevertheless, degeneracies can be a significant problem for the robustness of mesh-construction algorithms, an issue we will discuss in more detail later on.

There is a sizable body of literature in computational geometry on algorithms for constructing the Delaunay and Voronoi tessellations. It is in general much easier to construct the Delaunay tessellation and obtain the Voronoi tessellation from it, instead of trying to directly construct the Voronoi tessellation. The Voronoi construction hence effectively reduces to the problem of constructing the Delaunay triangulation, an approach we will also follow here.

The different construction algorithms for the Delaunay triangulation include:

(i) incremental insertion,
(ii) projection of the convex hull of a higher dimensional embedding,
(iii) recursive subdivision (divide & conquer),
(iv) direct incremental construction,
(v) improving an arbitrary triangulation by flipping.

Incremental insertion due to Bowyer (1981) and Watson (1981) is conceptionally the simplest approach. Here one starts with a valid tessellation, inserts an additional point, and then repairs the mesh locally by 'flipping' triangles/tetrahedra to restore Delaunayhood (see below). It can be shown that the worst case behaviour for this method (for unfavourable input particle sets) scales as N^2, but in practice, the observed scaling is much better. In fact, for point sets in general location which are added to the tessellation in random order, a scaling of $N \log N$ is reached.

Another interesting method is obtained by adding an additional coordinate to the point set, $r^2 = x^2 + y^2 + z^2$, which effectively produces a higher dimensional embedding of the form of a paraboloid. The convex hull of this lifted point set yields the Delaunay triangulation when projected down onto the original lower dimensional space. This method hence reduces the Delaunay triangulation to the problem of finding the convex hull in n-dimensional space, for which the *quickhull* algorithm can be used.

In two dimensions, the fastest algorithm is based on a divide and conquer strategy, as proposed by Guibas & Stolfi (1985) and refined by Dwyer (1987). Here the point set is recursively subdivided, until a single triangle can be constructed. These sets are then merged along the dividing lines. Unfortunately, this elegant approach is difficult to implement in three dimensions, primarily because of the difficulty of constructing a two-dimensional merging phase along the dividing planes. Cignoni et al. (1998) overcame this problem in the *Dewall* algorithm, essentially by reversing the order of the split and merge steps. These authors first construct a "wall" of Delaunay triangles directly, which
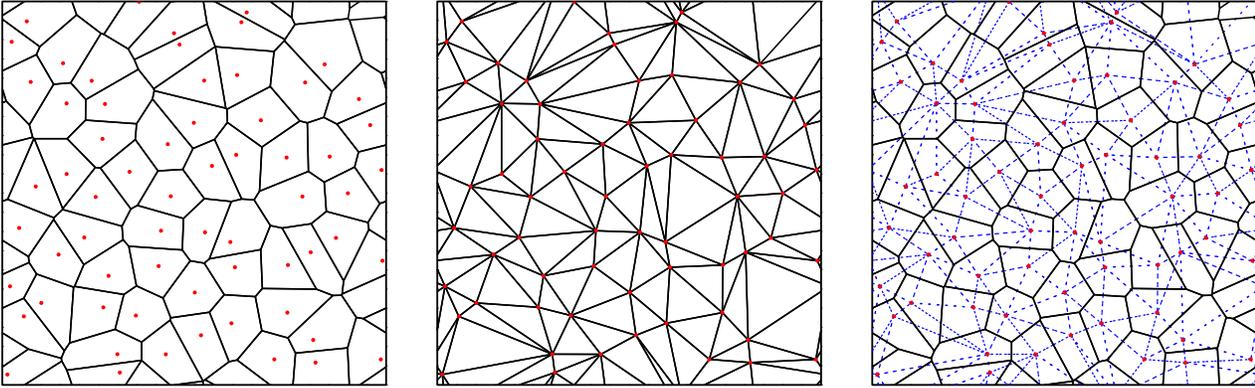
Figure 1. Example of a Voronoi and Delaunay tessellation in 2D, with periodic boundary conditions. The panel on the left shows the Voronoi tessellation for $N = 64$ points (shown as red circles), the panel in the middle gives the corresponding Delaunay tessellation, while the panel on the right shows both simultaneously (solid lines show the Voronoi, dashed lines the Delaunay tessellation).

splits the tessellation into two halfs; those can then be processed recursively in turn.

Direct incremental construction techniques start out from one Delaunay edge, and then find the correct point that completes it to form a Delaunay triangle. This has been used by van de Weygaert (1994), for example, who applied Voronoi tessellations for a statistical analysis of cosmic structures (a comprehensive dicussion and overview about this topic is given by van de Weygaert & Schaap, 2009).

Finally, the flipping method starts from an arbitrary triangulation, and then tries to give it the Delaunay property by local changes in the triangulation ("flips"). In 2D, it can be shown that this can always succeed through simple flips of edges between two adjacent triangles. However, in 3D, one may get get stuck with tetrahedralizations that are not flipable into the correct Delaunay triangulation. While this may appear as a show stopper for incremental insertion algorithms in 3D, Edelsbrunner & Shah (1996) have shown that this is not the case. Provided one starts with a valid Delaunay triangulation, local flips can always restore Delaunayhood after a further point has been inserted into the mesh, so that the incremental insertion strategy is actually a robust algorithm also for the three-dimensional case.

We use the incremental insertion strategy in our new hydrodynamical code. It is among the fastest known algorithms, and most importantly for us, it allows implementing our particular parallelization strategy for distributed memory machines, which requires that additional points from other processors can be easily added to an existing local tessellation. This task can not be readily accomplished with the other tessellation approaches, where normally the full point set needs to be known already at the start of the tessellation procedure.

We illustrate the sequential insertion algorithm in Figure 2. Starting from a valid Delaunay tessellation, the new point first needs to be located in one of the triangles (or tetrahedra in 3D), a problem we shall discuss further below. After this first step, the identified triangle is then subdivided into 3 triangles by inserting the point, yielding a new triangulation. However, one or several of the new triangles may now violate the *empty circumcircle* criterion. We note

that the latter can also be formulated for individual edges; we say an edge is a *Delaunay edge* if there exists a circle through both of its endpoints which does not contain any other point in its interior. It can be shown that if an edge is Delaunay, it is part of the correct Delaunay triangulation. It is easy to show that the three edges around the newly inserted point are Delaunay, but the opposite edges may have lost this property as a result of the insertion (marked in red in 'Step 2' of Fig. 2). These edges must be tested in turn using the in-circle criterion. If a violating edge is found (Step 4), it is flipped in the quadrilateral formed by the two adjacent triangles. This produces two more edges that may now have lost the Delaunay property, and which lie again opposite of the inserted point. These edges are added to the list of edges that need to be tested with the in-circle criterion. The algorithm continues until this list is exhausted, at which point the new site has been successfully inserted, and a new valid Delaunay triangulation has been obtained.

To make sure that every point that needs to be inserted always lies in a triangle to begin with, we start the tessellation procedure with a fiducial large triangle enclosing the whole system. Especially in 3D dimensions, this simplifies the algorithms enormously, as the difficult case of an insertion of a point outside of the convex hull of the current tessellation does not have to be dealt with.

In practice, we will always use periodic or reflecting boundaries that are realized with a layer of *ghost cells* (see below). The enclosing triangle is chosen large enough that both the primary simulation domain and the ghost region are enclosed in its interior, such that the enclosing triangle's shape or orientation does not influence the used part of the final tessellation in any way.

The geometric in-circle test can be formulated compactly in terms of an evaluation of a determinant. For example, in 2D, the in-circle test is given by

$$T_{\mathrm{InCircle}}(\boldsymbol{a}, \boldsymbol{b}, \boldsymbol{c}, \boldsymbol{d}) = \begin{vmatrix} 1 & a_x & a_y & a_x^2 + a_y^2 \\ 1 & b_x & b_y & b_x^2 + b_y^2 \\ 1 & c_x & c_y & c_x^2 + c_y^2 \\ 1 & d_x & d_y & d_x^2 + d_y^2 \end{vmatrix} =$$
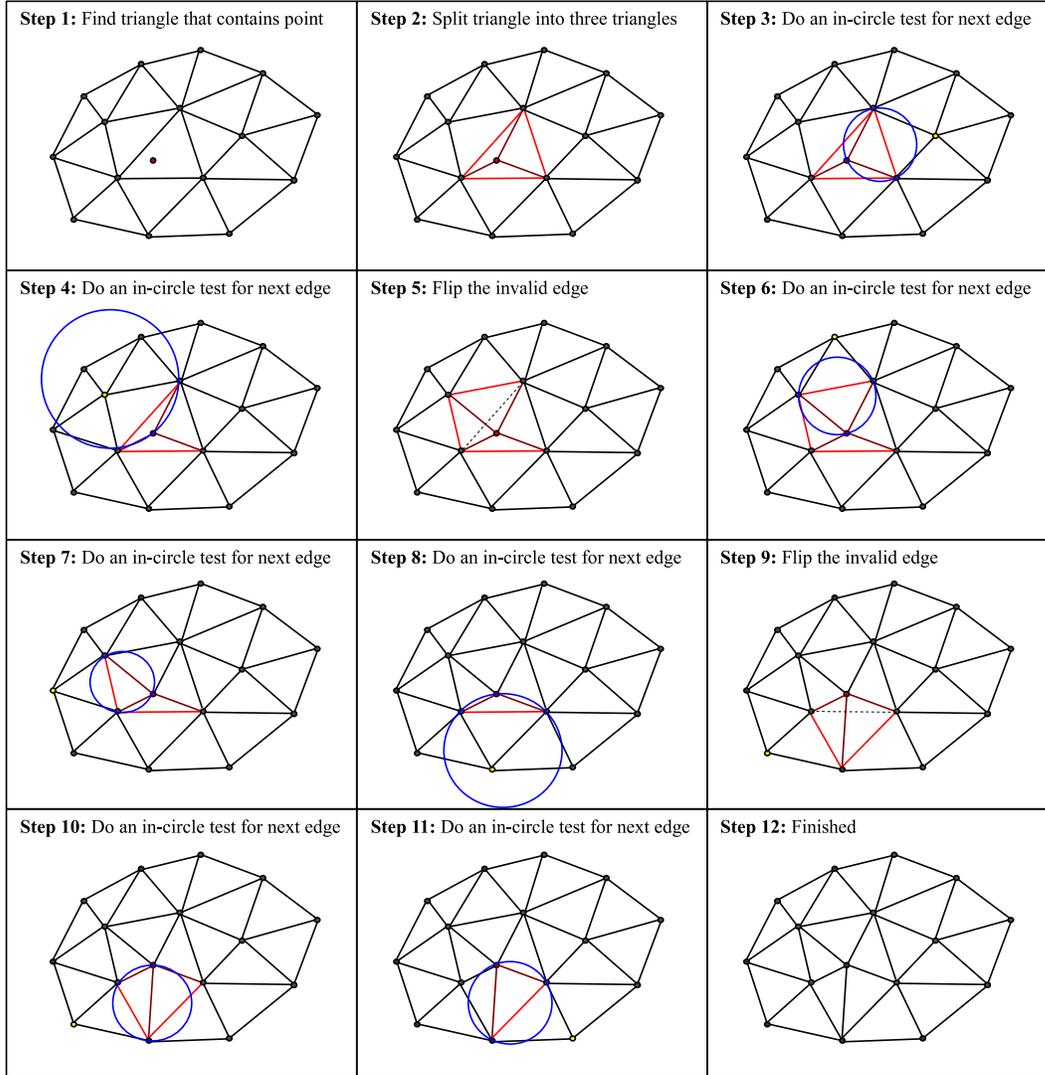
Figure 2. The point insertion algorithm in 2D. We start with a valid Delaunay triangulation in which we want to insert an additional point. We first locate the triangle containing the point (step 1), then split it into three triangles (step 2). The edges (drawn in red) in the new triangles opposite of the inserted point may violate the in-circle criterion and need to be tested individually. If an edge is Delaunay (step 3), it is part of the final tessellation, but if it violates the in-circle criterion (step 4), the edge needs to be flipped in the quadrilateral formed by the adjacent triangles (step 5). The flip generates additional edges that need to be tested (steps 6 and 7). Any violating edge found (e.g. step 9) needs to be corrected by flips. Once all remaining new edges are validated (steps 10 and 11), we arrive again at a valid Delaunay tessellation (step 12).

$$\left| \begin{array}{ccc} b_x - a_x & b_y - a_y & (b_x - a_x)^2 + (b_y - a_y)^2 \\ c_x - a_x & c_y - a_y & (c_x - a_x)^2 + (c_y - a_y)^2 \\ d_x - a_x & d_y - a_y & (d_x - a_x)^2 + (d_y - a_y)^2 \end{array} \right|. \quad (1)$$

Provided the triangle $(\boldsymbol{a}, \boldsymbol{b}, \boldsymbol{c})$ is positively oriented, this gives $T_{\mathrm{InCircle}}(\boldsymbol{a}, \boldsymbol{b}, \boldsymbol{c}, \boldsymbol{d}) < 0$ if the point $\boldsymbol{d}$ lies inside the circumsphere of the triangle, and $T_{\mathrm{InCircle}}(\boldsymbol{a}, \boldsymbol{b}, \boldsymbol{c}, \boldsymbol{d}) > 0$ if the point is outside. $T_{\mathrm{InCircle}}(\boldsymbol{a}, \boldsymbol{b}, \boldsymbol{c}, \boldsymbol{d}) = 0$ corresponds to the interesting case that $\boldsymbol{d}$ lies exactly on the circumsphere of the triangle. It turns out that correct detection of this degenerate case is problematic in the light of finite floating point precision on a computer, but crucial for the stability of the mesh-generating algorithm, an issue which we shall discuss further below.

The orientation of a triangle can also be established

with a determinant, through

$$T_{\mathrm{Orient2D}}(\boldsymbol{a}, \boldsymbol{b}, \boldsymbol{c}) = \left| \begin{array}{ccc} 1 & a_x & a_y \\ 1 & b_x & b_y \\ 1 & c_x & c_y \end{array} \right| = \left| \begin{array}{cc} b_x - a_x & b_y - a_y \\ c_x - a_x & c_y - a_y \end{array} \right|. \quad (2)$$

A positive value indicates positive orientation. Internally, we always store the triangles/tetrahedra of our Delaunay triangulation such that they are positively oriented, which minimizes the required number of orientation tests.

In three dimensions, the incremental construction algorithm works very similarly, apart from a few additional complications. Briefly, when a point is inserted, we now need to carry out a '1-to-4 flip', i.e. we replace the insertion tetrahedron by four new tetrahedra, as illustrated in Figure 3. Just as in 2D, this can render tetrahedra that share a
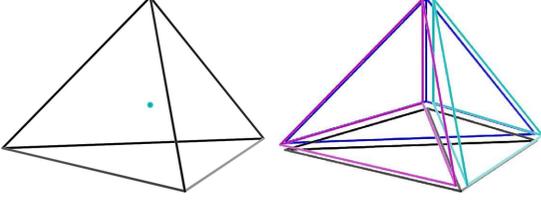
Figure 3. A '1-to-4' flip. A newly inserted point splits its insertion tetrahedron into 4 daughter tetrahedra.
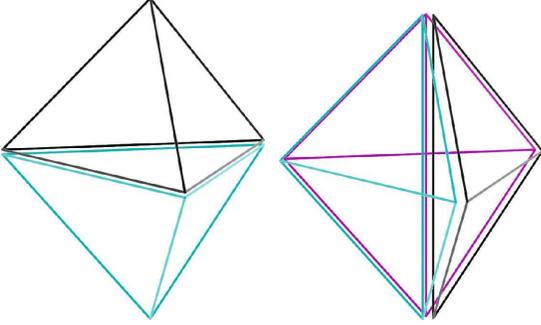

Figure 4. The standard replacement operation in 3D required for restoring Delaunayhood. It consists of 2-to-3 (from left to right) or 3-to-2 (from right to left) flips of tetrahedra. Note that the 2-to-3 flip is only possible if the line connecting the two points opposite of the common face intersects the interior of this face. Conversely, the 3-to-2 flip is only possible if an edge is shared by exactly three tetrahedra.

face with the four new tetrahedra invalid. These tetrahedra have to be subjected to the *in-sphere test* with the inserted point. We store the faces that need to be tested on a stack, where we specify the face that needs to be tested for Delaunayhood with a reference to a tetrahedron and the face's opposite point (which is always the inserted point). If a face that is pulled from the stack fails the in-sphere test, we need to check how we can replace the two adjacent tetrahedra. Unlike in 2D, we cannot simply replace two tetrahedra with two other tetrahedra. Instead, we may be able to replace the two tetrahedra with three tetrahedra, in a '2-to-3 flip', provided the line connecting the two tips opposite of the common triangle of the two tetrahedra intersects this triangle in its interior. This is illustrated in Figure 4. If on the other hand the intersection point lies outside *one* of the edges of the common triangle, then there is a tetrahedron formed by this edge and the two tips which needs to be included in the replacement operation. We can then replace these three tetrahedra with two, in a '3-to-2 flip', which is just the reverse of the '2-to-3 flip' shown in Figure 4. We note that the intersection point may also lie outside *two* of the edges of the common triangle; in this case the violating face is not flipable and can be skipped. It can be shown that the algorithm nevertheless finishes successfully thanks to the flips that can be carried out for other violating faces. Depending on the type of the flip that has been performed, either two or three new faces need to be put onto the test stack. The tests and flips are then continued until the stack is empty, at which point the Delaunay tessellation is valid again.

In three dimensions, the relevant determinant for the in-sphere test is given by

$$T_{\mathrm{InSphere}}(\boldsymbol{a},\boldsymbol{b},\boldsymbol{c},\boldsymbol{d},\boldsymbol{e}) = \begin{vmatrix} 1 & a_x & a_y & a_z & a_x^2 + a_y^2 + a_z^2 \\ 1 & b_x & b_y & b_z & b_x^2 + b_y^2 + b_z^2 \\ 1 & c_x & c_y & c_z & c_x^2 + c_y^2 + c_z^2 \\ 1 & d_x & d_y & d_z & d_x^2 + d_y^2 + d_z^2 \\ 1 & e_x & e_y & e_z & e_x^2 + e_y^2 + e_z^2 \end{vmatrix}. \quad (3)$$

This is negative if the point $\boldsymbol{e}$ lies inside the circumsphere around the positively oriented tetrahedron $(\boldsymbol{a},\boldsymbol{b},\boldsymbol{c},\boldsymbol{d})$, it is positive if the point lies outside, and zero if it is exactly on the circumsphere. The orientation of a tetrahedron can be established by testing the sign of

$$T_{\mathrm{Orient3D}}(\boldsymbol{a},\boldsymbol{b},\boldsymbol{c},\boldsymbol{d}) = \begin{vmatrix} 1 & a_x & a_y & a_z \\ 1 & b_x & b_y & b_z \\ 1 & c_x & c_y & c_z \\ 1 & d_x & d_y & d_z \end{vmatrix}, \quad (4)$$

which is positive for positive orientation.[†]

Once the Delaunay triangulation is generated, we calculate the areas and centres of the Voronoi faces, and the volumes of all Voronoi cells, as well as their centres-of-mass. To this end, we first calculate the midpoints of the circumspheres around each tetrahedron; these points form the vertices of the Voronoi cells. We then introduce a new data structure for each Voronoi face, storing the face area and references to the two adjacent cells, information that is later needed to determine the hydrodynamic fluxes across the face. To calculate the area of a Voronoi face, we circle in clockwise fashion around all tetrahedra that share the same Delaunay edge between the two mesh-generating points that belong to the face. Note that the line connecting these two points need not necessarily intersect the face. Once we have determined the area of the face, we can also easily obtain the volumes of the two equally-sized pyramids formed by the face and its two associated mesh-generating points. The volume of each Voronoi cell is then obtained as a sum over the pyramid volumes of all the cell's surface polyhedra.

2.1 Data structures for the tessellation

From the above it is clear that an important practical consideration for working with an unstructured polyhedral mesh is the use of efficient data structures to represent the tessellation. Ideally, the data structure should allow rapid and convenient access to the topological objects of the tessellation, such as individual triangles, the surfaces of Voronoi polyhedra, and neighbourhood relations, while at the same time not requiring too much memory. In 2D, Guibas & Stolfi (1985) introduced an elegant *quad-edge* data structure which can encode both the Delaunay triangulation and its dual at the same time. Besides storing references to the points of an edge, this edge-based structure stores links to the first adjacent edges in a clockwise or anticlockwise direction around the end points. While being very elegant, it is difficult to extend this structure to three dimensions. The 'face-edge' structure of Dobkin & Laszlo (1989) is one such possibility, but it produces substantial memory overhead. We therefore

---

[†] Note that the value of the determinant is equal to six times the volume of the tetrahedron spanned by the four points.

follow the approach taken in most codes for 3D Delaunay triangulation and adopt full tetrahedra as basic data structures for describing the mesh. In 2D, we correspondingly use full triangles.

For each tetrahedron, we store references to its four points. These are oriented such that the fourth point lies above the oriented triangle formed by the first three points. We also store along with each point of a tetrahedron a reference to the adjacent tetrahedron that lies opposite of the point and shares a face with the present tetrahedron. In addition, we store the index location of the point in this adjacent tetrahedron that lies opposite to the common face. This simplifies various types of construction and navigation tasks in the tessellation. Note that using this data structure we can also easily specify individual faces of tetrahedra in terms of a reference to the tetrahedron and to the point that lies *opposite* to the face in question.

A disadvantage of our data structure is its comparatively large memory requirement. If pointers are used for references to the 4 vertices and 4 adjacent tetrahedra of each tetrahedron, 36 bytes are required on 32-bit architectures per tetrahedron, or 68 bytes on 64-bit machines (using integer indices instead of pointers can however easily reduce this back to 36 bytes, which is completely sufficient if there are less than $\sim 200\,\mathrm{GB}$ or so available per MPI task, which is well above the parameters of current supercomputers). For a random point set, there are on average ~ 6.77 Delaunay tetrahedra per point (van de Weygaert, 1994), giving ~ 244 bytes (or $\sim$460 bytes if pointers on 64-bit architectures are used) per point for storing the mesh. Additional storage is required to hold a list of faces for the flux calculation. This sums up to a relatively hefty cost in terms of memory, a factor 3 to 4 or so larger than what is needed for the tree construction in a Tree-SPH code like GADGET-2, but not something that prohibitively restricts the sizes of possible simulations. However, we note that by exploiting the adjacency relations to label nearby tetrahedra, the memory cost could in principle be reduced to just about 7.5 bytes per tetrahedron in 3D (Blandford et al., 2005). We leave such memory optimizations for future work.

2.2 Point location

The point location in the above insertion algorithm can be a limiting factor, as a simple search through all triangles/tetrahedra would produce an N^2-scaling of the algorithm. But there are different possible approaches for speeding up the point location. One idea is to store the past insertion history of Delaunay triangles in a directed acyclic graph (Edelsbrunner & Shah, 1996), such that the insertion triangle can be localized through a tree-walk. However, the manipulation of the history graph requires complex bookkeeping and large amounts of memory.

Another method is the 'jump and walk' procedure for point location first proposed by Mücke et al. (1996). Here one walks through the tessellation from a random triangle in the direction of the point that is to be inserted. We will adopt this strategy. However, instead of starting at a random triangle or using a search grid for rapid location of an initial triangle, we order the points that are to be inserted along a space-filling Peano-Hilbert curve (Springel, 2005), a trick that has also been employed by the tessellation code
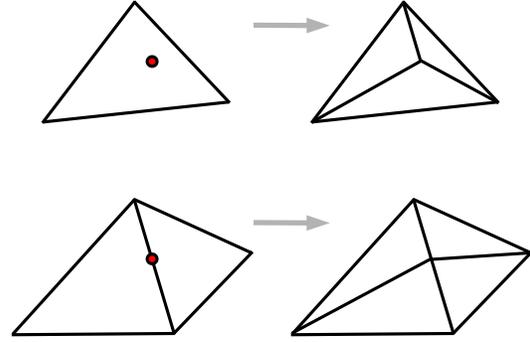

Figure 5. Point insertion in 2D in the normal case (top, via a 1-to-3 flip) and the degenerate case (bottom), where the point lies *exactly* on an edge of the current tessellation. In the latter case, the two triangles need to be replaced with four triangles (a 2-to-4 flip).

tess3 (Liu & Snoeyink, 2005). This guarantees that the next point that is inserted is always spatially close to the previous one. If we hence remember a pointer to the last processed triangle/tetrahedron, we can start the search in the immediate neighbourhood of the insertion triangle, and only a very small number of steps are required to arrive at the correct triangle. An additional advantage of this scheme lies in cache utilization benefits; thanks to the spatial proximity of subsequent insertion points, much of the required memory has been accessed recently and may hence still be resident in the processor's cache, which increases performance.

To test whether a point lies inside a given tetrahedron, we calculate whether it lies above all four of the planes defined by its oriented triangles. If the point does not lie in the current tetrahedron, we determine which of its faces is intersected by a line from the centre of mass of the tetrahedron to the insertion point, and then change to the adjacent tetrahedron on the other side of the selected face.

The above requires an efficient way to test whether a given point lies inside a tetrahedron (or triangle in 2D). Since all our tetrahedra are positively oriented, one way to do this is to use four orientation tests: if the point in question lies above all four oriented triangles of the tetrahedron, it must be inside. However, this is slow due to the required evaluation of four determinants. A faster method is to expand the coordinates of the given point in terms of the three linearly independent vectors spanned by the four points of the tetrahedron. This involves a linear system of equations which can be quickly solved with Gauss elimination. The values of the expansion coefficients α, β and γ then directly indicate whether the point lies inside the tetrahedron. This is the case if we simultaneously have $\alpha > 0$, $\beta > 0$, $\gamma > 0$ and $\alpha + \beta + \gamma < 1$. Only when there is a danger of obtaining the incorrect result with this method due to numerical round-off, we use instead an *exact* evaluation of the four orientation tests, which we discuss in more detail below.

2.3 Treatment of degenerate cases

A problematic point about incremental insertion is that in this method it can become hard to deal with degenerate point sets. In particular, the algorithm described above for
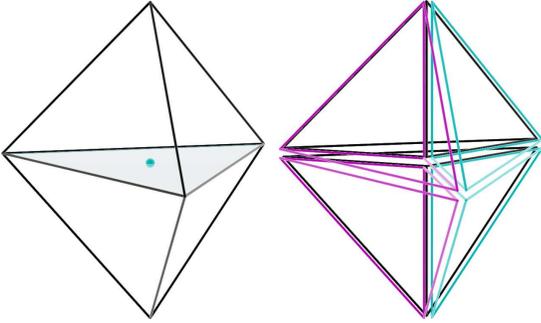
Figure 6. Degeneracy during point insertion in 3D. Here the point that is to be inserted falls onto a face of the current tessellation. The two tetrahedra involved need to be replaced by six tetrahedra, constituting a 2-to-6 flip.
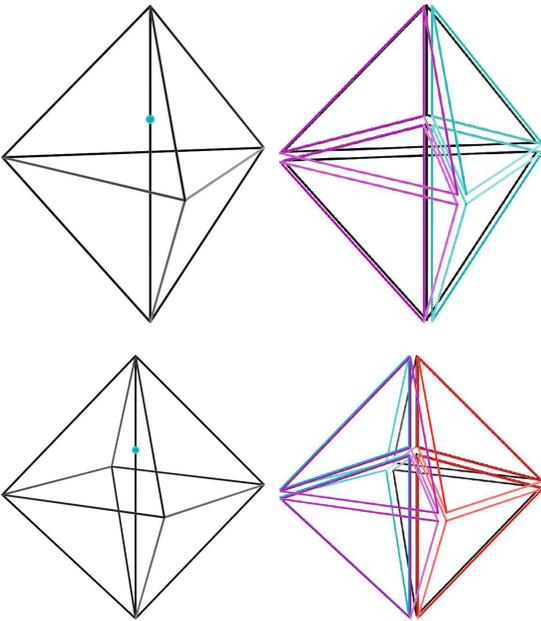

Figure 7. Degeneracy during point insertion in 3D. Here the point that is to be inserted falls onto an edge of the current tessellation. In this case, we need to make a n-to-$2n$ flip, where n is the number of tetrahedra that have the edge in common. In most case this is either 3 (top left) or 4 (bottom left), like in the examples shown in this figure, but n can in principle also be larger.

constructing the Delaunay triangulation only works robustly for points in *general position*, where in 2D never more than three points lie on a circle, and never more than 2 points lie on a line. If we start with a regular point distribution, for example a Cartesian grid, this condition is evidently strongly violated. But even for random point sets, it is possible that a degenerate situation approximately occurs, and due to floating point round-off, we may not be able to correctly decide the outcome of one of the geometric tests, i.e. to evaluate the *correct sign* of a nearly degenerate determinant (e.g. Clarkson, 1992). However, failure to do so invariably leads to a breakdown of the mesh construction. In addition, experience shows that attempts to address this issue with crude patches,
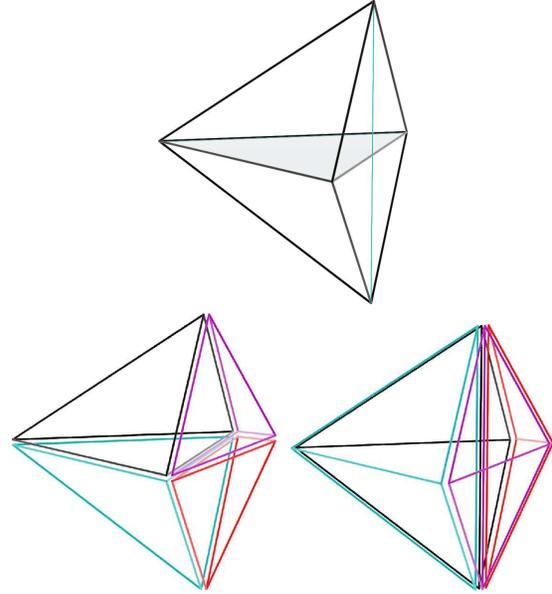

Figure 8. Flipping degeneracy in 3D. If the line that connect the two points opposite a common face of two tetrahedra intersects this face on one of its edges (like in the sketch on top), the standard 2-to-3 flip cannot be carried out. Instead, the two tetrahedra may be eligible for a 4-to-4 flip. This requires however that the intersected edge is the common edge to exactly 4 tetrahedra. In this case, four tetrahedra can be replaced by 4 tetrahedra, as shown in the bottom of the sketch.

for example in the form of random point perturbations, provides only unreliable (and inelegant) work-arounds.

One possible approach for solving this issue lies in systematically applying *symbolic perturbations* to the particle coordinates (Edelsbrunner & Mucke, 1990), which effectively bring the particles into general position, such that the Delaunay triangulation becomes formally unique and the algorithm for constructing the tessellation is guaranteed to succeed. There may then still be triangles/tetrahedra of zero volume attached to the complex hull of the final tessellation, but their removal represents no major problem. However, the symbolic perturbation approach still requires robust evaluations of the correct sign of determinants, which Mücke (1998) proposes to obtain with long-integer arithmetic.

Another possible method for constructing robust geometric predicates is to employ *exact* floating point arithmetic, implemented through suitable software packages. This is however very much slower than standard double-precision arithmetic. An attractive alternative is to use adaptive precision arithmetic, as proposed and implemented by Schewchuk (1997). Here the idea is to monitor the maximum round-off error that can occur in the evaluation of a geometric test. If there is a risk that the correct result may be missed with standard floating point arithmetic (which is carried out in hardware by the CPU), progressively more accurate approximations to exact floating point arithmetic are employed, until the correctness of the calculated sign can be guaranteed. Since the exact but slow floating point arithmetic is only used when it is really needed, this adaptive

precision approach is much faster than using exact floating point arithmetic throughout.

We use a different method instead which does not need perturbed point coordinates, but rather relies on modifications of the point insertion algorithm such that it can directly deal with degeneracies, and we combine this with a scheme that always guarantees the correct evaluation of geometric predicates. Let us first discuss the latter. We here follow the idea of Schewchuk (1997) and estimate the maximum round-off error in evaluations of in-circle and orientation tests. When there is a risk of getting the wrong sign with standard floating point arithmetic, we however evaluate the determinant with exact long integer arithmetic, which is both simple and robust. To this end we establish a one-to-one mapping between the floating point numbers of our point coordinates and the space of 53-bit integers. This is accomplished by mapping our computational domain to the floating point interval $[1, 2[$. All these numbers have the same exponent in the standard Institute of Electrical and Electronics Engineers (IEEE) representation of double-precision numbers, and the 53-bit mantissa effectively provides a linear and uniform grid of the possible floating point values in this interval. We read out this mantissa and use it to evaluate exact geometric predicates using long integer arithmetic with the open-source GMP library, when needed.

Let us now discuss the modifications required in the point insertion algorithm such that it can deal with degenerate input point sets if correctness of the geometric tests can be guaranteed. In two dimensions, only one such modification is required. We need to detect the case that the point that is to be inserted lies on an edge of the current tessellation, as illustrated in Figure 5. In this case, we can not replace one triangle with three new ones, but instead need to split both of the triangles that share the edge into two triangles.

In three dimensions, things are considerably more complicated. Here the point that is to be inserted may lie on a face of the current tessellation. In this case, we need to replace the two adjacent tetrahedra with altogether 6 new tetrahedra. This replacement represents a '2-to-6 flip', as shown in Figure 6. It may also happen that the point falls onto an edge of the current tessellation. There may be 3, 4, or more tetrahedra present that share this edge. All of them have to be replaced by two tetrahedra each, such that we effectively carry out an 'n-to-$2n$ flip', as illustrated in Figure 7. Finally, when degeneracies are present, a further case needs to be considered in the flipping operations that heal the mesh after a point has been inserted. Recall that the decision whether a 2-to-3 or 3-to-2 flip is carried out when an invalid Delaunay face has been found depends on the location of the intersection between this triangular face and the line that connects the tips of the adjacent tetrahedra. Previously, we discussed the cases where the intersection lies inside the triangle, or outside. For degenerate cases, it may lie exactly on one of the edges, a case that requires special treatment. Here a '4-to-4' flip is possible and needs to be carried out when needed, as illustrated in Figure 8.

We note that the topology of the resulting Delaunay tessellation is not unique if degeneracies are present, and the exact outcome (i.e. which of the different Delaunay tessellations that are possible is realized) depends on the order in which the points are inserted. However, the corresponding Voronoi tessellation is still unique, and hence the outcome of our hydrodynamical calculations is unaffected by the Delaunay non-uniqueness in the presence of degeneracies, and also does not depend on the order in which the mesh-generating points are inserted.

A related point concerns the change of the topology of the mesh when the points are moved. While the Delaunay triangulation changes *discontinuously* whenever a point is moved into or out of the circumsphere of another triangle, the corresponding Voronoi tessellation changes *continuously*. In fact, whenever the Delaunay neighbourhood relations between two points change, the corresponding Voronoi face shrinks to a vanishing area. As we will see later on, it is this property that allows the mesh to deform without running into the mesh-tangling problems that plague other approaches for moving meshes. Also, note that we can calculate the full motion of all Voronoi faces based just on the velocity vectors of the mesh generating points. We will make use of this property in our hydrodynamical schemes, as discussed in Section 3.

2.4   Parallelization of the tessellation code

Modern supercomputer platforms feature hundreds to thousands of compute cores, with a continuing trend to ever larger numbers of cores. Efficient use of this combined processing power for simulations of dynamically tightly coupled systems can be quite challenging, especially on distributed memory computers, which offer the largest and most cost effective performance. Parallelization of simulation codes for such architectures requires decomposition of a problem into individual parts, provided we want to avoid complete data duplication, which is prohibitive if good scalability is desired.

A number of parallel construction algorithms for the Delaunay triangulation have been proposed, some of them for distributed memory environments (e.g. Cignoni et al., 1998; Lee et al., 2001), others for shared memory machines (Blandford et al., 2006). However, the approach of Cignoni et al. (1998) replicates the entire point set on each independent processor, an approach we can not afford to follow in the interest of scalability.

Rather, we decompose the point set into disjoint spatial domains, each mapped to a different compute core with its own physical memory. The idea here is that most of the Voronoi cells of a domain will lie in its interior and hence only depend on the data local to the processor, while some cells close to the surface may be affected by data on other processors, which needs to be dealt with by data communication. Our strategy to deal with this issue is to construct a locally complete tessellation by importing *ghost points* from neighbouring processors such that all the Voronoi cells of the points that are local to the domain are correctly formed. This means that the joint set of all primary Voronoi cells forms the complete tessellation, but there is no need to actually ever form it explicitly, i.e. we do not need to somehow mesh the tessellations across two neighbouring domains together, which would be cumbersome. Instead, the ghost points provide the 'glue' that gives the proper connectivity across domains. We will also use ghost points to implement periodic or reflecting boundary conditions, which are simply realized through fiducial points that are imported from

the 'other side' of the simulation box. In practice, the use of ghost points increases the number of cells that need to be considered by a given processeor typically by $3 - 10\%$, depending on how many processors are used. Only if a large number of processors is used for a small problem, this induces significant overhead and a limit to scalability.

How can we find the ghost points that need to be imported, and how can we be sure that our local point set is sufficiently complete? We have implemented two different algorithms for this task. In the simpler of the two, we start by first constructing the tessellation for all local points r_i within a domain. With each of the points we associate a search radius h_i, inherited either from the previous timestep, or initialized with a guess. We then search for all points on *other processors* that lie within the spheres/circles of radius h_i around r_i. The union of the ghost points found in this way is then added to the local tessellation. For each local point, we can then calculate a radius s_i equal to twice the maximum radius of all the circumspheres of the Delaunay tetrahedra that have the point r_i as one vertex. The relevant geometry is illustrated for two dimensions in the sketch of Figure 9. Here the red circle has radius s_i around the target point i, which has an associated Voronoi cell shown in light blue. This local Voronoi cell around point r_i could only change if there was a further point somewhere inside the red circle that has not yet been added to the local tessellation. If we have $h_i > s_i$, then we know that such a point does not exist, and we are guaranteed that the Voronoi cell around point i is correct. Otherwise, we need to look whether further points from other processors need to be added to the local tessellation. In this case we increase the radius h_i by some factor and search again for *additional* points on other processors that have not yet been inserted into the local tessellation. These points are then added to the local tessellation, and the s_i are redetermined. The process is repeated until the condition $h_i > s_i$ holds for all points local to the processor, at which point the local tessellation is complete, i.e. all Voronoi cells of local points are guaranteed to be unaffected by the presence of the domain boundary.

Note that the 'thickness' of the layer of ghost points imported on each domain is not fixed in this scheme, rather it adjusts to variations of density along the domain boundaries, as well as to the geometry of the domains themselves. Once the tessellation is complete, we set h_i to s_i for use in the next mesh construction; this usually ensures close to optimum efficiency in finding the minimum required set of ghost particles.

However, sometimes the above approach may create a ghost layer that is thicker than really required in situations where the mesh resolution shows a strong spatial gradient, and a domain boundary lies orthogonal to this gradient. Since the search region for ghosts is taken to be spherical, this may lead to the import of a comparatively large number of ghost points from the side where the mesh resolution becomes finer. If the mesh resolution changes sufficiently rapidly in space, this can then incur a substantial overhead that exceeds the usual $3 - 10\%$ mentioned above. We have therefore also implemented an alternative algorithm to determine the ghost region, which is more efficient in this situation. In this approach we directly search for possible ghosts in *all* circumcircles of those triangles in the local tessellation that have at least one local particle as one of their vertices.

If a ghost point is found, all triangles modified in the point insertion step of the ghost will be tested again until no further ghosts are found. At the end, this method then guarantees that all Delaunay triangles shared by a local particle are part of the correct global mesh, and hence the Voronoi cell of this particle is complete. To prevent that initially very many ghost points are found in the large triangles present in the first iteration at the surface of the local domain, we always insert only the closest ghost particle found in a circumcircle that has not yet been added to the local mesh. Especially when individual timesteps are used and only parts of the mesh are constructed for active particles (as discussed later in the context of our individual time-stepping scheme), this approach is usually more efficient, despite its larger number of spatial point searches.

The above techniques relies on rapid algorithms to find all particles within a given sphere of arbitrary radius. To this end we employ a Barnes & Hut (1986) octtree and use the neighbour search algorithms of the parallel SPH code GADGET-2 (Springel, 2005). We also adopted the specific domain decomposition strategy from the GADGET-2 code, which is based on subdividing a space-filling Peano-Hilbert curve, an approach that has recently become popular also in other cosmological simulation codes (e.g. Shirokov & Bertschinger, 2005). Similar to GADGET-2, we also use a 'top-level tree' that covers the full simulation volume. This allows us to quickly decide whether or not a local search region is fully contained in the local domain, and if not, with which other processors it overlaps. This is also useful for devising an efficient communication strategy.

The complexity of the tessellation algorithms discussed in this section might suggest that the resulting computations are quite expensive and slow, but we want to remark that this is not really the case. The geometric tests required to insert a point involve primarily linear algebra operations that are calculated very efficiently on modern processors (which often offer combined multiply-add operations in a single cycle), while the rearrangement of local triangles or tetrahedra reduces to reorientations of pointers. As a result, even without significant efforts for speed optimizations, we reach tessellation speeds on the order of several tens of thousands of tetrahedra per second. This is comparable to or only slightly more than the work needed for SPH neighbour search. More importantly, the computational cost continues to scale just as $N \log N$. There is hence in principle no obstacle to use the tessellation techniques for large-scale applications, even if the mesh is reconstructed each timestep, as in our current approach.

2.5 Other applications of the tessellation code

While in the rest of this paper we will focus on applying the Voronoi mesh to problems of continuum hydrodynamics, we briefly want to mention that the tessellation methods discussed here are also useful in other contexts.

In particular, Voronoi or Delaunay tessellations are useful for general density reconstruction tasks. For example, van de Weygaert (1994) used Voronoi tessellation to study cosmic large-scale structure and Bernardeau & van de Weygaert (1996) employed them to analyze the statistics of velocity fields. Schaap & van de Weygaert (2000) and Pelupessy et al. (2003) proposed to use Delaunay tessellation as a general es-
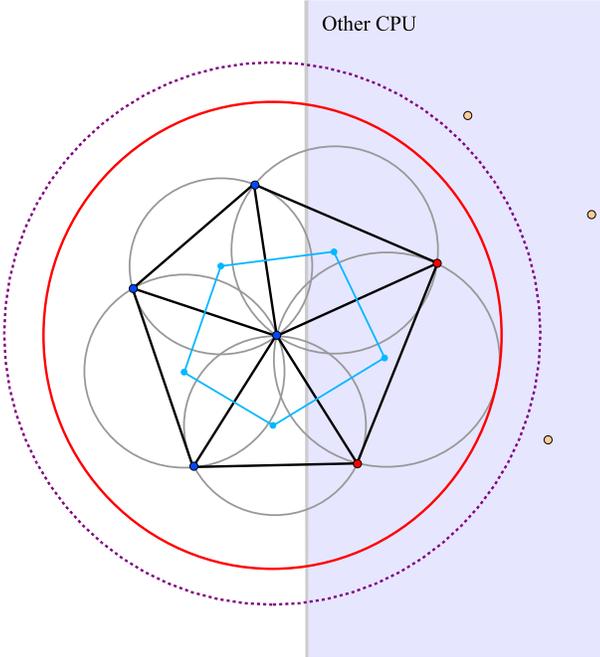
Figure 9. Geometry of the test for local completeness of a Voronoi cell. Points on the left of the vertical grey line reside on the local domain. The point i at the centre of the Voronoi cell (shown in light blue) has a search radius h_i equal to the dotted circle; all points on other processors inside this circle have been imported as ghost points (red dots) and were added to the local tessellation. We now have to decide whether the resulting Voronoi cell around point i could still be modified by points not yet added to the local tessellation. To this end we consider the circumcircles (shown in grey) of all Delaunay triangles that share the central point. The smallest circle encompassing all these circumcircles has a radius s_i equal to twice the maximum circumcircle radius, and is shown in red. If the red circle lies inside the dotted circle, i.e. for $s_i \leq h_i$, all the Delaunay triangles around the target point i are valid and are part of the fiducial global Delaunay tessellation that contains all points. Consequently, in this case the Voronoi cell around the target point i is complete and unaffected by the presence of the nearby domain boundary. For $s_i > h_i$, we increase h_i and add any additional point found in the enlarged search region, until the condition $s_i \leq h_i$ is fulfilled.

timation tool for linear reconstructions of the density field, based on the *contiguous Delaunay cell* that is formed by all Delaunay triangles around a given point.

We have applied Voronoi density estimates to calculate the dark matter annihilation signal expected in high-resolution dark matter simulations of the formation of a Milky-Way like galactic halo (Springel et al., 2008). In comparison with SPH, this has the advantage to provide an unbiased sum of the volumes assigned to each particle, and to produce less damping of the smallest resolved structures by smoothing. In our largest simulation, we constructed a Voronoi mesh for nearly 5 billion particles, composed of about 34 billion tetrahedra in the dual Delaunay tessellation, and with a dynamic range in point density of more than 10^7. This may well be one of the largest Voronoi meshes ever constructed. The mesh construction took 516 seconds on 1024 CPUs of an SGI Altix 4700 (the HLRB-II machine at the Leibniz-Computing Centre in Garching, Germany).

Outside of astronomy, Voronoi tessellations are widely applied for many different applications, including point pattern analysis, modelling of spatial processes, location optimization, and computer graphics, to name just a few. A comprehensive introduction to these applications can be found in the monograph of Okabe et al. (2000).

3   FINITE VOLUME HYDRODYNAMICS ON A MOVING VORONOI MESH

The Euler equations are conservation laws for mass, momentum and energy that take the form of a system of hyperbolic partial differential equation. They can be written in compact form by introducing a state vector

$$\boldsymbol{U} = \begin{pmatrix} \rho \\ \rho\boldsymbol{v} \\ \rho e \end{pmatrix} = \begin{pmatrix} \rho \\ \rho\boldsymbol{v} \\ \rho u + \frac{1}{2}\rho\boldsymbol{v}^2 \end{pmatrix} \tag{5}$$

for the fluid, where ρ is the mass density, $\boldsymbol{v}$ is the velocity field, and $e = u + \boldsymbol{v}^2/2$ is the total energy per unit mass. u gives the thermal energy per unit mass, which for an ideal gas is fully determined by the temperature. These fluid quantities are functions of the spatial coordinates $\boldsymbol{x}$ and time t, i.e. $U = U(\boldsymbol{x}, t)$, but for simplicity we will often refrain from explicitly stating this dependence in our notation. Based on $\boldsymbol{U}$, we can define a flux function

$$\boldsymbol{F}(\boldsymbol{U}) = \begin{pmatrix} \rho\boldsymbol{v} \\ \rho\boldsymbol{v}\boldsymbol{v}^T + P \\ (\rho e + P)\boldsymbol{v} \end{pmatrix}, \tag{6}$$

with an equation of state

$$P = (\gamma - 1)\rho u \tag{7}$$

that gives the pressure of the fluid. The Euler equations can then be written in the compact form

$$\frac{\partial \boldsymbol{U}}{\partial t} + \boldsymbol{\nabla} \cdot \boldsymbol{F} = 0, \tag{8}$$

which emphasizes their character as conservation laws for mass, momentum and energy.

Over the past decades, a large variety of different numerical approaches to solve this coupled set of partial differential equations have been developed (see Toro, 1997; LeVeque, 2002, for comprehensive expositions). Many modern schemes are descendants of Godunov's method, which revolutionized the field. By solving an exact or approximate Riemann problem at cell boundaries, Godunov's method allows the correct identification of the eigenstructure of the local solution and of the upwind direction, which is crucial for numerical stability. While Godunov's original method offers only first order accuracy and is relatively diffusive, it can be extended to higher order accuracy relatively simply, and in many different ways.

We will here employ a so-called *finite-volume* strategy, in which the discretization is carried out in terms of a subdivision of the system's volume into a finite number of disjoint cells. The fluid's state is described by the cell-averages of the conserved quantities for these cells. In particular, integrating the fluid over the volume V_i of cell i, we can define the total mass m_i, momentum p_i and energy E_i contained in the cell as follows,

$$\boldsymbol{Q}_i = \begin{pmatrix} m_i \\ \boldsymbol{p}_i \\ E_i \end{pmatrix} = \int_{V_i} \boldsymbol{U} \, \mathrm{d}V. \tag{9}$$

With the help of the Euler equations, we can calculate the rate of change of $\boldsymbol{Q}_i$ in time. Using Gauss' theorem to convert the volume integral over the flux divergence into a surface integral over the cell results in

$$\frac{\mathrm{d}\boldsymbol{Q}_i}{\mathrm{d}t} = -\int_{\partial V_i} \left[\boldsymbol{F}(\boldsymbol{U}) - \boldsymbol{U}\boldsymbol{w}^T \right] \mathrm{d}\boldsymbol{n}. \tag{10}$$

Here $\boldsymbol{n}$ is an outward normal vector of the cell surface, and $\boldsymbol{w}$ is the velocity with which each point of the boundary of the cell moves. In Eulerian codes, the mesh is taken to be static, so that $\boldsymbol{w} = 0$, while in a fully Lagrangian approach, the surface would be allowed to move at every point with the local flow velocity, i.e. $\boldsymbol{w} = \boldsymbol{v}$. In this case, the right hand side of equation (10) formally simplifies, because then the first component of $\boldsymbol{Q}_i$, the mass, stays fixed for each cell. Unfortunately, it is normally not possible to follow the distortions of the shapes of fluid volumes exactly in multi-dimensional flows for a reasonably long time, or in other words, one cannot guarantee the condition $\boldsymbol{w} = \boldsymbol{v}$ over the entire surface. In this case, one needs to use the general formula of equation (10), as we will do in this work.

The cells of our finite volume discretization are poly-hedra with flat polygonal faces (or lines in 2D). Let $\boldsymbol{A}_{ij}$ describe the oriented area of the face between cells i and j (pointing from i to j). Then we can define the averaged flux across the face i-j as

$$\boldsymbol{F}_{ij} = \frac{1}{A_{ij}} \int_{A_{ij}} \left[\boldsymbol{F}(\boldsymbol{U}) - \boldsymbol{U}\boldsymbol{w}^T \right] \mathrm{d}\boldsymbol{A}_{ij}, \tag{11}$$

and the Euler equations in finite-volume form become

$$\frac{\mathrm{d}\boldsymbol{Q}_i}{\mathrm{d}t} = -\sum_j A_{ij}\boldsymbol{F}_{ij}. \tag{12}$$

We obtain a manifestly conservative time discretization of this equation by writing it as

$$\boldsymbol{Q}_i^{(n+1)} = \boldsymbol{Q}_i^{(n)} - \Delta t \sum_j A_{ij}\hat{\boldsymbol{F}}_{ij}^{(n+1/2)}, \tag{13}$$

where the $\hat{\boldsymbol{F}}_{ij}$ are now an appropriately time-averaged approximation to the true flux $\boldsymbol{F}_{ij}$ across the cell face. The notation $\boldsymbol{Q}_i^{(n)}$ is meant to describe the state of the system at step n. Note that $\hat{\boldsymbol{F}}_{ij} = -\hat{\boldsymbol{F}}_{ji}$, i.e. the discretization is manifestly conservative.

Evidently, a crucial step lies in obtaining a numerical estimate of the fluxes $\hat{\boldsymbol{F}}_{ij}$, and a good fraction of the literature on computational fluid dynamics is concerned with this problem. This issue is particularly important since the most straightforward (and perhaps naive) approach for estimating the fluxes, namely simply approximating them as the average of the left and right cell-centred fluxes catastrophically fails and invariably leads to severe numerical integration instabilities that render such a scheme completely useless in practice.

One effective cure for the stability problem lies in "upwind" schemes that do not weight the two sides equally, but rather with a bias in the upwind direction of the flow. This works especially well for simpler equations than the Euler
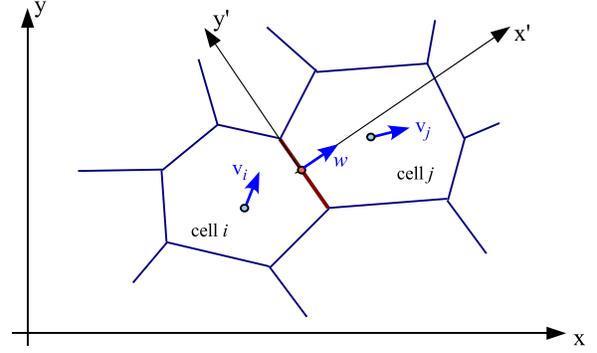

Figure 10. Geometry of the flux calculation. We use an unsplit scheme where the flux across each face is estimated based on a one-dimensional Riemann problem. To this end, the fluid state is expressed in a frame which moves with the normal velocity $\boldsymbol{w}$ of the face, and is aligned with it. Note that the motion of the face is fully specified by the velocities of the mesh-generating points of the cells left and right of the face.

system, for example the advection equation. Another, physically particularly meaningful approach is given by the family of Godunov methods, which employ analytic solutions of the Riemann problem occurring at each cell interface, either obtained exactly or approximately.

We will employ Godunov's method in the form of the MUSCL-Hancock scheme (van Leer, 1984; Toro, 1997; van Leer, 2006), which is a well-known and relatively simple approach for obtaining second-order accuracy in space and time. This scheme is also popular in astronomy and used in several state-of-the art Eulerian codes (e.g. Fromang et al., 2006; Mignone et al., 2007; Cunningham et al., 2009). In its simplest form, the MUSCL-Hancock scheme involves a slope-limited piece-wise linear reconstruction step within each cell, a first order prediction step for the evolution over half a timestep, and finally a Riemann solver to estimate the time-averaged inter-cell fluxes for the timestep.

Figure 10 gives a sketch of the problem of estimating the flux across the face between two Voronoi cells. Since truly multidimensional Riemann solvers are not known, we will calculate the flux for each face separately, treating it as an effectively one-dimensional problem. Since we do not work with Cartesian meshes, we cannot use operator splitting (Strang, 1968) to deal with the individual dimensions. Rather we use an *unsplit* method where all the fluxes are computed in one step, and are then collectively applied to calculate the change of the conserved quantities in a cell. For defining the Riemann problem normal to a cell face, we rotate the fluid state into a suitable coordinate system with the x'-axis normal to the cell face (see sketch). This defines the left and right states across the face, which we pass to an exact Riemann solver. The latter is implemented following Toro (1997) with an extension to treat vacuum states, but could easily be substituted with an approximate Riemann solver for higher performance, if desired. We have also written an exact Riemann solver for isothermal gas, similar to the scheme of Balsara (1994). We note that in multi-dimensions the transverse velocities are also required in the Riemann problem in order to identify the correct upwind transverse velocity, which is important for an accurate

treatment of shear. Once the flux has been calculated with the Riemann solver, we transform it back to the lab frame.

A further important point concerns the treatment of the allowed motion of cell surfaces in our scheme. In order to obtain stable upwind behaviour, the Riemann problem needs to be solved *in the frame of the moving face*. This is important as the one-dimensional Godunov approach is not Galilean-invariant in the following sense: Suppose left and right state at an interface are described by $(\rho_\mathrm{L}, P_\mathrm{L}, v_\mathrm{L})$ and $(\rho_\mathrm{R}, P_\mathrm{R}, v_\mathrm{R})$, for which the Riemann solver returns an interface state $(\rho_\mathrm{F}, P_\mathrm{F}, v_\mathrm{F})$ that is the basis for the flux estimate. For example, the mass flux across the interface is then given by $\rho_\mathrm{F} v_\mathrm{F}$. Consider now a velocity boost v applied both to the left and the right side. The new Riemann problem is given by $(\rho_\mathrm{L}, P_\mathrm{L}, v_\mathrm{L} + v)$ and $(\rho_\mathrm{R}, P_\mathrm{R}, v_\mathrm{R} + v)$, and its solution will be sampled at the fixed coordinate $x = 0$ in the new frame of reference, returning a flux estimate $\rho'_F v'_F$. However, in general this will yield $\rho'_F v'_F \neq \rho_\mathrm{F}(v_\mathrm{F} + v)$, which means that the calculated flux vectors are not Galilean invariant. This is not necessarily a problem in practice, but as we will see, it can drastically reduce the accuracy of Eulerian hydrodynamics in the presence of large bulk velocities. For this reason, we pay particularly attention to obtain a Galilean-invariant formulation of our new scheme, which should be possible if the mesh motion is tied to the fluid motion.

It is important to note that the Riemann problem itself is an exact solution of the Euler equations, which is of course Galilean-invariant. However, the flux vector read off from the Riemann solution does not transform in a Galilean-invariant way, simply because the location where the self-similar solution is sampled depends on the frame of reference. A timestep in our scheme may also be viewed as a sequence of reconstruction, evolution, and averaging steps (REA approach). Both the spatial reconstruction (which is linear in the primitive variables) as well as the evolution steps (by means of the Riemann solver) are Galilean-invariant, but the averaging is not; it depends on the frame of reference. Note that the flux vectors simultaneously encode the evolution and the averaging, and their non-invariance ultimately originates in the latter. An immediate and obvious corollary is that the diffusion error resulting from the averaging depends on the frame of reference. One may also say in a more general sense that the truncation error of the Eulerian approach is not Galilean-invariant. Finally, we would like to stress that this feature of Galilean non-invariance does of course not mean that the Eulerian approach necessarily creates incorrect results. It only means that the errors in the solutions depend on the frame of reference, which is a highly unwelcome feature. But as higher resolution always helps to reduce the diffusion error, one should always be able to beat down, at potentially considerable numerical cost, the additional diffusion error obtained from some bulk velocity to the point where it lies below a prescribed tolerance. Nevertheless, it is clearly desirable to have a numerical scheme where the Galilean-invariance of the Euler equations is manifestly retained in the discretized forms of the equations, a goal that is achieved by the method proposed here.

In our new hydrodynamical scheme, each timestep involves the following basic steps:

(i) Calculate a new Voronoi tessellation based on the current coordinates $\boldsymbol{r}_i$ of the mesh generating points. This also gives the centres-of-mass $\boldsymbol{s}_i$ of each cell, their volumes V_i, as well as the areas A_{ij} and centres $\boldsymbol{f}_{ij}$ of all faces between cells.

(ii) Based on the vector of conserved fluid variables $\boldsymbol{Q}_i$ associated with each cell, calculate the 'primitive' fluid variables $\boldsymbol{W}_i = (\rho_i, \boldsymbol{v}_i, P_i)$ for each cell.

(iii) Estimate the gradients of the density, of each of the velocity components, and of the pressure in each cell, and apply a slope-limiting procedure to avoid overshoots and the introduction of new extrema.

(iv) Assign velocities $\boldsymbol{w}_i$ to the mesh generating points.

(v) Evaluate the Courant criterion and determine a suitable timestep size Δt.

(vi) For each Voronoi face, compute the flux $\hat{\boldsymbol{F}}_{ij}$ across it by first determining the left and right states at the midpoint of the face by linear extrapolation from the cell midpoints, and by predicting these states forward in time by half a timestep. Solve the Riemann problem in a rotated frame that is moving with the speed of the face, and transform the result back into the lab-frame.

(vii) For each cell, update its conserved quantities with the total flux over its surface multiplied by the timestep, using equation (13). This yields the new state vectors $\boldsymbol{Q}_i^{(n+1)}$ of the conserved variables at the end of the timestep.

(viii) Move the mesh-generating points with their assigned velocities for this timestep.

For the sake of definiteness, we will now more explicitly describe the most important details of these different steps.

3.1 Gradient estimation and linear reconstruction

According to the Green-Gauss theorem, the surface integral of a scalar function over a closed volume is equal to its gradient integrated over the same volume, i.e.

$$\int_{\partial V} \phi\, \mathrm{d}\boldsymbol{n} = \int_V \boldsymbol{\nabla}\phi\, \mathrm{d}V. \tag{14}$$

This suggests one possible way to estimate the mean gradient in a Voronoi cell, in the form

$$\langle \boldsymbol{\nabla}\phi \rangle_i \simeq -\frac{1}{V_i} \sum_j \phi(\boldsymbol{f}_{ij})\, \boldsymbol{A}_{ij}, \tag{15}$$

where $\phi(\boldsymbol{f}_{ij})$ is the value of ϕ at the centroid $\boldsymbol{f}_{ij}$ of the face shared by cells i and j, and $\boldsymbol{A}_{ij}$ is a vector normal to the face (from j to i), with length equal to the face's area. Based on the further approximation

$$\phi(\boldsymbol{f}_{ij}) \simeq \frac{1}{2}(\phi_i + \phi_j), \tag{16}$$

this provides an estimate for the local gradient. Note that with the use of equation (16), the gradient of cell i only depends on the values ϕ_j of neighbouring cells, but not on ϕ_i itself. While the estimate (15) can be quite generally applied to arbitrary tessellations, due to the use of only one Gauss point per face it is also relatively inaccurate and is not exact to linear order in general.

For the special case of Voronoi cells, it is however possible to obtain a considerably better gradient estimate with little additional effort. The key is to carry out the surface integral more accurately. Let us assume that in the vicinity of a point i the scalar function $\phi(\boldsymbol{r})$ can be well approximated linearly as $\phi(\boldsymbol{r}) = \phi_i + \boldsymbol{b} \cdot (\boldsymbol{r} - \boldsymbol{r}_i)$. The vector $\boldsymbol{b}$ is the

local gradient that we seek to estimate. We can now write the surface integral as

$$V_i \langle \boldsymbol{\nabla}\phi \rangle_i = \int_{\partial V_i} \phi \, \mathrm{d}\boldsymbol{n} = \sum_{j \neq i} \int_{A_{ij}} [\phi_i + \boldsymbol{b} \cdot (\boldsymbol{r} - \boldsymbol{r}_i)] \frac{\boldsymbol{r}_j - \boldsymbol{r}_i}{r_{ij}} \mathrm{d}A \quad (17)$$

where the sum extends over all faces of the Voronoi cell of i, and the integrals extend over each of the faces. Note that we here already made use of the fact that the surface normal of each face is parallel to the separation vector of i and j, a property that is in general only fulfilled for Voronoi tessellations. Following the notation of Serrano & Español (2001), we now define $\boldsymbol{c}_{ij}$ as the vector from the midpoint between i and j to the centre-of-mass of the face between i and j, i.e.

$$\boldsymbol{c}_{ij} \equiv \frac{1}{A_{ij}} \int_{A_{ij}} \left(\boldsymbol{r} - \frac{\boldsymbol{r}_i + \boldsymbol{r}_j}{2} \right) \mathrm{d}A. \tag{18}$$

Noting that $\phi_j = \phi_i + \boldsymbol{b} \cdot (\boldsymbol{r}_j - \boldsymbol{r}_i)$, equation (17) can be rewritten as

$$V_i \langle \boldsymbol{\nabla}\phi \rangle_i = -\sum_{j \neq i} \left[\frac{\phi_i + \phi_j}{2} + \boldsymbol{b} \cdot \boldsymbol{c}_{ij} \right] \frac{\boldsymbol{r}_{ij}}{r_{ij}} A_{ij}. \tag{19}$$

where $\boldsymbol{r}_{ij} = \boldsymbol{r}_i - \boldsymbol{r}_j$ is the vector of length $r_{ij} = |\boldsymbol{r}_{ij}|$ connecting the two neighbouring points, and A_{ij} is the area of the face.

Next, we can make the replacement $(\boldsymbol{b} \cdot \boldsymbol{c}_{ij}) \, \boldsymbol{r}_{ij} = (\boldsymbol{b} \cdot \boldsymbol{r}_{ij}) \, \boldsymbol{c}_{ij} + \boldsymbol{b} \times (\boldsymbol{r}_{ij} \times \boldsymbol{c}_{ij})$, and set $\boldsymbol{b} \cdot \boldsymbol{r}_{ij} = \phi_i - \phi_j$. Then, the term involving the cross products can be rewritten by reinserting the definition of $\boldsymbol{c}_{ij}$:

$$\boldsymbol{b} \times \sum_{j \neq i} \frac{\boldsymbol{r}_{ij} \times \boldsymbol{c}_{ij}}{r_{ij}} A_{ij} = \boldsymbol{b} \times \sum_{j \neq i} \frac{\boldsymbol{r}_{ij}}{r_{ij}} \times \int \left(\boldsymbol{r} - \frac{\boldsymbol{r}_i + \boldsymbol{r}_j}{2} \right) \mathrm{d}A \quad (20)$$

The term involving $\boldsymbol{r}$ is really the surface integral $\int_{\partial V} \boldsymbol{r} \times \mathrm{d}\boldsymbol{n}$, which can be cast into a volume integral of the curl of $\boldsymbol{r}$, but $\boldsymbol{\nabla} \times \boldsymbol{r} = 0$ vanishes. Likewise, we have $\boldsymbol{r}_{ij} \times (\boldsymbol{r}_i + \boldsymbol{r}_j)/2 = \boldsymbol{r}_{ij} \times \boldsymbol{r}_i$, so that the remaining term is proportional to the surface integral $\int_{\partial V} \boldsymbol{r}_i \times \mathrm{d}\boldsymbol{n}$, which also vanishes since $\boldsymbol{r}_i$ is a constant vector. As a result, the double cross product $\boldsymbol{b} \times (\boldsymbol{r}_{ij} \times \boldsymbol{c}_{ij})$ gives a vanishing contribution to equation (19).

We are hence finally left with the following gradient estimate:

$$\langle \boldsymbol{\nabla}\phi \rangle_i = \frac{1}{V_i} \sum_{j \neq i} A_{ij} \left([\phi_j - \phi_i] \frac{\boldsymbol{c}_{ij}}{r_{ij}} - \frac{\phi_i + \phi_j}{2} \frac{\boldsymbol{r}_{ij}}{r_{ij}} \right). \tag{21}$$

Note that this result is exact to linear order, independent of the locations of the mesh-generating points of the Voronoi tessellation. Without the term involving $\boldsymbol{c}_{ij}$ this is the same as the simpler Green-Gauss estimate. However, retaining this extra term leads to significantly better accuracy, because the gradient estimate becomes exact to linear order for arbitrary Voronoi meshes. In practice, we shall therefore always use this gradient estimation in our MUSCL-Hancock scheme for the Euler equations, where we calculate in this way gradients for the 5 primitive variables (ρ, v_x, v_y, v_z, P) that characterize each cell.

The result (21) has also an interesting relation to the formulae obtained by Serrano & Español (2001) for the partial derivatives of the volume of a Voronoi cell with respect to the location of one of the points. As Serrano & Español

(2001) have shown, the derivative of the volume of a Voronoi cell due to the motion of a surrounding point is given by

$$\frac{\partial V_i}{\partial \boldsymbol{r}_j} = -A_{ij} \left(\frac{\boldsymbol{c}_{ij}}{r_{ij}} + \frac{\boldsymbol{r}_{ij}}{2r_{ij}} \right) \quad \text{for} \quad i \neq j. \tag{22}$$

Furthermore, they show that

$$\frac{\partial V_i}{\partial \boldsymbol{r}_i} = -\sum_{j \neq i} \frac{\partial V_j}{\partial \boldsymbol{r}_i}. \tag{23}$$

Using these relations, and noting that according to the Gauss theorem we have

$$\frac{\phi_i}{V_i} \sum_{j \neq i} A_{ij} \frac{\boldsymbol{r}_{ij}}{r_{ij}} = 0, \tag{24}$$

because the summation is just the surface integral of a constant function, we can also write the estimate for the gradient of ϕ at $\boldsymbol{r}_i$ more compactly as

$$\langle \boldsymbol{\nabla}\phi \rangle_i = -\frac{1}{V_i} \sum_j \frac{\partial V_j}{\partial \boldsymbol{r}_i} \phi_j. \tag{25}$$

An interesting corollary of the above is that provided $\phi(\boldsymbol{r})$ varies only linearly, the sum

$$S = \sum_i \phi(\boldsymbol{r}_i) V_i \tag{26}$$

approximates the integral $\int \phi(\boldsymbol{r}) \, \mathrm{d}V$ *exactly*, independent of the positions of the points that generate the Voronoi tessellation. This follows because we then have $\partial S/\partial \boldsymbol{r}_i = 0$ for all the points i.

In our approach, we use the gradients estimated with equation (21) for a linear reconstruction in each cell around the centre-of-mass. For example, the density at any point $\boldsymbol{r} \in V_i$ of a cell is estimated as

$$\rho(\boldsymbol{r}) = \rho_i + \langle \boldsymbol{\nabla}\rho \rangle_i \cdot (\boldsymbol{r} - \boldsymbol{s}_i), \tag{27}$$

where $\boldsymbol{s}_i$ is the centre of mass of the cell. Note that independent of the magnitude of the gradient and the geometry of the Voronoi cell, this linear reconstruction is conservative, i.e. the total mass in the cell m_i is identical to the volume integral over the reconstruction, $m_i = \int_{V_i} \rho(\boldsymbol{r}) \mathrm{d}^3 r$. An alternative choice for the reference point is to choose the mesh-generating point $\boldsymbol{r}_i$ instead of $\boldsymbol{s}_i$. This is the more natural choice if the cell values are known to sample the values of the underlying field at the location of the mesh-generating points, then the reconstruction is exact to linear order. However, our input quantities are cell-averages, which correspond to linear order to the values of the underlying field sampled at the centre-of-masses of the cells. For this reason we prefer the centre-of-mass of a cell as reference point for the reconstruction.

Nevertheless, this highlights that large spatial offsets between the centre-of-mass of a cell and its mesh-generating point are a source of errors in the linear reconstruction. It is therefore desirably to use "regular" meshes if possible, where the mesh-generating points lie close to the centre-of-mass; such meshes minimize the errors in the gradient estimation and the linear reconstruction. Or in other words, we would like our Voronoi meshes to be relatively close to so-called *centroidal Voronoi meshes*, where the mesh-generating points lie exactly in the centre of mass of each

cell. As we will discuss in more detail later, we have developed an efficient method for steering the mesh motion such that this regularity condition can be approximately maintained at all times (if desired).

In smooth parts of the flow, the above reconstruction is second-order accurate, with a stencil that consists of the local cell plus all adjacent cells. However, in order to avoid numerical instabilities the order of the reconstruction must be reduced near fluid discontinuities, such that the introduction of new extrema by over- or undershoots in the extrapolation is avoided. This is generally achieved by applying slope limiters that reduce the size of the gradients near local extrema, or by flux limiters that replace the high-order flux with a lower order version if there are steep gradients in the upstream region of the flow. These techniques allow the construction of total variation diminishing (TVD) schemes, in which spurious oscillations in solutions can be completely suppressed.

We here generalize the original MUSCL approach to an unstructured grid by enforcing monotonicity with a slope limiting of the gradients. To this end we require that the linearly reconstructed quantities on face centroids do not exceed the maxima or minima among all neighbouring cells (Barth & Jesperson, 1989). Mathematically, we replace the gradient with a slope-limited gradient

$$\langle \boldsymbol{\nabla}\phi \rangle_i' = \alpha_i \langle \boldsymbol{\nabla}\phi \rangle_i, \tag{28}$$

where the slope limiter $0 \le \alpha_i \le 1$ for each cell is computed as

$$\alpha_i = \min(1, \psi_{ij}). \tag{29}$$

Here the minimum is taken with respect to all cells j that are neighbours of cell i, and the quantity ψ_{ij} is defined as

$$\psi_{ij} = \begin{cases} (\phi_i^{\mathrm{max}} - \phi_i)/\Delta\phi_{ij} & \text{for} \quad \Delta\phi_{ij} > 0 \\ (\phi_i^{\mathrm{min}} - \phi_i)/\Delta\phi_{ij} & \text{for} \quad \Delta\phi_{ij} < 0 \\ 1 & \text{for} \quad \Delta\phi_{ij} = 0 \end{cases} \tag{30}$$

where $\Delta\phi_{ij} = \langle \boldsymbol{\nabla}\phi \rangle_i \cdot (\boldsymbol{f}_{ij} - \boldsymbol{s}_i)$ is the estimated change between the centroid $\boldsymbol{f}_{ij}$ of the face and the centre of cell i, and $\phi_i^{\mathrm{max}} = \max(\phi_j)$ and $\phi_i^{\mathrm{min}} = \max(\phi_j)$ are the maximum and minimum values occurring for ϕ among all neighbouring cells of cell i, including i itself.

We note that this slope limiting scheme does not strictly enforce the total variation diminishing property, which means that (usually reasonably small) post-shock oscillations are still possible. However, by choosing a slightly more conservative slope-limiter it is possible to obtain TVD behaviour, at the price of a more dissipative scheme (Barth & Ohlberger, 2004). Finally, we note that future refinements of the present method could also employ higher-order polynomial reconstruction schemes, for example based on a larger stencil and conservative least square reconstruction (e.g. Ollivier-Gooch, 1997). This would be similar in spirit to higher-order essentially non-oscillatory (ENO) or weighted ENO (WENO) schemes.

3.2 Setting the velocities of the mesh generators

A particular strength of the scheme we propose here is that it can be used both as an Eulerian code, and as a Lagrangian scheme. The difference lies only in the motion of the mesh-generation points. If the mesh-generating points are arranged on a Cartesian mesh and zero velocities are adopted for them, our method is identical to a second-order accurate Eulerian code[‡] on a structured grid. Of course, one can equally well choose a different layout of the points, in which case we effectively obtain an Eulerian code on an unstructured mesh. The real advantage of the new code can be realized when we allow the mesh to move, with a velocity that is tied to the local fluid speed. In this case, we obtain a Lagrangian hydrodynamics code, which has some unique and important advantages relative to an Eulerian treatment.

In fact, our code belongs to the general class of so-called Arbitrary Lagrangian-Eulerian (ALE) fluid dynamical methods. Unlike other ALE schemes, the method proposed here however does not rely on remapping techniques to recover from distortions of the mesh once they become severe, simply because the Voronoi tessellation produced by the continuous motion of the mesh-generating points yields a mesh geometry and topology that itself changes continuously in time, without any mesh-tangling effects. The motion of the mesh-generating points can be chosen nearly arbitrarily, including cases where it is prescribed by an external flow field, for example to smoothly concentrate resolution towards particular regions of a mesh. Also, as we shall discuss below, we may modify the flow of mesh-generating points such that certain desired properties of the fluid tessellation are maintained or achieved, e.g. a constant mass per cell, or that cell sizes are constrained to lie within prescribed minimal or maximal bounds.

The most simple and basic approach for specifying the motion of the mesh generators is to use

$$\boldsymbol{w}_i = \boldsymbol{v}_i, \tag{31}$$

i.e. the points are moved with the fluid speed of their cell. This ansatz is clearly appropriate for pure advection and in smooth parts of the flow. Whereas it is not strictly Lagrangian because it does not guarantee that the faces of the cells move with the local velocity and hence mass exchange can still occur between the cells, it nevertheless approximates Lagrangian behaviour by minimized the mass flux between cells. Also, it can be expected that this ansatz will roughly keep the mass per cell fixed, leading to an adaptive spatial resolution in situations with strong clustering of matter.

However, in this scheme there is no mechanism built in that tries to improve the regularity of the Voronoi mesh in case the mean mass per cell should develop substantial scatter around a desired mean value, or if a large number of cells with high aspect ratios occur. If desired, such tendencies of a growing mesh irregularity can be counteracted by adding corrective velocity components to the mesh velocities $\boldsymbol{w}_i$ given by equation (31). There are many different possibilities for how exactly to do this, and we consider this freedom a strength of the formalism. In Section 4, we will discuss a few simple regularization terms that we have explored thus far, and which have proven to be very effective.

[‡] There are of course many different variants of 2nd order Eulerian schemes. Our method corresponds to the well known MUSCL-Hancock approach.

3.3 Flux computation

An important aspect of our approach is that the specified motion of the mesh-generating points fully determines the motion of the whole Voronoi mesh, including, in particular, the velocities of the centroids of cell faces. This allows us to calculate the Riemann problem in the rest-frame of each of the faces.

Consider one of the faces in the tessellation and call the fluid states in the two adjacent cells the 'left' and 'right' states. We first need to determine the velocity $\boldsymbol{w}$ of the face based on the velocities $\boldsymbol{w}_\mathrm{L}$ and $\boldsymbol{w}_\mathrm{R}$ of the two mesh-generating points associated with the face (they are connected by a Delaunay edge). It is clear that $\boldsymbol{w}$ has a primary contribution from the mean velocity $(\boldsymbol{w}_\mathrm{L} + \boldsymbol{w}_\mathrm{R})/2$ of the points, but there is also a secondary contribution $\boldsymbol{w}'$ from the residual motion of the two points relative to their centre of mass. This residual motion is given by $\boldsymbol{w}'_\mathrm{R} = -\boldsymbol{w}'_\mathrm{L} = (\boldsymbol{w}_\mathrm{R} - \boldsymbol{w}_\mathrm{L})/2$, and we need to determine its impact on the motion of the face centroid. Figure 11 sketches the geometry of the situation. The components of $\boldsymbol{w}'_\mathrm{R}$ and $\boldsymbol{w}'_\mathrm{L}$ parallel to the line connecting the centroid $\boldsymbol{f}$ of the face with the midpoint $\boldsymbol{m}$ of the two mesh-generating points $\boldsymbol{r}_\mathrm{L}$ and $\boldsymbol{r}_\mathrm{R}$ induce a rotation of the face around the point $\boldsymbol{m}$. We are only interested in the normal velocity component of this motion at the centroid of the face. This can be easily computed as

$$\boldsymbol{w}' = \frac{(\boldsymbol{w}_\mathrm{L} - \boldsymbol{w}_\mathrm{R}) \cdot [\boldsymbol{f} - (\boldsymbol{r}_\mathrm{R} + \boldsymbol{r}_\mathrm{L})/2]}{|\boldsymbol{r}_\mathrm{R} - \boldsymbol{r}_\mathrm{L}|} \frac{(\boldsymbol{r}_\mathrm{R} - \boldsymbol{r}_\mathrm{L})}{|\boldsymbol{r}_\mathrm{R} - \boldsymbol{r}_\mathrm{L}|}. \tag{32}$$

The full velocity $\boldsymbol{w}$ of the face is then given by

$$\boldsymbol{w} = \frac{\boldsymbol{w}_\mathrm{R} + \boldsymbol{w}_\mathrm{L}}{2} + \boldsymbol{w}'. \tag{33}$$

We note that this result can also be used to calculate the rate of change of the volume of a cell i due to the motion of its neighbouring points, viz.

$$\frac{\mathrm{d}V_i}{\mathrm{d}t} = -\sum_{j \neq i} A_{ij} \left[\frac{\boldsymbol{c}_{ij}}{r_{ij}} \cdot (\boldsymbol{w}_j - \boldsymbol{w}_i) + \frac{\boldsymbol{r}_{ij}}{2r_{ij}} \cdot (\boldsymbol{w}_j + \boldsymbol{w}_i) \right], \tag{34}$$

where $\boldsymbol{r}_{ij} = \boldsymbol{r}_i - \boldsymbol{r}_j$ is the distance vector between the two points i and j (with $r_{ij} = |\boldsymbol{r}_{ij}|$), A_{ij} is the area of the common face, and $\boldsymbol{c}_{ij} = \boldsymbol{f}_{ij} - (\boldsymbol{r}_i + \boldsymbol{r}_j)/2$ is a vector pointing to the centre $\boldsymbol{f}_{ij}$ of the face from the midpoint between i and j. We note that the same result can also be obtained with equations (22) and (23).

We now calculate the flux across the face using the MUSCL-Hancock approach, with the important difference that we shall carry out the calculation in the rest-frame of the face. It is convenient to do this in the primitive variables $(\rho, \boldsymbol{v}, P)$, where we first transform the lab-frame velocities of the two cells to the rest-frame by subtracting $\boldsymbol{w}$,

$$\boldsymbol{W}'_{\mathrm{L,R}} = \boldsymbol{W}_{\mathrm{L,R}} - \begin{pmatrix} 0 \\ \boldsymbol{w} \\ 0 \end{pmatrix}. \tag{35}$$

We then linearly predict the states on both side to the centroid of the face, and also predict them forward in time by half a timestep. This produces the states

$$\boldsymbol{W}''_{\mathrm{L,R}} = \boldsymbol{W}'_{\mathrm{L,R}} + \left.\frac{\partial \boldsymbol{W}'}{\partial r}\right|_{\mathrm{L,R}} (\boldsymbol{f} - \boldsymbol{s}_{\mathrm{L,R}}) + \left.\frac{\partial \boldsymbol{W}'}{\partial t}\right|_{\mathrm{L,R}} \frac{\Delta t}{2}. \tag{36}$$
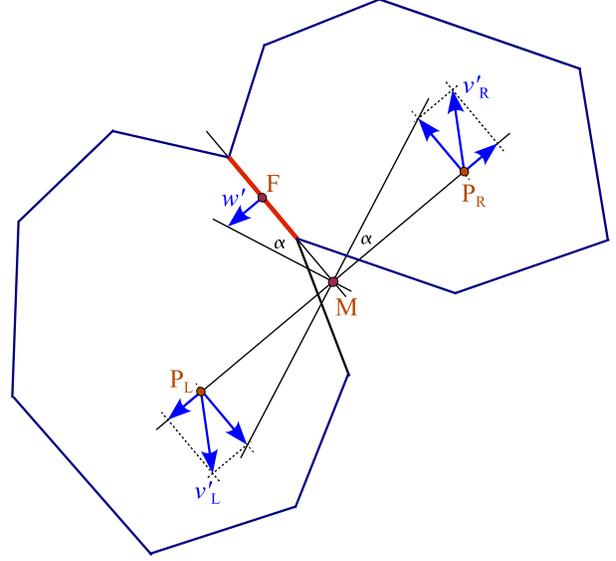

Figure 11. Sketch illustrating the calculation of the normal velocity of a face based on the motion of its two associated mesh-generating points.

The spatial derivatives $\partial \boldsymbol{W}'/\partial \boldsymbol{r}$ are known, and given by the (slope-limited) gradients of the primitive variables that are estimated as described in Section 3.1. Note that the gradients are unaffected by the change of rest-frame described by Eqn. (35). The partial time derivate $\partial \boldsymbol{W}/\partial t$ can be replaced by spatial derivatives as well, based on the Euler equations in primitive variables, which are given by

$$\frac{\partial \boldsymbol{W}}{\partial t} + \boldsymbol{A}(\boldsymbol{W}) \frac{\partial \boldsymbol{W}}{\partial \boldsymbol{r}} = 0, \tag{37}$$

where $\boldsymbol{A}$ is the matrix

$$\boldsymbol{A}(\boldsymbol{W}) = \begin{pmatrix} \boldsymbol{v} & \rho & 0 \\ 0 & \boldsymbol{v} & 1/\rho \\ 0 & \gamma P & \boldsymbol{v} \end{pmatrix}. \tag{38}$$

Having finally obtained the states left and right of the interface, we need to turn them into a coordinate system aligned with the face, such that we can solve an effectively one-dimensional Riemann problem. The required rotation matrix $\boldsymbol{\Lambda}$ for the states only affects the velocity components, viz.

$$\boldsymbol{W}'''_{\mathrm{L,R}} = \boldsymbol{\Lambda} \, \boldsymbol{W}''_{\mathrm{L,R}} = \begin{pmatrix} 1 & 0 & 0 \\ 0 & \boldsymbol{\Lambda}_{\mathrm{3D}} & 0 \\ 0 & 0 & 1 \end{pmatrix} \boldsymbol{W}''_{\mathrm{L,R}}, \tag{39}$$

where $\boldsymbol{\Lambda}_{\mathrm{3D}}$ is an ordinary rotation of the coordinate system, such that the new x-axis is parallel to the normal vector of the face, pointing from the left to the right state.

With these final states, we now solve the Riemann problem, and sample the self-similar solution along $x/t = 0$. This can be written as

$$\boldsymbol{W}_\mathrm{F} = R_{\mathrm{iemann}}(\boldsymbol{W}'''_\mathrm{L}, \boldsymbol{W}'''_\mathrm{R}), \tag{40}$$

where R_{iemann} is a one-dimensional Riemann solver, which returns a solution for the state of the fluid $\boldsymbol{W}_\mathrm{F}$ on the face in primitive variables. We now transform this back to the lab-frame, reversing the steps above,

$$\boldsymbol{W}_{\mathrm{lab}} = \begin{pmatrix} \rho \\ \boldsymbol{v}_{\mathrm{lab}} \\ P \end{pmatrix} = \Lambda^{-1}\boldsymbol{W}_{\mathrm{F}} + \begin{pmatrix} 0 \\ \boldsymbol{w} \\ 0 \end{pmatrix}. \qquad (41)$$

Finally, we can use this state to calculate the fluxes in the conserved variables across the face. Here we need to take into account that the *face is moving* with velocity $\boldsymbol{w}$, meaning that the appropriate flux vector in the lab frame is given by

$$\hat{\boldsymbol{F}} = \boldsymbol{F}(\boldsymbol{U}) - \boldsymbol{U}\boldsymbol{w}^{\mathrm{T}} = \begin{pmatrix} \rho(\boldsymbol{v}_{\mathrm{lab}} - \boldsymbol{w}) \\ \rho\boldsymbol{v}_{\mathrm{lab}}(\boldsymbol{v}_{\mathrm{lab}} - \boldsymbol{w})^{\mathrm{T}} + P \\ \rho e_{\mathrm{lab}}(\boldsymbol{v}_{\mathrm{lab}} - \boldsymbol{w}) + P\boldsymbol{v}_{\mathrm{lab}} \end{pmatrix}, \quad (42)$$

where $\boldsymbol{U}$ is the state $\boldsymbol{W}_{\mathrm{lab}}$ expressed in the conserved variables, and $e_{\mathrm{lab}} = \boldsymbol{v}_{\mathrm{lab}}^2/2 + P_{\mathrm{lab}}/[(\gamma-1)\rho_{\mathrm{lab}}]$. The scalar product of this flux vector with the normal vector of the face gives the net flux of mass, momentum, and energy that the two adjacent, moving cells exchange. It is the flux of equation (42) that can finally be used in the conservative updates of each cell, as described by equation (13).

3.4   Galilean invariance

In the above scheme, it is clear that the state $\boldsymbol{W}_{\mathrm{F}}$ sampled from the Riemann solver is invariant under Galilean transformations, because a special invariant frame for evaluation of the Riemann problem is adopted, that of the face moving with the flow. As a result, the input left and right states are invariant under a Galilean boost; any such boost is simply absorbed into the motion of the face. This also means that the velocity difference $\boldsymbol{u} \equiv (\boldsymbol{v}_{\mathrm{lab}} - \boldsymbol{w})$ appearing in the flux of equation (42) is invariant as well. It is thus clear that the mass flux between cells is Galilean-invariant, but this property is much less evident for the momentum and energy fluxes, as they still have an additional dependence on the velocity $\boldsymbol{v}_{\mathrm{lab}}$ in the lab-frame, as seen in Eqn. (42).

Recall that the desired invariance means that it should not matter whether we evolve the state of a cell in the current lab-frame, or in a reference frame that is boosted by a constant velocity relative to it. In both cases, we should obtain the same final state when compared again in the same frame.

We can demonstrate this property for the above scheme as follows. Let us assume for simplicity that there is only one flux vector in or out of a cell. When calculated in the current lab-frame, the new state after a timestep Δt will then be

$$\boldsymbol{Q}^{\mathrm{new}} = \begin{pmatrix} Q_0 \\ \boldsymbol{Q}_1 \\ Q_2 \end{pmatrix} + \begin{pmatrix} \rho\,\boldsymbol{u} \\ \rho\,\boldsymbol{v}_{\mathrm{lab}}\,\boldsymbol{u}^{\mathrm{T}} + P \\ \rho\,e_{\mathrm{lab}}\boldsymbol{u} + P\,\boldsymbol{v}_{\mathrm{lab}} \end{pmatrix} \boldsymbol{A}\Delta t, \qquad (43)$$

where $\boldsymbol{A}$ is the normal vector of the face, and Q_0, $\boldsymbol{Q}_1$, and Q_2 are mass, momentum and energy of the cell at the beginning.

Let the function $G(\boldsymbol{Q}, \boldsymbol{v})$ return the state vector $\boldsymbol{Q}'$ of conserved quantities of a cell in a frame that is moving with a constant velocity relative to the current frame. For a Galilean boost with velocity $\boldsymbol{v}_0$, the new state is given by

$$\boldsymbol{Q}' = G(\boldsymbol{Q}, \boldsymbol{v}_0) \qquad (44)$$

where

$$G(\boldsymbol{Q}, \boldsymbol{v}) = \begin{pmatrix} Q_0 \\ \boldsymbol{Q}_1 + Q_0\boldsymbol{v} \\ Q_2 + \boldsymbol{Q}_1 \cdot \boldsymbol{v} + \frac{1}{2}Q_0\boldsymbol{v}^2 \end{pmatrix} \qquad (45)$$

defines the boost transformation. We can now evolve this boosted state over one timestep, which yields

$$\boldsymbol{Q}'' = \boldsymbol{Q}' + \begin{pmatrix} \rho\,\boldsymbol{u} \\ \rho\,(\boldsymbol{v}_{\mathrm{lab}} + \boldsymbol{v}_0)\,\boldsymbol{u}^{\mathrm{T}} + P \\ \rho\,e'_{\mathrm{lab}}\boldsymbol{u} + P\,(\boldsymbol{v}_{\mathrm{lab}} + \boldsymbol{v}_0) \end{pmatrix} \boldsymbol{A}\Delta t, \qquad (46)$$

where $e'_{\mathrm{lab}} = e_{\mathrm{lab}} + \boldsymbol{v}_{\mathrm{lab}}\boldsymbol{v}_0 + \frac{1}{2}\boldsymbol{v}_0^2$. The flux is here different because $\boldsymbol{v}_{\mathrm{lab}}$ transform to $\boldsymbol{v}_{\mathrm{lab}} + \boldsymbol{v}_0$ in the boosted frame. Finally, we can take the state $\boldsymbol{Q}''$ back to our original frame, by calculating

$$\tilde{\boldsymbol{Q}}^{\mathrm{new}} = G(\boldsymbol{Q}'', -\boldsymbol{v}_0). \qquad (47)$$

Our scheme is Galilean invariant if this state $\tilde{\boldsymbol{Q}}^{\mathrm{new}}$ agrees with the state (43) obtained by evolving the cell in the original system. Inserting equations (44), (45) and (46) into (47), and after a bit of algebra, it is seen that this is indeed the case. This is an extremely important property not shared by ordinary Eulerian codes.

As a word of caution, we note that the finite numerical round off errors always present in ordinary floating point arithmetic will perturb the exact Galilean invariance of our discretization scheme in practice. In particular, since the conserved quantities are always stored in the lab-frame, the effective number of significant bits left for the internal energy will be reduced for very large bulk velocities, as it is then defined as the difference of two large numbers. However, with double precision arithmetic this may only become a problem for really extremely large Mach numbers, and it could always be solved by the use of extended floating point precision if needed.

3.5   Poorly resolved cold flows

It is a well known problem in Eulerian finite volume methods that flows that are dominated by their kinetic energy – or in other words are very cold and move supersonically with respect to the calculational frame – often exhibit spurious heating in adiabatic parts of the flow. This arises from small amounts of dissipation occurring in the cold gas, introduced by finite discretization errors. Better spatial resolution alleviates the problem, but if the gas is sufficiently cold, even very small dissipative effects become readily visible in the evolution of the gas temperature. Whereas the pressure forces remain typically negligible as a result of this effect and hence do not change the gas motion itself, the temperature evolution can be very seriously in error. Unfortunately, this problem is ubiquitous in cosmology, where the early phases of structure formation always involve very cold gas combined with relatively large velocities that are induced by gravity, resulting in extremely high Mach numbers. If the spurious dissipation is not prevented, the temperature of the low-density intergalactic medium can not be trusted and becomes unusable for quantitative analysis.

Different solutions have been developed in the literature to cope with this problem (which incidentally is absent in the SPH formalism, see e.g. Springel & Hernquist, 2002). Ryu et al. (1993) evolve the entropy of the gas as an additional conserved quantity and define a number of criteria for deciding whether the energy or the entropy equation should be used. Bryan et al. (1995) on the other hand propose a 'dual energy formalism', where the internal gas energy is

evolved in addition to the total energy. When the gas motion is highly supersonic, the temperature and pressure of the gas are set based on the result of the internal energy equation, while otherwise the total energy is used.

The Galilean-invariance of the moving mesh code suggests that it should in principle have fewer problems with highly supersonic flow. However, if the velocity differences from cell to cell are of the order of the local sound speed or larger, we find that the moving mesh code can also give rise to spurious dissipation in the cold gas and as a result can produce an incorrect temperature evolution. The problem is that in adiabatically evolving gas, any small difference between the total energy and kinetic energy of a cell automatically appears in the thermal energy. Even if the discretization errors from fluid advection are quite small, equal to only a small fraction of the total energy of a cell, these errors will give rise to spurious changes of the temperature if the thermal energy is comparably small.

A related problem arises in simulations that are coupled to a collisionless dark matter or stellar component. The collisionless fluid often dominates the gravitational field, and is usually treated with the gravitational N-body approach. The problem is that the resulting gravitational force field is relatively noisy, and imparts a stochastic driving onto the gas as it flows through the bumpy potential provided by the N-body system. We have found that the resulting small-scale velocity fluctuations are readily dissipated away by the mesh-based hydrodynamics, giving rise to a significant spurious heating of the gas. Interestingly, SPH is much less susceptible to this effect, presumably because of its much poorer ability to detect very weak shocks. Part of the heating effect can be readily understood by the analysis of Steinmetz & White (1997), who showed that two-body encounters between collisionless particles and fluid elements induce substantial heating in the gas. In numerical experiments with cold gaseous disks in isolated galaxies with live N-body dark matter halos, we have found that the effect in the finite volume hydrodynamics is even stronger than expected based on Steinmetz & White (1997), presumably because the gas also reacts strongly to slower moving collisionless particles that are not well treated by the impulse approximation. We also found that the heating can only be efficiently suppressed if either an extremely large number of N-body particles is used, or a smooth analytic potential is employed. But such large particle numbers are impractical in many applications, and also not needed in the SPH approach. We therefore seek a method that can suppress the spurious heating of the gas through the N-body component, if needed.

To circumvent the problems described above, we adopt a solution that is similar to that of Ryu et al. (1993), but differs in a number of important aspects. We first define a measure of the total entropy of a cell as

$$S_i = M_i A_i = M_i \frac{P_i}{\rho_i^\gamma}, \tag{48}$$

where $A_i \equiv P_i/\rho_i^\gamma$ is an entropic function that effectively labels the entropy per unit mass of the gas, and γ is the adiabatic index. Note however that the quantity S is not the thermodynamic entropy itself, but is related to it through a simple monotonic relation. In fact, for a monoatomic ideal gas the thermodynamic entropy S_{therm} per particle is given by

$$\frac{S_{\text{therm}}}{N} = \frac{3}{2} k_{\text{B}} \left[\ln \left(\frac{S}{N} \right) + \ln \left(\frac{2\pi m^{5/3}}{h^2} \right) + \frac{5}{3} \right], \tag{49}$$

where N is the number of atoms, m their mass, and h is Planck's constant. For simplicity, we will call S the total entropy, as it is simpler to work with than using the thermodynamic entropy directly.

The Euler equations show that outside of shocks, S is a *conserved quantity*. We can hence add a further hyperbolic conservation law of the form

$$\frac{\partial}{\partial t}(\rho A) + \boldsymbol{\nabla} \cdot (\rho A \boldsymbol{v}) = 0 \tag{50}$$

to the set of equations we solve in our finite volume scheme, and treat S_i as a further component in the vector $\boldsymbol{Q}_i$ of conserved quantities for each cell. Furthermore, we may optionally replace the primitive variable P_i with the entropic function $A_i = S_i/M_i$ of a cell. For the vector of primitive variables $\boldsymbol{W} = (\boldsymbol{\rho}, \boldsymbol{v}, \boldsymbol{A})$, the Euler equations can in this case be written as

$$\frac{\partial \boldsymbol{W}}{\partial t} + \boldsymbol{B}(\boldsymbol{W}) \frac{\partial \boldsymbol{W}}{\partial \boldsymbol{r}} = 0, \tag{51}$$

where $\boldsymbol{B}$ is the matrix

$$\boldsymbol{B}(\boldsymbol{W}) = \begin{pmatrix} \boldsymbol{v} & \rho & 0 \\ \gamma A \rho^{\gamma-2} & \boldsymbol{v} & \rho^{\gamma-1} \\ 0 & 0 & \boldsymbol{v} \end{pmatrix}. \tag{52}$$

This again shows that A stays constant along the flow, making this variable particularly convenient to characterize adiabatic motion.

We can now apply our usual gradient estimation, spatial reconstruction and slope limiting procedures to the entropic function A_i (in addition to, or instead of, the pressure). When the pressure is needed, for example as input to the Riemann problem, it is calculated as $P = A\rho^\gamma$. Finally, we compute additional flux components at each cell face, namely the entropy fluxes corresponding to equation (50), and use them to update the entropies S_i of all cells, keeping the sum of the total entropy constant. At each cell face, we take the entropy flux to be $\rho_{\text{F}} v_{\text{F}} A_{\text{U}}$, where ρ_{F} and v_{F} are the density and normal velocity returned by the Riemann solver, while A_{U} is chosen equal to the entropic function of the *upwind side* of the Riemann problem (i.e. A_{U} is either equal to A_{L} or A_{R}), which we select based on the sign of v_{F}. This hence advects the entropy assuming that the flow is smooth.

However, normally the result of this entropy advection is *discarded* at the end of each timestep. Instead, we *reinitialize* the entropy S_i of each cell based on the updated values of total energy, total momentum and mass. This takes care of the fact that in general the entropy will not be conserved after all. It will tend to increase, either through dissipative processes in shock fronts as captured by the analytic Riemann solution, or as a result of the mixing entropy that is generated when the Riemann solution is averaged over a cell and mapped back to a piece-wise constant state. The entropy conservation law (50) is therefore essentially redundant in finite volume methods because the other conservation laws already fully determine the final averaged state of the cell. This is why in an ordinary Godunov scheme the entropy is normally not considered explicitly, the scheme automatically injects exactly the right amount of entropy to satisfy the conservation laws of total energy, momentum and mass.
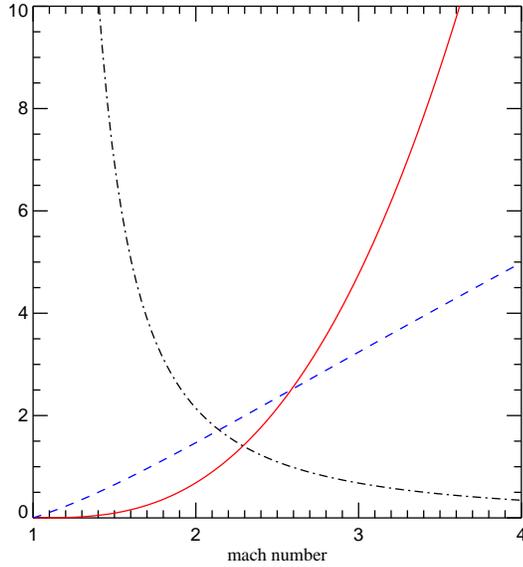
Figure 12. Dissipative heating rate $f_{\mathrm{diss}}(\mathcal{M})$ in a shock as a function of Mach number $\mathcal{M}$ (red solid line), for a $\gamma = 5/3$ gas. The dashed blue line gives the adiabatic heating rate $f_{\mathrm{adiab}}(\mathcal{M})$ of the gas as it is compressed at the shock. Finally, the dotted line gives the ratio of adiabatic and dissipative heating rates.

However, if the flow is poorly resolved and very cold, or if it is governed by a noisy external gravitational field, we may give precedence to the entropy conservation law over that for the total energy, provided the flow is sufficiently smooth. This can be simply accomplished by keeping the updated entropy S_i of a cell at the end of a timestep, thereby suppressing local dissipation. Instead of reinitializing the entropy with the help of the total energy equation, the entropy is then used together with the new density to update the thermal energy, and hence the pressure. In this case there is no spurious heating of the gas in parts of the flow that are dominated by their kinetic energy, or are cold and poorly resolved. Instead, the temperature will evolve adiabatically, as expected for a smooth flow. The catch is that this procedure temporarily gives up manifest conservation of total energy, as the thermal energy is now not defined as a difference between total energy and kinetic energy, but rather based on the value expected for isentropic evolution of the gas. The resulting errors should normally be negligible however if the entropy scheme is only applied when the thermal energy is a negligible part of the total energy, and the pressure forces are unimportant.

The above discussion makes it clear that an important part of this method is the specific criterion used to decide whether a sufficiently smooth, poorly resolved cold flow is actually present, and hence a dissipative update of the entropy via the total energy equation can be delayed. We presently use the following simple criteria for this purpose.

Our primary criterion relies on directly detecting the presence of shocks with the help of the Riemann problem that we solve for each face. The Riemann problem yields a contact wave that is sandwiched on both sides either by a shock wave or a rarefaction fan. The Mach number(s) of the shock(s) present in the Riemann problem can be easily

determined. We hence can find for each cell the maximum Mach number that occurs in any of the Riemann problems of its surrounding faces. The idea is to only use the entropy equation whenever this maximum Mach number is smaller than a prescribed threshold value.

To examine the consequences of such a scheme, we recall the irreversible thermal dissipation rate of shock as a function of its Mach number. For a shock propagating with Mach number $\mathcal{M} = v_1/c_1$ into a medium of density ρ_1, soundspeed c_1 and thermal energy per unit mass u_1, the dissipative increase in thermal energy per unit time and unit shock surface area $\mathrm{d}F$ can be written as (see also Pfrommer et al., 2006)

$$\frac{\mathrm{d}E_{\mathrm{diss}}}{\mathrm{d}t\,\mathrm{d}F} = \rho_1 v_1 \rho_2^{\gamma-1}(A_2 - A_1)/(\gamma - 1), \tag{53}$$

where A_1 and A_2 are the pre- and postshock entropic functions, and ρ_2 is the postshock density. The adiabatic heating rate just from the reversible compression of the gas is given by

$$\frac{\mathrm{d}E_{\mathrm{adiab}}}{\mathrm{d}t\,\mathrm{d}F} = \rho_1 v_1 (\rho_2^{\gamma-1} - \rho_1^{\gamma-1})A_1/(\gamma - 1). \tag{54}$$

The jumps in density and entropy can be expressed in terms of Mach number only:

$$f_\rho(\mathcal{M}) \equiv \frac{\rho_2}{\rho_1} = \frac{(\gamma+1)\mathcal{M}^2}{(\gamma-1)\mathcal{M}^2 + 2}, \tag{55}$$

$$f_A(\mathcal{M}) \equiv \frac{A_2}{A_1} = \frac{2\gamma\mathcal{M}^2 - (\gamma-1)}{\gamma+1}\left[\frac{(\gamma-1)\mathcal{M}^2 + 2}{(\gamma+1)\mathcal{M}^2}\right]^\gamma. \tag{56}$$

This allows us to express the dissipative heating rate as

$$\frac{\mathrm{d}E_{\mathrm{diss}}}{\mathrm{d}t\,\mathrm{d}F} = \rho_1 u_1 c_1\, f_{\mathrm{diss}}(\mathcal{M}), \tag{57}$$

with

$$f_{\mathrm{diss}}(\mathcal{M}) = \mathcal{M}[f_A(\mathcal{M}) - 1]f_\rho^{\gamma-1}(\mathcal{M}). \tag{58}$$

This shows the well-known result that the dissipation rate in a shock depends very sensitively on Mach number, $f_{\mathrm{diss}}(\mathcal{M}) \propto (\mathcal{M} - 1)^3$. Similarly, we can write the heating rate from the adiabatic shock compression as

$$\frac{\mathrm{d}E_{\mathrm{adiab}}}{\mathrm{d}F\,\mathrm{d}t} = \rho_1 u_1 c_1\, f_{\mathrm{adiab}}(\mathcal{M}), \tag{59}$$

with

$$f_{\mathrm{adiab}}(\mathcal{M}) = \mathcal{M}[f_\rho^{\gamma-1}(\mathcal{M}) - 1]. \tag{60}$$

Note that the adiabatic heating rate increases more slowly with Mach number than the dissipation, $f_{\mathrm{adiab}}(\mathcal{M}) \propto (\mathcal{M} - 1)$. For very low Mach numbers, the adiabatic heating strongly dominates, and the dissipative heating becomes comparatively unimportant. This is shown in Figure 12, where we plot the factors $f_{\mathrm{diss}}(\mathcal{M})$ and $f_{\mathrm{adiab}}(\mathcal{M})$ as a function of Mach number, as well as their ratio.

This suggests to use a threshold Mach number $\mathcal{M}_{\mathrm{thresh}}$ for deciding whether the entropy equation may be used to update a cell instead of the total energy equation. If we pick $\mathcal{M}_{\mathrm{thresh}} \sim 1.1$ and use the entropy equation only if the maximum Mach number of all shocks in the Riemann problems surrounding the cell lies below this number, then the entropy production of very weak shocks that are associated with spurious dissipation is suppressed. The flow is effectively treated as being smooth and adiabatic. Note that if

real weak shocks of this small strength are present, they still nevertheless have the correct adiabatic heating rate, which strongly dominates for these weak shocks (by a factor of more than 100 for $\mathcal{M} < 1.1$), suggesting that errors in the dynamics should be very minor. Indeed, we have found that this scheme works especially well for suppressing artificial heating of the gas from the Poisson noise in the gravitational field of a N-body system. In this case we have also not been able to find any detrimental impact on the quality with which the total energy is conserved (on the contrary actually), which we recall is not manifestly conserved in self-gravitating systems.

As an alternative to the Mach number switch discussed above, we have also implemented a scheme that compares the thermal energy of a cell with a suitably defined kinetic energy in order to determine whether a flow is cold. This is more similar to the approach of Bryan et al. (1995) and Ryu et al. (1993). In practice, we first determine the expected new thermal energy $E_{\mathrm{therm}} = E_{\mathrm{tot}} - M\boldsymbol{v}^2/2$ at the end of the timestep, based on the usual conservation laws. If this energy is much smaller than the maximum kinetic energy $E_{\mathrm{kin}}^{\mathrm{max}}$ among the cell and all its neighbouring cells,

$$E_{\mathrm{therm}} < \alpha_S \, E_{\mathrm{kin}}^{\mathrm{max}}, \tag{61}$$

then the flow is is considered 'cold' and the entropy is kept and not updated in this step. We typically use $\alpha_S \sim 0.01$ for the parameter α_S, but the results are not sensitive to this choice provided one ensures that one switches back to the "normal" treatment of the hydrodynamics once a sufficiently strong dissipative event occurs.

In the Lagrangian mode of the code, we define the kinetic energy $E_{\mathrm{kin}}^{\mathrm{max}}$ of the neighbouring fluid cells relative to the velocity $\boldsymbol{w}_i$ of the current cell. In this way, the criterion (61) becomes Galilean invariant and effectively compares the local sound speed with the size of the velocity changes from cell to cell. Sometimes this renders the criterion too restrictive, however, especially in simulations with self-gravity. We then invoke a further condition,

$$E_{\mathrm{therm}} < \beta_S \, M_i \, g_i \, R_i, \tag{62}$$

which effectively compares the strength of pressure forces to the gravitational acceleration. Here R_i is the 'radius' of the cell (see below), and g_i is the magnitude of the local gravitational acceleration. If one of the conditions (61) or (62) is fulfilled, the entropy is kept for the current step. This is based on the idea that if the pressure forces are negligible compared to the gravitational forces, we are dealing with an effectively kinematically dominated flow, and it then makes sense to keep the entropy as this provides for a more accurate temperature evolution.

Note that the scheme described in this subsection is an optional treatment in the AREPO code. Even if enabled, there is no difference to the ordinary conservative hydrodynamics for sufficiently small values of $\mathcal{M}_{\mathrm{thresh}}$, or α_S and β_S. Also, if these parameters are set to unreasonably large values and the entropy production is artificially suppressed, the dynamics is often still represented surprisingly accurately. This is because weak shocks produce only little new entropy. Even if this entropy production is ignored, the Riemann solver still recovers the correct jumps in density and velocity and rescues the dynamics.

3.6 Boundary conditions

We have implemented two simple boundary conditions thus far, periodic boundaries and reflective boundaries. In both cases, the computational domain is restricted to be a rectangular domain of arbitrary aspect ratio. The implementation of periodic boundaries is realized with the ghost cell technique discussed earlier. Even if only a single processor is used, particles close to the edge of the domain will find periodic image particles 'on the other side' of the principal domain, and import those as ghost particles. While this means that the cells that overlap with the box boundaries will be duplicated in the mesh construction, the overhead in mesh storage this induces is small. But the convenience of this approach lies in the fact that it does not require a modification of the actual mesh construction algorithms to make them aware of the periodic boundaries. Also, this simple technique is readily combined with the approach we adopted to cope with distributed-memory parallelization.

Reflective boundaries can be realized similarly, except that ghost particles are now not simply primary particles/cells that are translated by one box-length. Instead, the spatial location of ghost particles correspond to *mirrored* copies of the primary mesh-generation points. When added to the primary points, this means that the resulting Voronoi mesh for the principal domain will always have faces aligned with the box boundaries. It is then possible to impose different boundary conditions on these faces. For reflective boundaries, we can simply copy the state of the fluid from the mirrored point, but with the sign of the normal velocity component reversed. This will automatically make the mass flux vanish on the surface of the boundary, and leads to reflective boundary conditions. However, it is also easily possible with this mirroring technique to realize outflow or inflow boundary conditions. Finally, it is possible to arrange for arbitrary curve-linear boundary conditions by arranging two parallel strings of paired particles in a suitable way. One of the particles of each pair would constitute a cell inside the computational domain, the other would be a fiducial cell outside, and the desired boundary condition can be imprinted at the face they share. If desired, such a boundary may also be moved in complex ways. We will discuss an illustrative example of this technique in subsection 8.9.

4 MESH REGULARITY

As seen in Figure 1, Voronoi meshes may sometimes look quite "irregular", in the sense that there is a significant spread in sizes and aspect ratios of the cells, especially for sufficiently disordered point distributions. While this is not a problem of principle for our approach, it is clear that the computational efficiency will normally be optimized if regions of similar gas properties are represented with cells of comparable size. Having a mixture of cells of greatly different volumes to represent a gas of constant density will restrict the size of the timestep unnecessarily (which is determined by the smallest cells), without giving any giving a benefit in spatial resolution (which will be limited by the largest cells in the region).

As we have seen, it is also desirable to have cells where the centre-of-mass lies close to the mesh-generating point,

because this minimizes errors in the linear reconstruction and limits the rate at which mesh faces turn their orientation during mesh motion. Below, we will discuss our approaches for steering the mesh motion during the dynamical evolution such that, if desired, mesh regularity in the above sense can be achieved and maintained.

4.1   Making cells 'rounder'

In so-called centroidal Voronoi tessellations, the mesh-generating points coincide with the centre-of-mass of all cells. There is an amazingly simple algorithm known as Lloyd's method (Lloyd, 1982) to obtain a centroidal Voronoi tessellation starting from an arbitrary tessellation. One simply moves the mesh-generating points of the current Voronoi tessellation to the centre-of-masses of their cells, and then reconstructs the Voronoi tessellation. The process is repeated iteratively, and with each iteration, the mesh relaxes more towards a honey-web like configuration in which the Voronoi cells appear quite 'round' and have similar volume – a centroidal Voronoi tessellation. This is illustrated in Figure 13, which shows the Voronoi tessellation of a Poisson distribution of 625 points in 2D, and the result of 50 Lloyd iterations applied to it.

Inspired by this algorithm, we (optionally) employ a simple scheme to improve the local shape of the Voronoi tessellation during the dynamical evolution. We simply augment equation (31) with an additional velocity component, which is designed to move a given mesh-generating point towards the centre-of-mass of its cell. There are different possibilities to parameterize such a corrective velocity. One approach that we found to work very well in practice is to add a correction velocity whenever the mesh-generating point is further away from the centre-of-mass of a cell than a given threshold, irrespective of the actual velocity field of the gas. To this end, we associate a radius $R_i = (3V_i/4\pi)^{1/3}$ with a cell based on its volume (or area in 2D). If the distance d_i between the cell's centre-of-mass $\boldsymbol{s}_i$ and its mesh-generating point $\boldsymbol{r}_i$ exceeds some fraction η of the cell radius R_i, we add a corrective term proportional to the local sound speed c_i of the cell to the velocity of the mesh-generating point. This effectively applies one Lloyd iteration (or a fraction of it) to the cell by repositioning the mesh-generating point onto the current centre-of-mass, ignoring other components of the mesh motion. In order to soften the transition between no correction and the full correction, we parameterize the velocity as

$$\boldsymbol{w}_i' = \boldsymbol{w}_i + \chi \begin{cases} 0 & \text{for } d_i/(\eta\,R_i) < 0.9 \\ c_i \frac{\boldsymbol{s}_i - \boldsymbol{r}_i}{d_i} \frac{d_i - 0.9\,\eta R_i}{0.2\,\eta R_i} & \text{for } 0.9 \le d_i/(\eta\,R_i) < 1.1 \\ c_i \frac{\boldsymbol{s}_i - \boldsymbol{r}_i}{d_i} & \text{for } 1.1 \le d_i/(\eta\,R_i) \end{cases} \quad (63)$$

but the detailed width of this transition is unimportant. In very cold flows the sound speed may be so low that the correction becomes ineffective. As an alternative, we therefore also implemented an option in the code that allows a replacement of $c_s(\boldsymbol{s}_i - \boldsymbol{r}_i)/d_i$ in equation (63) with $(\boldsymbol{s}_i - \boldsymbol{r}_i)/\Delta t$. This more aggressive approach to ensure round cells generally works very well too, but has the disadvantage to depend on the timestepping. Our typical choice for the threshold of the correction is $\eta = 0.25$, and we usually set $\chi = 1.0$, i.e. the correction is, if present, applied in full over the course of one

timestep. Smaller values of η can be used to enforce round cell shapes more aggressively, if desired. Smaller values of χ can be used to apply the corrective velocity more gently in time, but we have not noticed problems with the choice of $\chi = 1.0$ in the problems we examined thus far.

Because only relatively regular meshes have their centres of mass always close to their mesh-generating points, the extra velocity component has the tendency to make the local mesh more regular. Indeed, the above scheme is quite effective in maintaining low aspect rations for the mesh cells at all times during the evolution. We therefore found it to be a good default choice for general simulations with the moving mesh approach. Note that for a reasonably 'roundish' mesh, the correction velocity vanishes and the mesh will be strictly advected with the fluid in smooth parts of the flow.

4.2   Maintaining constant mass or volume for the cells

In many applications in cosmology, it is desirable to have constant mass resolution, and to increase/decrease the spatial resolution automatically when matter clusters or expands. If the mesh-generating points are moved with the local fluid velocity, the gas mass in the cells will stay very nearly constant, thus approximately fulfilling this desired Lagrangian adaptivity during the course of a simulation. However, some scatter in the mass per cell will nevertheless occur after a while, and in complicated flows with strong compressions and shocks, these fluctuations may reach factors of several. This calls for a method that is automatically able to restore and maintain a constant mass per cell.

Similarly, we would sometimes like to impose constraints on the volumes of cells as well, for example by requesting that they should not exceed a maximum size, or not become smaller than a prescribed scale. A special case of this are simulations where one would like to have roughly constant volume per cell, even though large density contrasts develop and at the same time the mesh should still move with the local flow velocity as far as possible.

In many practical applications, one may in fact request that both the mass and the volume of cells respect certain regularity conditions. For example, in situations where a self-gravitating clump of gas (say a galaxy) is embedded in large regions of essentially empty space, it would be best to have cells of nearly equal volume in the region that are largely (or completely) devoid of gas. (In fact, equal mass per cell would be ill-defined in this case as it basically meant that a single cell would have to represent all of this volume.) On the other hand, in the regions where the density is large, it would at the same time be desirable to have equal mass per cell.

We have implemented a scheme to regulate the mesh motion which effectively ensures that such prescribed constraints are respected by the moving mesh. Our method is inspired by the Zeldovich approximation and requires the solution of a Poisson-like equation. It is very powerful as it can eliminate even large-scale deviations from the desired distribution of cells in very few steps, as we discuss next.

Let $n(\boldsymbol{x})$ describe the current number density distribution of mesh-generating points. Let us suppose that this distribution is not quite ideal yet for the given density field of the gas, according to some suitable criterion, but that
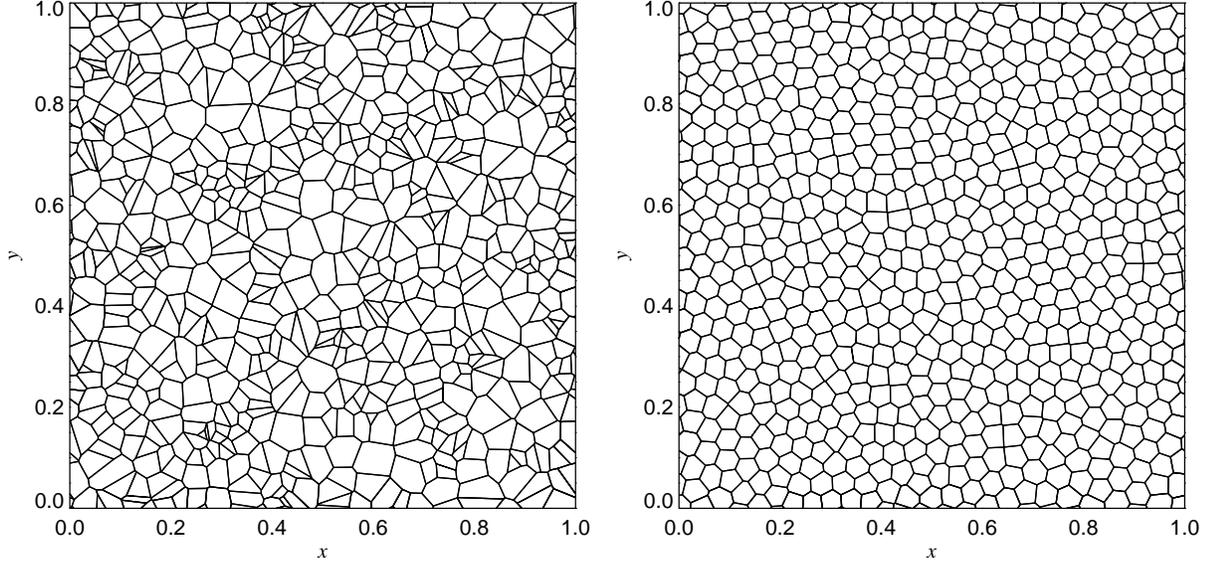
Figure 13. Example for a mesh regularization with Lloyd's algorithm. The panel on the left shows the Voronoi mesh of a Poisson sample of 625 points in the unit square, with periodic boundary conditions. The panel on the right hand side is the same mesh after being evolved with 50 iterations of Lloyd's algorithm, i.e. in each step the mesh-generating points are moved to the centre-of-mass of their cell. The mesh slowly 'crystallizes' into a quite regular structure with mostly hexahedral cells that are of very similar volume.

it is not too far away from the ideal distribution $n_0(\boldsymbol{x})$. In the following we will assume that linear order is sufficient to describe the differences between the current and the ideal distribution of the mesh-generating points. For each point, let $\boldsymbol{q}_i$ be its ideal coordinate, and $\boldsymbol{x}_i$ its current coordinate. They are related by

$$\boldsymbol{x}_i = \boldsymbol{q}_i + \epsilon\,\boldsymbol{d}_i, \qquad (64)$$

where $\boldsymbol{d}_i$ is the displacement of site i from its ideal coordinate, and ϵ is a fiducial dimensionless time variable, with $\epsilon = 1$ corresponding to the current situation. Our goal is to estimate $\boldsymbol{d}_i$, such that by applying a coordinate shift $-\boldsymbol{d}_i$ to all the points, we can move the mesh close to the ideal configuration.

We shall now assume that the displacements can be obtained as gradient of a scalar field Ψ,

$$\boldsymbol{d} = -\boldsymbol{\nabla}\Psi. \qquad (65)$$

Furthermore, since we only consider linear order, we can write the evolution of the number density field $n_\epsilon(\boldsymbol{x})$ along the particle trajectories as

$$n_\epsilon(\boldsymbol{x} + \epsilon\boldsymbol{d}) = \epsilon\, n(\boldsymbol{x} + \boldsymbol{d}) + (1 - \epsilon)\, n_0(\boldsymbol{x}). \qquad (66)$$

The 'velocities' of each point in this transformation are given by $\boldsymbol{v}_i = \mathrm{d}\boldsymbol{x}_i/\mathrm{d}\epsilon = \boldsymbol{d}_i$. Invoking the Lagrangian continuity equation for the motion of the points,

$$\frac{\mathrm{d}n}{\mathrm{d}\epsilon} + n\boldsymbol{\nabla}\cdot\boldsymbol{v} = 0, \qquad (67)$$

and evaluating it at $\epsilon = 0$, we obtain the Poisson-like equation

$$\nabla^2\Psi = \frac{n(\boldsymbol{x} + \boldsymbol{d})}{n_0(\boldsymbol{x})} - 1 \simeq \frac{n(\boldsymbol{x})}{n_0(\boldsymbol{x})} - 1, \qquad (68)$$

where in the last step we approximated to linear order

$n(\boldsymbol{x} + \boldsymbol{d}) \simeq n(\boldsymbol{x})$. What remains to be done is to specify the desired density of mesh-generating points n_0 for the ideal configuration of the Voronoi cells. Here we use the following ansatz that can deal with quite general situations, including cases where there is empty space. We would like that the quantity

$$K_i \equiv \frac{m_i}{\tilde{m}} + \frac{V_i}{\tilde{V}} \qquad (69)$$

is equal to a constant value $\tilde{K}$ for all cells, i.e. $K_i = \tilde{K}$. Here $\tilde{m}$ is a prescribed constant which effectively sets the desired (maximum) mass per cell, and $\tilde{V}$ is a chosen value that determines the desired maximum volume per cell, while m_i and V_i are the actual mass and volume of the cell i. For the ideal mesh, the mass and volume of a cell are given by $m_i = \rho(\boldsymbol{q}_i)/n_0(\boldsymbol{q}_i)$ and $V_i = 1/n_0(\boldsymbol{q}_i)$, respectively. We can hence write

$$n_0(\boldsymbol{x}) = \frac{1}{\tilde{K}}\left(\frac{\rho(\boldsymbol{x})}{\tilde{m}} + \frac{1}{\tilde{V}}\right). \qquad (70)$$

Note that the density field itself is assumed to be stationary here; only the sampling by the mesh points changes. This leads finally to the following Poisson-equation to obtain the mesh-displacement vectors

$$\nabla^2\Psi = \frac{\tilde{K}\,n(\boldsymbol{x})}{\rho(\boldsymbol{x})/\tilde{m} + 1/\tilde{V}} - 1. \qquad (71)$$

This can be solved in the same way as we solve for the gravitational field, either with particle-mesh (PM) methods in Fourier-space, or in real-space via a tree, or by a combination of the two (TreePM method). Finally, we estimate the displacement of a point from its ideal position by evaluation $\boldsymbol{d} = -\boldsymbol{\nabla}\Psi$ at its current coordinate instead of the unknown ideal coordinate, which is again accurate to leading linear order.
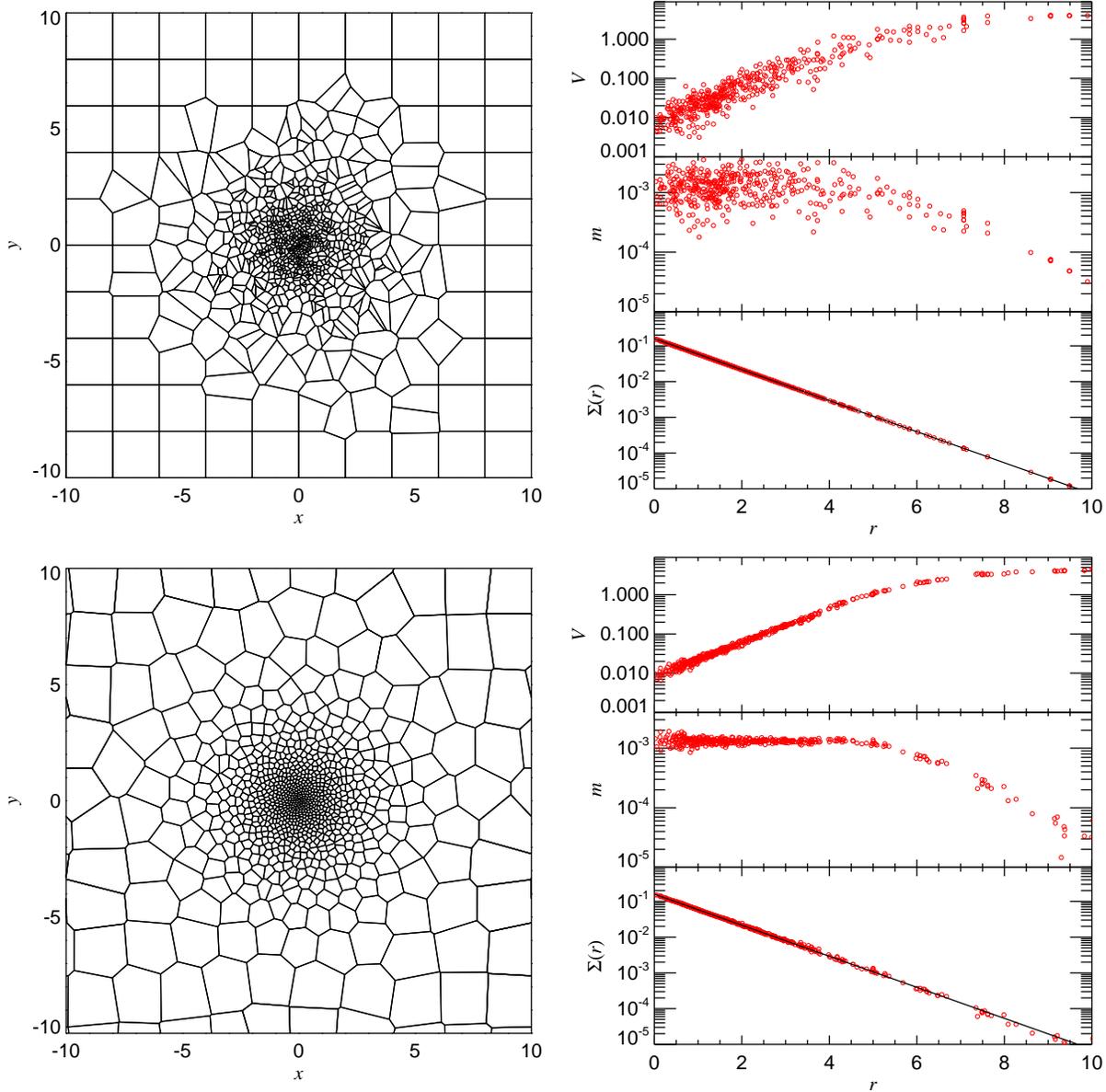
Figure 14. Mesh regularization of the initial conditions of an exponential disk. We here randomly distributed 750 particles with an exponential surface profile of scalelength $R_0 = 1.0$. To represent the 'vacuum' outside the disk, an additional Cartesian grid of 10×10 particles was placed into the simulation domain, which is a periodic box of 20 length units on a side. The resulting Voronoi mesh is shown in the top panel. While it has the right density field, the mass per cell (and hence the cell volumes) shows substantial scatter, as seen in the top right panel. However, after the mesh regularization has been applied, a much better mesh results, as seen in the bottom panels. While the surface mass density profile has remained the same, there is now little local scatter in the mass and volume per cell. Inside the disk, constant mass per cell is reached, while far outside, a constant volume per cell is obtained, with a smooth transition between the two regimes.

We will typically assume periodic boundary conditions for the mesh regularization. The value of $\tilde{K}$ should then be set such that the source term on the right hand-side of equation (71) integrates to zero for the current particle distribution; this is a prerequisite that the Poisson equation actually has a well-defined solution for an infinite periodic space. This means that we should set

$$\tilde{K} = \frac{V_{\text{tot}}}{\sum_i \left(\rho_i / \tilde{m} + 1/\tilde{V} \right)^{-1}}, \tag{72}$$

where V_{tot} is the total volume of the simulation domain. The -1 on the right hand side of equation (71) then eliminates the constant term in Fourier space. This is similar to the treatment of self-gravity in periodic spaces, where the mean density needs to be subtracted from the density field in order to obtain a finite solution of the Poisson equation.

Solving for the displacement field is equivalent to calculating the gravitational accelerations for a particle distribution with 'masses' given by $\tilde{K}/(\rho_i/\tilde{m} + 1/\tilde{V})$. We use the TreePM formalism for this, which has the advantage of be-

ing free of any restrictions on dynamic range while at the same time being quite fast. Once we have obtained the displacement vectors $\boldsymbol{d}_i$ for all particles, we add a corrective velocity to the mesh motion as follows:

$$\boldsymbol{w}_i' = \boldsymbol{w}_i - \kappa \frac{\boldsymbol{d}_i}{\Delta t}. \tag{73}$$

We usually set $\kappa = 0.5$, such that the estimated displacement from the ideal position is cut in half in each timestep. If needed, κ is reduced for the current step such that the maximum displacement of a point does not exceed half its cell size, which is needed for stability reasons. As this scheme is quite effective in maintaining an ideal mesh at all times, the size of the prefactor κ does not really matter much in practice.

We note that the above approach essentially corresponds to an 'inverse Zeldovich approximation', as it is used for example by the GADGET-2 code (Springel, 2005) to produce a gravitational 'glass' (White, 1996) of constant density, except that we generalized the approach to allow construction of generalized glasses for variable density fields that are constrained by the freely adjustable constants $\tilde{m}$ and $\tilde{V}$. We note that this method may also be useful to construct 'quiet starts' for SPH calculations that need to initialize astrophysical objects with a prescribed density structure, such as stars in simulations of stellar collisions. The methods most commonly used for this purpose at the moment rely on settling the particle distribution into equilibrium with the help of artificial friction or pressure forces (e.g. Goodman & Hernquist, 1991). We also remark that both schemes for mesh-regularization discussed above obey the property of Galilean-invariance of the moving-mesh code. This is because the primary mesh motion is still given by equation (31); any Galilean boost would simply be absorbed into it, while the mesh-correction velocities would remain unaffected.

4.3 Constructing suitable initial conditions

The above discussion about mesh regularity also prompts the question of how suitable initial conditions for a prescribed initial density field can be constructed. For many hydrodynamical test problems, constant density fields are needed that can simply be realized with Cartesian grids. This is also a possible choice for cosmological initial conditions, where Cartesian grids may be used for the unperturbed initial conditions. However, sometimes one would like to start a simulation with a non-trivial density distribution for the gas, for example in the form of a gaseous disk with a prescribed surface density profile, or in the form of a spherically symmetric gas cloud that approximates the gas distribution in a cluster of galaxies.

One popular approach to realize such general density distributions in SPH lies in randomly sampling the density field, for example with the rejection method (Press et al., 1992). This effectively produces a Poisson sampling of the underlying density field. While such a particle distribution can be used as initial conditions for the mesh-generation points, the quite irregular mesh this corresponds to represents a significant disadvantage. For example, in the top left panel of Fig. 14, we show the Voronoi mesh resulting from a random realization of a gaseous disk with an exponential

gas surface density profile. In addition to 750 particles used for the primary disk distribution, a coarse Cartesian grid with 10^2 points has been used here to fill the volume with cells that do not exceed a certain maximum volume. Due to the random sampling, the resulting mesh is characterized by cells with significant scatter in their volume at any given radius, as seen in the top panels of Fig. 14, and since the desired density profile has been prescribed, this is reflected in an equally large scatter in the mass per cell.

It is of course nevertheless possible to start a simulation with such a Poisson distribution and then to let the simulation code improve the mesh with time. However, if a more quiet start is desired, one can also first relax the initial mesh with the methods described above, except that the gas distribution is kept *fixed in space* by solving the advection equation for the moving mesh, instead of the Euler equation. For the advection equation, we use a simple second-order accurate upwind scheme to determine the fluxes at all cell faces.

An example for the result of such a relaxation is shown in the two bottom panels of Fig. 14. The panel on the left shows the Voronoi mesh, and the panel on the bottom right the radial profiles of mass and volume of each cell, as well as the surface density profile. Evidently, the relaxed mesh is much more regular and features relatively 'roundish' cells with low aspect ratios. Also, at any given radius, there is little scatter in the mean mass and mean volume of the cells. In fact, their radial variation follows the imposed constraint of constant $m_i/\tilde{m} + V_i/\tilde{V}$ very well. This produces a situation where in the inner parts of the disk the mass per cell is constant, while in the low density outer regions, the volume of the cells is kept fixed, with a smooth transition in between. This behaviour is particular useful for structures embedded in nearly or completely empty space, for example for simulations of isolated or colliding galaxies.

5 SELF-GRAVITY

Outside of astrophysics, self-gravity of gases plays hardly any role in computational fluid dynamics. However, gravitational forces are the primary driver of cosmological structure formation. This fundamental importance of gravity adds a significant complication to hydrodynamic codes. In fact, in cosmology there is arguably little value in calculating the hydrodynamics highly accurately when gravity is not treated with comparable accuracy.

There are some indications that the specific challenges posed by an accurate treatment of self-gravity have been underestimated when traditional Eulerian approaches have been employed in cosmology. This is suggested by recent comparisons of P^3M/Tree/TreePM methods and adaptive mesh refinement (AMR) codes where both are applied in pure gravity mode to the clustering of collisionless dark matter. Both in O'Shea et al. (2005) and Heitmann et al. (2008) it was found that state-of-the-art AMR codes like ENZO and FLASH have significant problems in accurately recovering the low-mass end of the mass function of dark matter halos. They are only able to match the results of high-accuracy N-body codes once much finer base meshes and stricter refinement criteria are used than are normally employed with these codes. They are then no longer competitive with al-

ternative approaches in cosmological structure formation in terms of calculational efficiency and memory consumption (O'Shea et al., 2005). While these results have been found in comparison studies that only tested the AMR gravity solver for a collisionless fluid, it is clearly worrying that similarly poor behaviour is likely also to affect calculations of self-gravity in hydrodynamical applications.

The problem seems to be that the adaptive refinement strategy, as presently applied in the gravity solvers of some of the cosmological AMR codes, does not work particularly well for the gravitational instability of dark matter, where structures may grow everywhere from very small seed perturbations. Since the placement or removal of refinements corresponds to discrete and *discontinuous* changes in local resolution, the growth of small perturbations can be delayed if a refinement is placed 'too late' onto an emerging halo. The effectively Lagrangian behaviour of tree codes fares better in this respect. Here, the spatially homogeneous high force resolution allows tree codes to be formulated such that they observe the Hamiltonian structure of the collisionless dynamics of dark matter. This structure is broken each time the AMR mesh hierarchy is modified, because this changes the effective gravitational softening associated with the mesh, and modifies the potential energy stored in the density field. As we will see, in the moving mesh approach such discontinuous changes in the Hamiltonian structure of gravitational dynamics can be avoided.

An attractive feature of our new Lagrangian hydrodynamical scheme lies in the possibility of combining it easily with a particle-based approach to calculate the gravitational field, in the form of the familiar high-accuracy N-body solvers for collisionless dynamics, for example Tree or TreePM schemes. The simplest approach for this is to treat the mass of each cell as being concentrated in the centre of the cell, and then to calculate the gravitational force on a cell as the suitably gravitationally softened N-body force of the resulting point set. The hierarchical multipole expansion used in tree codes, carried out to monopole or quadrupole order, provides an efficient way to compute these forces. And thanks to the tree-based approach, the gravitational resolution then automatically and *continuously* adjusts in a collapsing structure, and the spatial resolution of self-gravity in the gas is always matched accurately to that of the hydrodynamics (see also Bate & Burkert, 1997). We shall employ this approach in this work. The specific N-body algorithms we adopt for calculating the gravitational forces are those of an updated version of the code GADGET-2 (Springel, 2005).

5.1   The Euler equations with self-gravity

If a gravitational field is present, the Euler equations (8) are modified by source terms for momentum and energy, which take the form

$$\frac{\partial \boldsymbol{U}}{\partial t} + \boldsymbol{\nabla} \cdot \boldsymbol{F} = \begin{pmatrix} 0 \\ -\rho \boldsymbol{\nabla} \Phi \\ -\rho \boldsymbol{v} \boldsymbol{\nabla} \Phi \end{pmatrix}. \tag{74}$$

The gravitational potential Φ may be externally specified, or it describes the self-gravity of the gas as a solution of Poisson's equation,

$$\boldsymbol{\nabla}^2 \Phi = 4\pi G \rho. \tag{75}$$

In the former case, the total energy $E_{\text{tot}} = \int (\rho e + \rho \phi) \mathrm{d}V$ stays constant if the potential is static. In the more relevant case of self-gravity, the total energy of the system is given by

$$E_{\text{tot}} = \int \left(\rho e + \frac{1}{2} \rho \Phi \right) \mathrm{d}V, \tag{76}$$

and is conserved in the dynamics, i.e.

$$\frac{\mathrm{d}E_{\text{tot}}}{\mathrm{d}t} = 0. \tag{77}$$

Without gravity, the finite volume formulation for hydrodynamics introduced earlier ensures conservation of the sum of thermal and kinetic energy to machine precision. Since the thermal energy in this approach is actually defined as the difference between the total energy and kinetic energy of a cell, it is in principle highly desirable to also obtain a discretized formulation of the dynamics in the self-gravitating case where the conservation of energy is manifest. Furthermore, it would be convenient if the gravitational source term could be incorporated into the time integration such that there is no need to explicitly include gravity in the Riemann solver (this can be done approximately, however, see for example the PPM scheme of Colella & Woodward, 1984).

In the following, we first review a standard approach to include self-gravity in finite volume codes, which however is not explicitly energy-conserving. In fact, we will show that the resulting errors can be quite substantial for certain types of problems. We then briefly discuss an attempt to improve on this by restoring manifest conservation of the total energy, based on including the gravitational self-energy in the total energy variable that is evolved for each cell. Unfortunately, it turns out that this approach is numerically problematic since it can lead to unphysical changes of the local thermal energy. We therefore ultimately adopt a different solution that corrects for the large errors that can appear in the 'standard' approach. While not manifestly conservative, we find that, in practice, the total energy is conserved quite accurately in this approach. Since monitoring the accuracy of total energy conservation can then also serve as a useful check of the quality of the integration, we consider this as a good compromise. Finally, we discuss our treatment of locally adaptive, time-dependent gravitational softening, and how this is accounted for in the dynamics.

5.2   A standard approach to include self-gravity

Arguably the simplest method to include self-gravity lies in an operator-splitting approach, where one alternatingly evolves the system under the homogeneous Euler equations and the gravitational source terms. However, such fractional step methods are often inadequate for handling the gravitational source terms, especially in situations with approximate hydrostatic equilibrium (Müller & Steinmetz, 1995; LeVeque, 1998; Zingale et al., 2002). We will therefore not consider this method here.

Instead, we consider the method suggested by Müller & Steinmetz (1995), which is employed in similar form in many current finite volume cosmological codes (e.g. Truelove et al., 1998). Since the gravitational energy is nonlocal, an explicit conservation of total energy in the discretizations

of equations (74) and (75) cannot easily be obtained with an extension of the standard flux-based formalism of finite volume methods. We may therefore give up the property of manifest energy conservation and instead couple the gravitational field to the Euler equations in a way that resembles the fractional-step approach, except that gravity is also properly included in the half-step prediction of the hydrodynamical step.

We begin by noting that, when the Euler equations are expressed in primitive variable formulation,

$$\frac{\partial \boldsymbol{W}}{\partial t} + \begin{pmatrix} \boldsymbol{v} & \rho & 0 \\ 0 & \boldsymbol{v} & 1/\rho \\ 0 & \gamma P & \boldsymbol{v} \end{pmatrix} \frac{\partial \boldsymbol{W}}{\partial \boldsymbol{r}} = \begin{pmatrix} 0 \\ -\boldsymbol{\nabla}\Phi \\ 0 \end{pmatrix}, \qquad (78)$$

where $\boldsymbol{W} = (\rho, \boldsymbol{v}, P)$, the gravitational source term couples only to the momentum equation. Hence, to first order in time, the gravitational field does not change the pressure or density of a fluid, only the velocity is altered. We can therefore account for the gravitational field in the hydrodynamic flux calculation if we augment the half-step prediction of the velocities with the gravitational acceleration according to

$$\tilde{\boldsymbol{v}}_i^{(n+1/2)} = \boldsymbol{v}_i^{(n+1/2)} - \frac{\Delta t}{2}\boldsymbol{\nabla}_i\Phi^{(n)}, \qquad (79)$$

where the potential $\Phi^{(n)}$ is calculated at the beginning of the step. Applying the ordinary reconstruction and Riemann solver techniques discussed earlier, we can then obtain time-centred flux estimates that solve the homogeneous part of the Euler equations. To add the gravitational source term into the final time-advance, we then proceed as follows. We first use the estimated mass flux to update the mass contained in each cell,

$$m_i^{(n+1)} = m_i^{(n)} - \Delta t \sum_j A_{ij} F_m^{ij}, \qquad (80)$$

which exploits the fact that the gravitational field does not appear in the mass equation of the conservative form of the Euler equations. With the new masses in hand, we can calculate the gravitational forces at the end of the timestep, $\boldsymbol{\nabla}_i\Phi^{(n+1)}$. This allows an update of the momentum of each cell, according to

$$\begin{aligned} \boldsymbol{p}_i^{(n+1)} &= \boldsymbol{p}_i^{(n)} - \Delta t \sum_j A_{ij} \boldsymbol{F}_{\boldsymbol{p}}^{ij} \\ &\quad -\frac{\Delta t}{2}\left[m_i^{(n)}\boldsymbol{\nabla}_i\Phi^{(n)} + m_i^{(n+1)}\boldsymbol{\nabla}_i\Phi^{(n+1)} \right], \end{aligned} \qquad (81)$$

where $\boldsymbol{F}_{\boldsymbol{p}}$ is the hydrodynamical momentum flux. Note that this step also determines the new velocities at the end of the step. We can use them to finally obtain a second-order accurate update of the energies of each cell,

$$\begin{aligned} \boldsymbol{E}_i^{(n+1)} &= \boldsymbol{E}_i^{(n)} - \Delta t \sum_j A_{ij} F_E^{ij} \\ &\quad -\frac{\Delta t}{2}\left[m_i^{(n)}\boldsymbol{v}_i^{(n)}\boldsymbol{\nabla}_i\Phi^{(n)} + m_i^{(n+1)}\boldsymbol{v}_i^{(n+1)}\boldsymbol{\nabla}_i\Phi^{(n+1)} \right]. \end{aligned} \qquad (82)$$

Here, the term in square brackets is the gravitational work term, while the flux term involving F_E stems from the homogeneous part of the Euler equations.

The above scheme does not explicitly conserve total energy, but it still conserves total momentum and mass. Violations of energy conservation can arise because the gravitational work term, which is estimated effectively with cell-centred fluxes, may not precisely balance the *actual* energy extracted from the gravitational field, which is determined by the mass fluxes obtained with the Riemann solver around a cell's boundary. We have found that this subtle difference can sometimes lead to substantial inaccuracies in total energy conservation, especially in collapse problems that involve strong shocks and a conversion of large amounts of gravitational energy into heat energy. For example, "Evrard's collapse problem", to be discussed in Section 9.1, shows large errors of this kind, especially when the spatial resolution is relatively poor. Note that in this case the violation of the total energy conservation is first order in time, i.e. it does not go away with very fine time-stepping and instead stays constant at a finite (large) size even in the limit of highly accurate time integration. It is therefore desirable to obtain a more accurate discretization of the energy equation when a gravitational field is present.

5.3 An explicitly conservative formulation to include self-gravity

One idea for a more accurate discretization of the conservative Euler equations in the presence of gravity is based on rewriting the standard form of the energy equation,

$$\frac{\partial}{\partial t}(\rho e) + \boldsymbol{\nabla}\left[(\rho e + P)\boldsymbol{v}\right] = -\rho\boldsymbol{v}\boldsymbol{\nabla}\Phi, \qquad (83)$$

with the help of the continuity equation as

$$\begin{aligned} \frac{\partial}{\partial t}\left(\rho e + \frac{1}{2}\rho\Phi\right) + \boldsymbol{\nabla}\left[\left(\rho e + \frac{1}{2}\rho\Phi + P\right)\boldsymbol{v}\right] = \\ \frac{1}{2}\rho\frac{\partial\Phi}{\partial t} - \frac{1}{2}\rho\boldsymbol{v}\boldsymbol{\nabla}\Phi. \end{aligned} \qquad (84)$$

This suggests redefining the total energy of an individual cell as

$$E_i = \int_{V_i}\left(\rho e + \frac{1}{2}\rho\Phi\right)\mathrm{d}V, \qquad (85)$$

such that the total energy of the system simply becomes the sum of the E_i of all cells. If we suitably modify the energy flux function in the hydrodynamical finite volume scheme, the left hand side of equation (84), which has the form of a conservation law, can be easily solved such that the *total* energy stays constant. If we can also find an explicitly conservative discretization of the modified source term on the right-hand side of equation (84), we would obtain a scheme that manifestly conserves the total energy.

This can, in fact, be achieved. We can write the right-hand side of equation (84) as

$$\begin{aligned} \frac{1}{2}\rho\frac{\partial\Phi}{\partial t} - \frac{1}{2}\rho\boldsymbol{v}\boldsymbol{\nabla}\Phi &= \\ G\int\rho(\boldsymbol{x})\rho(\boldsymbol{x}')&\frac{\boldsymbol{v}(\boldsymbol{x}) + \boldsymbol{v}(\boldsymbol{x}')}{2}\boldsymbol{\nabla}_{\boldsymbol{x}}\frac{1}{|\boldsymbol{x} - \boldsymbol{x}'|}\mathrm{d}^3\boldsymbol{x}'. \end{aligned} \qquad (86)$$

If we decompose the $\boldsymbol{x}'$-integration into a sum over integrals over all cells, and integrate the full energy equation over $\boldsymbol{x}$ for a cell i, we obtain the discretized form

$$\frac{\mathrm{d}E_i}{\mathrm{d}t} + \sum_k \boldsymbol{A}_{ik}F_{ik}^{(E)} = \sum_j \frac{\boldsymbol{v}_i + \boldsymbol{v}_j}{2}\boldsymbol{f}_{ij} \qquad (87)$$

for the energy equation, where $\boldsymbol{f}_{ij}$ is the gravitational force between cells i and j. We see that the term on the right hand

side effectively symmetrizes the gravitational work term the two cells exert onto each other. The sum over j extends over all cells, but both relevant terms, the total force $\sum_j \boldsymbol{f}_{ij}$ and the total work term $\sum_j \boldsymbol{v}_j \boldsymbol{f}_{ij}$ can be accurately and efficiently calculated with a tree algorithm. The sum over k in equation (87) accumulates the energy fluxes

$$F_{ik}^{(E)} = \rho_{ik} \left(e_{ik} + \frac{\Phi_{ik}}{2} \right) (\boldsymbol{v}_{ik} - \boldsymbol{w}_{ik}) + P_{ik} \boldsymbol{v}_{ik} \qquad (88)$$

from the neighbouring cells of cell i, where the (ρ_{ik}, e_{ik}, $\boldsymbol{v}_{ik} - \boldsymbol{w}_{ik}$, P_{ik}) are determined by the Riemann problem between cells i and k, and the potential Φ_{ik} on the face between two cells can be defined as the arithmetic mean $\Phi_{ik} = (\Phi_i + \Phi_k)/2$ of the potentials at the corresponding mesh-generating points of the cells. It is not difficult to define a time integration scheme for equation (87) that preserves its conservative character in the discretized form, such that at least formally a finite volume scheme results that accurately conserves up to machine precision the total energy, momentum and mass in the presence of a gravitational field.

However, the above approach shows severe shortcomings in practice. In particular, the fact that the temperature of the gas is effectively defined by subtracting the kinetic energy *and* the potential energy from the total energy associated with a fluid element causes trouble. This can give rise to spurious local changes in the temperature of the gas due to the presence of a gravitational field, even though the Euler equations in primitive variable form show that there should be no first order change in the temperature due to a gravitational field. We have found that in some cases this may even drive the temperature to unphysical negative values. Secondly, in this approach the temperature field couples to discreteness noise present in the gravitational field, which considerably reduces the accuracy of the hydrodynamical calculations. In combination, these defects are severe enough that the 'total energy approach' described in this subsection appears not to be a viable practical solution for implementing self-gravity in the moving-mesh approach. We therefore refrain from using it in our practical applications.

One exception is the case where gravity is simply described by an external static gravitational potential Φ. We can then express the conservation of total energy as

$$\frac{\partial}{\partial t} \left(\rho e + \rho \Phi \right) + \boldsymbol{\nabla} \left[(\rho e + \rho \Phi + P) \, \boldsymbol{v} \right] = 0, \qquad (89)$$

which suggests that we include the gravitational energy in the definition of the total energy of a cell. The thermal energy can then be defined by subtracting both the kinetic energy and the potential energy from the total energy. We also need to augment the energy flux term for a cell interface with an additional gravitational energy flux, with the result that the total energy is exactly conserved. The inclusion of gravity into the dynamics then proceeds like in equations (80), (81) and (82), except that in equation (82) the explicit gravitational work term (in square brackets) is omitted as it is already accounted for by the energy flux.

5.4   An improved coupling of self-gravity to the Euler equations

In the following, we discuss a method that tries to improve the discretization of the energy equation used in the 'stan-

dard approach' discussed above in Section 5.2. Recall that the gravitational work exerted on a cell over a timestep Δt is given by

$$\Delta E_i^{\rm grav} = - \int \mathrm{d}t \int_{V_i} \mathrm{d}V \rho \, \boldsymbol{v} \boldsymbol{\nabla} \Phi, \qquad (90)$$

integrated over the moving volume of a cell. We may also rewrite this integral as

$$\Delta E_i^{\rm grav} = - \int \mathrm{d}m \int \mathrm{d}\boldsymbol{s} \boldsymbol{\nabla} \Phi. \qquad (91)$$

where $\mathrm{d}\boldsymbol{s}$ is the displacement of each individual mass element. This highlights that the key to accurate energy conservation in case of self-gravity is to correctly account for the *actual* mass motions that happen in the system. The problem with equation (82) is that this is not guaranteed explicitly since it estimates the mass motion with a cell-centred flux, but the mass fluxes actually used are calculated at the surfaces of the cells, and may sometimes be quite different.

We suggest another discretization of equation (90) that improves on this. First, we introduce the velocity vector $\boldsymbol{w}_i$ of the cell's motion, which splits the integral into two parts, one describing the motion of the cell itself (with all of its mass), and the other accounting for the motion of mass elements that are actually exchanged between two adjacent cells, viz.

$$\Delta E_i^{\rm grav} = -\Delta t \, m_i \boldsymbol{w}_i \boldsymbol{\nabla} \Phi_i - \Delta t \int \rho_i (\boldsymbol{v} - \boldsymbol{w}_i) \boldsymbol{\nabla} \Phi_i \, \mathrm{d}V. \quad (92)$$

Instead of approximating the volume integral of the second part with a cell-centred flux, we transform it into a surface integral. Neglecting spatial variations in the density, velocity, and force fields for the moment, we can write $\boldsymbol{v} - \boldsymbol{w}_i = \boldsymbol{\nabla}[(\boldsymbol{r} - \boldsymbol{r}_i)(\boldsymbol{v} - \boldsymbol{w}_i)]$ and apply the Green-Gauss theorem. This yields

$$\begin{aligned} \Delta E_i^{\rm grav} &= -\Delta t \, m_i \boldsymbol{w}_i \boldsymbol{\nabla} \Phi_i \qquad\qquad\qquad (93) \\ &\quad - \frac{\Delta t}{2} \sum_j \rho_{ij} [(\boldsymbol{v}_{ij} - \boldsymbol{w}_i) \boldsymbol{r}_{ij}] [\boldsymbol{\nabla} \Phi_i \boldsymbol{r}_{ij}/r_{ij}] A_{ij}, \end{aligned}$$

where the sum is now over all faces of area A_{ij} of a cell, and, as usual, $\boldsymbol{r}_{ij} = \boldsymbol{r}_i - \boldsymbol{r}_j$ is the displacement vector between the neighbouring mesh-generating points. We have also replaced the values of density and velocity on the surface with those determined by the Riemann solver. In fact, the term $\Delta t \rho_{ij} (\boldsymbol{v}_{ij} - \boldsymbol{w}_i) \boldsymbol{r}_{ij} A_{ij}/r_{ij}$ can be recognized as the integrated mass flux $\Delta m_{ij} = \Delta t A_{ij} F_m^{ij}$ exchanged between two cells i and j, yielding

$$\Delta E_i^{\rm grav} = -\Delta t \, m_i \boldsymbol{w}_i \boldsymbol{\nabla} \Phi_i - \frac{1}{2} \sum_j \Delta m_{ij} \boldsymbol{r}_{ij} \boldsymbol{\nabla} \Phi_i. \qquad (94)$$

An even more instructive form of this equation is obtained with the replacement

$$\boldsymbol{r}_{ij} \boldsymbol{\nabla} \Phi_i \simeq \Phi_i - \Phi_j \qquad (95)$$

which gives

$$\Delta E_i^{\rm grav} = -\Delta t \, m_i \boldsymbol{w}_i \boldsymbol{\nabla} \Phi_i - \frac{1}{2} \sum_j \Delta m_{ij} (\Phi_i - \Phi_j). \qquad (96)$$

If we define the total gravitational energy of the discretized system as

$$E_{\text{pot}} = \frac{1}{2} \sum_{ij} G\, m_i\, m_j\, \phi(r_{ij}) = \frac{1}{2} \sum_i m_i \Phi_i \qquad (97)$$

and the potential as

$$\Phi_i = \sum_j G\, m_j\, \phi(r_{ij}), \qquad (98)$$

where ϕ_{ij} describes the gravitational interaction kernel between two cells, then it is easy to see that equation (96) describes the gravitational energy change *exactly* to linear order in time. This is a significant improvement compared with schemes based on cell-centred flux for the gravitational work estimate. The above can hence replace the energy update of equation (82) with a more accurate version that ensures conservation of the total energy in self-gravitating systems.

In practice, we typically use the version (94) based on the gravitational forces, instead of equation (96) based on the potential. In order to render the time integration of the energy equation second-order accurate, we need to replace the gravitational forces (or potentials) with averages between the beginning and end of the timesteps, which can be done as in section 5.2. We note that this method is also applicable in ordinary Eulerian codes, where $\Delta \boldsymbol{w}_i = 0$, not just in the moving-mesh approach developed in this paper. However, the method may also cause drifts of the temperature of the gas in certain situations, and is hence not completely free of the problems that were mentioned earlier.

5.5 Gravitational softening

To calculate gravitational potentials and forces for our unstructured hydrodynamical mesh, we represent each cell as a mass point with an appropriate gravitational softening, and employ techniques that are commonly used in N-body algorithms. In principle, the gravitational field of a single Voronoi cell could be adopted as the field of a polyhedron of constant density, with the cell's shape and its total mass. However, this would make an exact calculation of the field unwieldy and unnecessarily complicated. As we anyway run out of gravitational resolution on the scale of the mesh cells, the precise shape of a cell should be unimportant, provided we can ensure that the generated field is sufficiently smooth and free of anisotropies due to the mesh geometry. For simplicity, we therefore represent the potential of each gaseous cell as that of a top-hat sphere of constant density and radius h. In order to improve the smoothness of the potential in light of the varying geometries of individual cells, we typically choose the volume of this top-hat sphere to be slightly larger than the cell volume itself. In practice, we relate h to the volume V of a cell as $h = f_h (3V/4\pi)^{1/3}$, where we choose $f_h \sim 1.0 - 1.5$. We note that for well-behaved meshes a softening of the force-law is not strictly necessary because the mesh-generating points are then always sufficiently distant from each other. However, a gravitational softening is always required if a collisionless particle component is present as well, and it allows a consistent definition of the gravitational binding energy of the gas.

The gravitational potential kernel of a cell of volume V is taken to be

$$\phi(r, h) = -\frac{1}{r} \begin{cases} \frac{r}{2h}\left[3 - \left(\frac{r}{h}\right)^2\right] & \text{for } r \le h, \\ 1 & \text{for } r > h, \end{cases} \qquad (99)$$

as a function of distance r. We then define the total gravitational self-energy of the system of Voronoi cells as

$$E_{\text{pot}} = \frac{1}{2} \sum_{ij} G\, m_i\, m_j\, \phi(r_{ij}, h_j). \qquad (100)$$

Ignoring mass exchanges between cells for the moment, this implies that the gravitational acceleration of a cell is given by

$$
\begin{aligned}
m_i\, \boldsymbol{a}_i^{\text{grav}} &= -\frac{\partial E_{\text{pot}}}{\partial \boldsymbol{r}_i} \\
&= -\sum_j G m_i m_j \frac{\boldsymbol{r}_{ij}}{r_{ij}} \frac{[\phi'(r_{ij}, h_i) + \phi'(r_{ij}, h_j)]}{2} \\
&\quad - \frac{1}{2} \sum_{jk} G m_j m_k \frac{\partial \phi(r_{jk}, h_j)}{\partial h} \frac{\partial h_j}{\partial \boldsymbol{r}_i},
\end{aligned} \qquad (101)
$$

where $\phi'(r, h) = \partial\phi/\partial r$ and $\boldsymbol{r}_{ij} = \boldsymbol{r}_i - \boldsymbol{r}_j$. The interaction between cells of different softening lengths is hence symmetrized by averaging the forces, as opposed to, for example, by averaging the softening lengths. This is analogues to the formalism employed in Hernquist & Katz (1989). By defining the potential energy of equation (100) slightly differently, in terms of an interaction potential with a symmetrized softening length h_{ij}, one can however also arrive at a scheme where the softening lengths are averaged, but then the correction force derived below is less convenient to calculate.

The last term in equation (101) describes an additional force component which stems from changes of the gravitational softening lengths. It has to be included to make the system properly conservative when spatially adaptive gravitational softening lengths are used (Price & Monaghan, 2007) that are allowed to vary in time, which is our default approach to treat self-gravity in the moving-mesh scheme. Since we tie the gravitational softening length to the volume of a Voronoi cell, we have

$$\frac{\partial h_j}{\partial \boldsymbol{r}_i} = \frac{\partial h_j}{\partial V_j} \frac{\partial V_j}{\partial \boldsymbol{r}_i} = \frac{h_j}{3V_j} \frac{\partial V_j}{\partial \boldsymbol{r}_i}. \qquad (102)$$

Defining the quantities

$$\eta_j \equiv \frac{1}{2} \sum_k G m_j m_k \frac{\partial \phi(r_{jk}, h_j)}{\partial h} \frac{h_j}{3V_j}, \qquad (103)$$

we can rewrite the last sum in equation (101) as

$$m_i\, \boldsymbol{a}_i^{\text{soft}} = -\sum_j \eta_j \frac{\partial V_j}{\partial \boldsymbol{r}_i}. \qquad (104)$$

Using equations (22) and (23) for the partial derivative of the Voronoi volume (see Serrano & Español, 2001), this can be more explicitly expressed as

$$m_i\, \boldsymbol{a}_i^{\text{soft}} = \sum_{j \ne i} (\eta_j - \eta_i)\, A_{ij} \left(\frac{\boldsymbol{c}_{ij}}{r_{ij}} - \frac{\boldsymbol{r}_{ij}}{2r_{ij}} \right), \qquad (105)$$

where the sum extends over all the Voronoi neighbours of a cell. Note that A_{ij}, $\boldsymbol{c}_{ij}$, and r_{ij} are invariant when i and j are exchanged, while $\boldsymbol{r}_{ij}$ changes sign. The term involving $\boldsymbol{c}_{ij}$ produces therefore an antisymmetric force between i and j, but the same is not obvious for the force from the $\boldsymbol{r}_{ij}$-term. However, according to the Gauss theorem we have
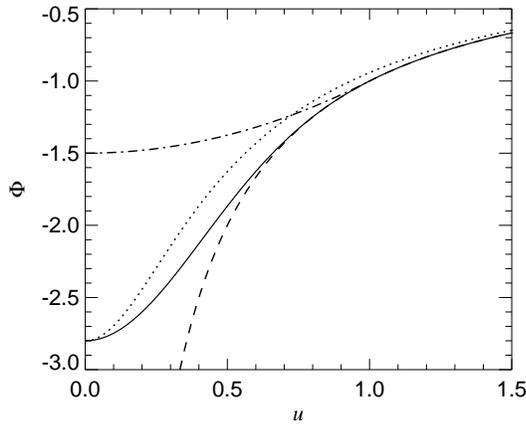
Figure 15. Softened gravitational potential for cells and particles. The solid line shows the spline-based softening we use for collisionless particles, while the dot-dashed line is the top-hat like softening of gaseous cells. Both potentials become equal to the Newtonian potential for $u \geq 1.0$. For comparison, we also show the Plummer softening with a dotted line. The dashed line is the Newtonian potential of a point mass.

$$\eta_i \sum_{j \neq i} A_{ij} \frac{\boldsymbol{r}_{ij}}{r_{ij}} = 0, \tag{106}$$

because the summation is just the surface integral of a constant function. If we subtract equation (106) from equation (105), we obtain

$$m_i \, \boldsymbol{a}_i^{\mathrm{soft}} = \sum_{j \neq i} A_{ij} \left[(\eta_j - \eta_i) \frac{\boldsymbol{c}_{ij}}{r_{ij}} - (\eta_j + \eta_i) \frac{\boldsymbol{r}_{ij}}{2 r_{ij}} \right], \tag{107}$$

where now the antisymmetry of the correction force between particles i and j is manifest.

To properly account for the changes in the gravitational energy when the softening lengths are varied, we hence need to calculate the quantities η_i given by Equation (103), which can be conveniently done alongside the tree walk used for the gravity calculation. With these values in hand, we can then calculate the correction force as a surface integral over the local Voronoi cell. Finally, the correction force is added to the ordinary gravitational force, and the resulting total force is used in equations (81) and (82), or alternatively in equations (96), replacing $-m\boldsymbol{\nabla}\Phi$ where appropriate.

For the dark matter particles, we employ a softening kernel with a different shape, the same one as used in the SPH-code GADGET, which corresponds to spreading the mass of a particle with the more centrally concentrated SPH kernel. This softening kernel is given by

$$\phi_{\mathrm{dm}}(r, h) = -\frac{G}{r} \begin{cases} \frac{14}{5}u - \frac{16}{3}u^3 + \frac{48}{5}u^5 \\ \quad -\frac{32}{5}u^6, & 0 \leq u < \frac{1}{2}, \\ -\frac{1}{15} + \frac{16}{5}u - \frac{32}{3}u^3 \\ \quad +16u^4 - \frac{48}{5}u^5 + \frac{32}{15}u^6, & \frac{1}{2} \leq u < 1, \\ 1, & u \geq 1. \end{cases} \tag{108}$$

where $u = r/h$. Often, we will quote the gravitational softening length for collisionless dark matter particles in terms of an 'equivalent' Plummer softening length ϵ, defined such that the potential at zero lag is $m\,\phi(0) = -Gm/\epsilon$. This implies $h = 2.8\epsilon$. We keep the softening lengths for dark matter

particles fixed, which ensures that the collisionless dynamics is conservative without the need for correction forces like the ones derived for the gaseous cells. Figure 15 illustrates the difference in shape between the 'particle' and the 'cell' kernels, for an equal choice of h. The gravitational softening we have chosen for dark matter particles results in a slower decline of the force within the softening length.

In our tree-based gravity calculation, we store for each tree node the maximum softening length h_{node} of all particles it represents, and we always open a node if its distance is smaller than $\max(h_i, h_{\mathrm{node}})$, where h_i is the softening of the particle under consideration. As a result, softened interactions only occur between particles, and not between nodes and particles.

Finally, a brief comment about our treatment of the gravitational self-energy of individual resolution elements. In our tree-based calculation of the potential, we always sum over all particles, hence the potential at the location of a particle contains a contribution from the particle itself. In the case of a dark matter particle of mass m and softening length $h = 2.8\epsilon$, this is $-Gm/\epsilon$. Because the dark matter particle masses are constant, there is then a finite gravitational binding energy left even if all particles are spread out to infinity. While unimportant for the dynamics itself, we prefer to eliminate this contribution by subtracting the self-potential $-Gm/\epsilon$ from the calculated potential of a collisionless particle. For gas particles (which really represent cells of a well-defined volume), the situation is different. As their mass and volume can change, the self-energy contribution of a gaseous cell is not constant and hence cannot simply be subtracted. This is also not necessary in this case. As the gas mass is spread out to infinity, its self-energy will automatically tend to zero, because then the cell volumes and smoothing radii tend to infinity as well.

6 REFINING OR DEREFINING CELLS

In ordinary Eulerian hydrodynamics, adaptive-mesh refinement techniques are very useful methods for dynamically concentrating the mesh resolution in regions where it is needed most, while smooth regions or parts of the flow that are not of interest can be derefined and modelled more coarsely. For applications with a large dynamic range in density and length scales (which is typical in cosmology), adaptive mesh refinement is, in fact, often a prerequisite in Eulerian methods in order to achieve the necessary resolution in the regions that are of most interest.

The Lagrangian moving-mesh methodology introduced in this paper, when combined with the techniques to steer the mesh-motion, removes much of the need for adaptive mesh refinement, especially in applications where quasi-Lagrangian refinement criteria are used, as is typical in cosmological structure formation calculations with AMR. In fact, we think that the Lagrangian moving-mesh approach with its automatic adjustment of resolution to the local clustering state is ideal for this type of application, and is arguably more natural than AMR.

One of AMR's particular strengths is however that the refinement criteria can be nearly arbitrary. This allows resolution to be gained not only where most of the mass goes, but where resolution is needed or desired most, according to
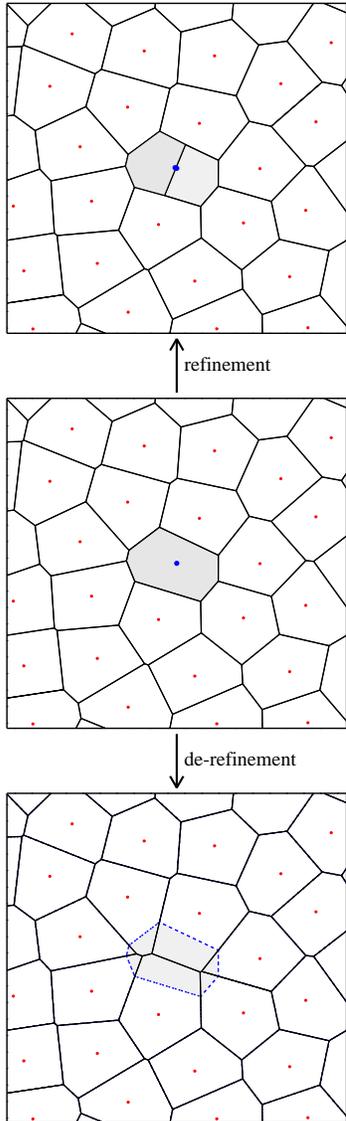
Figure 16. Example for the mesh refinement and derefinement operations. In the middle panel, a Voronoi cell is marked in grey. In a refinement operation, the cell is split into two cells, as shown in the top panel. If a coarsening of the mesh-resolution is desired, the cell may be eliminated from the mesh in the derefining operation shown in the bottom panel.

the problem at hand. For example, one might want to resolve low-density regions or locate shock fronts particularly well. Both can be achieved with AMR by an appropriate choice of the refinement criteria. If the same flexibility is desired for the unstructured Voronoi code discussed here, one needs to find ways to refine or derefine the local mesh resolution dynamically, a topic that we discuss briefly in this section.

In structured AMR, collections of cells can be hierarchically covered with patches of refined meshes. Since here the geometry of the cells is simple, it is easy to arrange the daughter meshes to exactly cover a certain set of cells in the parent mesh. This makes the operations of interpolation and prolongation straightforward. For our unstructured mesh, the situation is more complicated. In particular, it is

not straightforward to cover a contiguous set of cells with another set that is better resolved, simply because of the fact that the cell boundaries are defined as the edges of a Voronoi tessellation. Finding a new, larger set of points as a replacement for the points contained in some evacuated region such that the outer convex hull of the Voronoi cells of all original points remains unchanged is non-trivial in general. There is one exception, however: If we want to refine just a single cell, we can split a Voronoi cell into two halfs if we insert a new mesh-generating point at *almost exactly* the same location as the cell's original point. This will leave all surrounding Voronoi cells *unchanged.*

This forms the basic mechanism for mesh-refinement in our code. According to a criterion of choice, any given cell can be flagged for refinement. It is then split into two cells by introducing a further mesh-generating point, as illustrated in Figure 16. The conserved quantities of the original cell (mass, energy, momentum) are distributed among the two halfs in a conservative way, either simply by weighting with the relative fractions of the volumes occupied by the two new cells, or by using the estimated linear gradient for a conservative reconstruction combined with a volume integration. After the new point has been inserted, the mesh-regularization techniques then dynamically change the local mesh such that the two nearby points created by the cell split become well separated from each other over the course of a few timesteps. By introducing the new point in the direction of fluid gradients, one can furthermore optimize the direction for which the spatial resolution is gained.

Note that a fundamental difference in this refinement approach compared with the standard AMR method is that there is no hierarchy of multiple meshes that cover the same region of interest. Instead, there is always only a single mesh, albeit with spatially varying resolution. Refinement in our approach means the dynamic introduction of further cells to locally increase the resolution.

As we stressed above, the Lagrangian nature of the moving-mesh approach largely eliminates the need for 'mesh derefinements' in many practical applications. This is because the mesh follows the flow, which often means that the resolution automatically stays where it is needed, and in particular, advection alone does not generate a need for refinement or derefinement, in contrast to AMR codes. For example, if a galaxy that is highly resolved in its centre moves through space with large velocity, the moving mesh approach automatically follows the centre well, without any need to introduce mesh refinements. In Eulerian AMR on the other hand, refinements would have to be constantly introduced along the path of the galaxy's centre, and then removed again once it has passed by. Nevertheless, in certain applications, one may encounter situations also in the moving-mesh approach where one would like to dynamically reduce the spatial resolution in special regions of a mesh. However, the geometry of the Voronoi mesh imposes significant restrictions on a suitable mesh coarsening operation. One possibility is to basically try to reverse the refinement operation discussed above. To this end one can move two mesh-generating points close together over the course of a couple of timesteps, until they have essentially identical position. Once this is achieved, the Voronoi cells corresponding to the two points can simply be merged by replacing the two points with a single mesh-generating point at the same lo-

cation. The new cell then inherits the sum of the conserved fluid variables of the two merged cells.

However, there are several technical difficulties in this approach that make its application problematic in practice. For example, the decision for derefinement is not made for a single cell, but for two neighbouring cells simultaneously. In addition, several timesteps are needed to bring two mesh-generating points close together in a smooth fashion, either during the actual time evolution (over which the conditions for derefinement may well change) or during a pseudo-evolution where the density field is kept static and only the advection equation for the deforming mesh is solved.

Because of these difficulties, we have implemented an alternative derefinement strategy where a cell is dissolved instantly by simply removing its mesh-generating point from the tessellation. This means that the volume of the removed cell will be claimed by the surrounding Voronoi cells, as illustrated in Figure 16. It is then also natural to distribute the conserved fluid quantities (mass, energy, momentum) of the dissolved cell among these neighbours, in proportion to the claimed volume fractions. Working out the corresponding geometrical factors requires the construction of the Voronoi diagram of the neighbouring cells with and without the point that is removed.

A small complication in this approach is that the removal of a cell changes the geometry of all the neighbouring cells. This in turn may well change the outcome of the derefinement criterion for these neighbouring cells. For example, if all cells below a certain size are supposed to be derefined and two neighbouring cells are candidates for the derefinement, then the removal of one of them will make the other larger, so that it may no longer fulfill the derefinement criterion. To make the order of derefinement a well-defined procedure, we construct the list of cells that are derefined in a given timestep in the following way. First, we restrict ourselves to derefinement criteria that allow a priority ordering of some kind, i.e. we need to be able to unambiguously identify the cell that should 'most urgently' be derefined. Starting with this cell, we then flag cells for derefinement in the order of this urgency parameter. However, we skip all cells that already have a neighbouring cell that is flagged for derefinement in the same timestep. In this way we always have a well-defined set of cells that can be derefined in a given timestep, and only cells whose derefinement criteria are independent from each other are derefined in the same step. This also means that two neighbouring cells are never derefined in the same timestep. In Section 8, we will discuss a test problem (the Noh problem) where we apply both the refinement and derefinement strategy described here.

7   TIME INTEGRATION

In this section, we discuss issues of time integration. In particular, we introduce an individual timestep scheme that can be used for our finite volume discretization on an unstructured mesh. We will also address how we combine the hydrodynamics with the integration of a collisionless N-body system that represents dark matter or stars in galaxies. Finally, we detail how we implemented cosmological integrations in an expanding universe, and we explain the general struc-

ture of our new simulation code AREPO that implements the methods discussed in this paper.

7.1   Timestep criterion

For hydrodynamics with a global timestep, we employ a simplified CFL timestep criterion in the form

$$\Delta t_i = C_{\mathrm{CFL}} \frac{R_i}{c_i + |\boldsymbol{v}_i'|} \tag{109}$$

to determine the maximum allowed timestep for a cell i. Here R_i is the effective radius of the cell, calculated as $R_i = (3V_i/4\pi)^{1/3}$ from the volume of a cell (or as $R_i = (V_i/\pi)^{1/2}$ from the area in 2D), under the simplifying assumption that the cell is spherical. The latter is normally a good approximation, because we steer the mesh motion such that the cell-generating point lies close to the centre-of-mass of the cell, which gives it a "roundish" polyhedral shape. $C_{\mathrm{CFL}} < 1$ is the Courant-Friedrichs-Levy coefficient (usually we choose $C_{\mathrm{CFL}} \simeq 0.4 - 0.8$), $c_i = \sqrt{\gamma P/\rho}$ is the sound speed in the cell, and $|\boldsymbol{v}_i'| = |\boldsymbol{v}_i - \boldsymbol{w}_i|$ is the velocity of the gas *relative to the motion of the grid*. In the Lagrangian mode of the code, the velocity $|\boldsymbol{v}_i'|$ is close to zero and usually negligible against the sound speed, which means that larger timesteps than in an Eulerian treatment are possible, especially if there are large bulk velocities in the system.

If the code is operated with a global timestep, we determine the next system timestep as the minimum

$$\Delta t = \min_i \Delta t_i \tag{110}$$

of the timestep limits of all particles. In simulations with gravity, we also impose a second kinematic timestep criterion for each particle, as described in Springel (2005), and we restrict the maximum allowed timestep to a suitable value. However, we have also implemented an individual timestep scheme, where the different timestep conditions of different cells are treated in a more flexible and computationally efficient fashion. This is discussed next.

7.2   Individual timesteps

In typical cosmological simulations, a large dynamic range in densities quickly occurs as a result of gravitational clustering. Accordingly, local dynamical times can vary by orders of magnitude. It has hence long been common practice to use individual timesteps for the collisionless N-body problem, a technique that has also been extended to hydrodynamical SPH simulations (e.g. Katz et al., 1996; Springel et al., 2001). However, the use of individual timesteps in mesh-based finite volume codes is more problematic and appears to be rarely used, except in the context of AMR simulations. In the latter, individual refined grid patches are typically subcycled in time (frequently by a factor of 2 if the refinement factor is 2) relative to their parent grid. Refluxing techniques are then used to assure that a fully conservative solution is obtained on the coarser parent grid as well. Note that in this approach the same volume is effectively covered multiple times.

We aim for another solution, because in the moving mesh approach the cell size may vary greatly without an
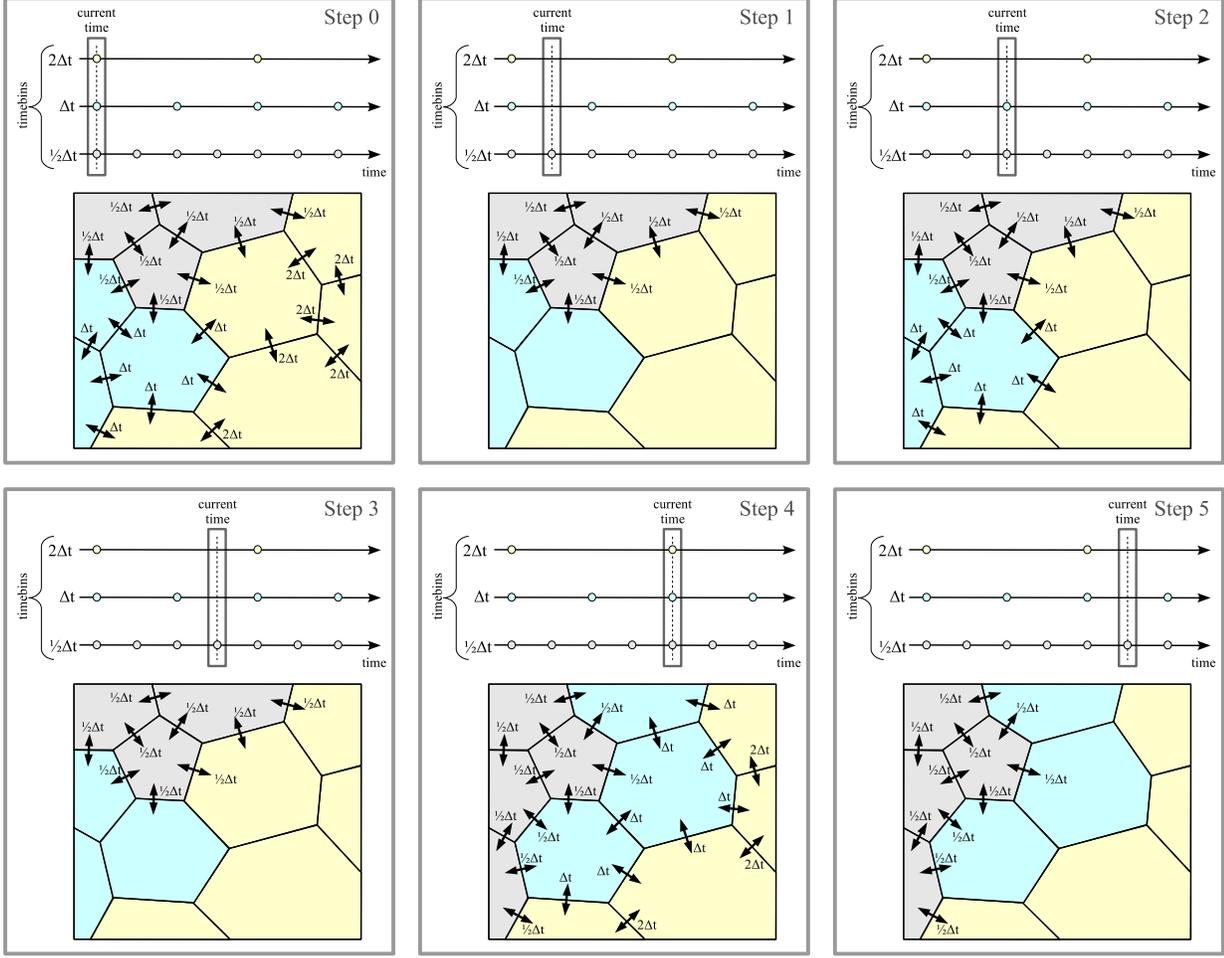
Figure 17. Sketch of the individual time integration scheme used in AREPO for the hydrodynamics. The mesh cells in this example occupy three different timebins, and are coloured accordingly in the sketch. In each timestep, fluxes are calculated for all faces where at least one of the cells is active on the current timestep. The cells then exchange conserved quantities on the smaller of the two timestep sizes of the two neighbouring cells of each active face. A cell has the possibility to reduce its timesteps at the end of each step, but can only move to a timestep twice larger every second step in order to maintain a nested synchronization of the timestep hierarchy.

associated nested grid structure. In order to save computational time in simulations with a large dynamic range, we would like to be able to evolve only certain parts of the mesh with a small timestep, and other parts with a larger step size. At the same time we want to retain the conservative character and the stability of the finite-volume approach that is obtained for a global timestep.

Our approach to address these requirements is based on a discretization of the allowed timestep sizes into a power-of-two hierarchy, similar to the approach frequently adopted in cosmological SPH codes (e.g. Katz et al., 1996). This means that the actual timestep Δt_i of a cell i is determined by taking the largest power of 2 subdivision that is smaller than the timestep criterion of equation (109). This effectively puts the cells into a set of timestep bins that form a nested hierarchy of possible timesteps, providing for a partial synchronization of the timesteps of different cells.

Our individual timestep integration of the unstructured mesh is based on the principle that, if two adjacent cells have different timesteps, their common face is evolved with the smaller of the two steps. This leads to a time-integration

scheme that is graphically explained in the sketch of Figure 17. In this example, in 'Step 0', the current system time is synchronized with the start of all three timestep sizes that are present. As a result, the Voronoi mesh needs to be generated for all cells present in the system, and fluxes are estimated for all of the faces. However, the flux estimate is done for different timestep sizes, depending on the timesteps of the involved cells, as indicated in the sketch. For each face, always the smaller timestep of the two neighbouring cells is used as actual timestep, and the time-integrated fluxes estimated for the faces are used to update the conservative quantities of the two adjacent cells.

Once the step is completed, the system time is advanced to the next beginning/end of occupied timestep bins, and step 1 in Fig. 17 begins. For cells that have completed their timestep (these are the ones marked with timestep size '$1/2\Delta t$'), new primitive fluid variables and gradients are estimated, but the other cells continue to use their old primitive variables and gradients for half-step predictions and flux estimates. Also, their mesh-generating points continue to move with the velocities assigned in their last active step. In step
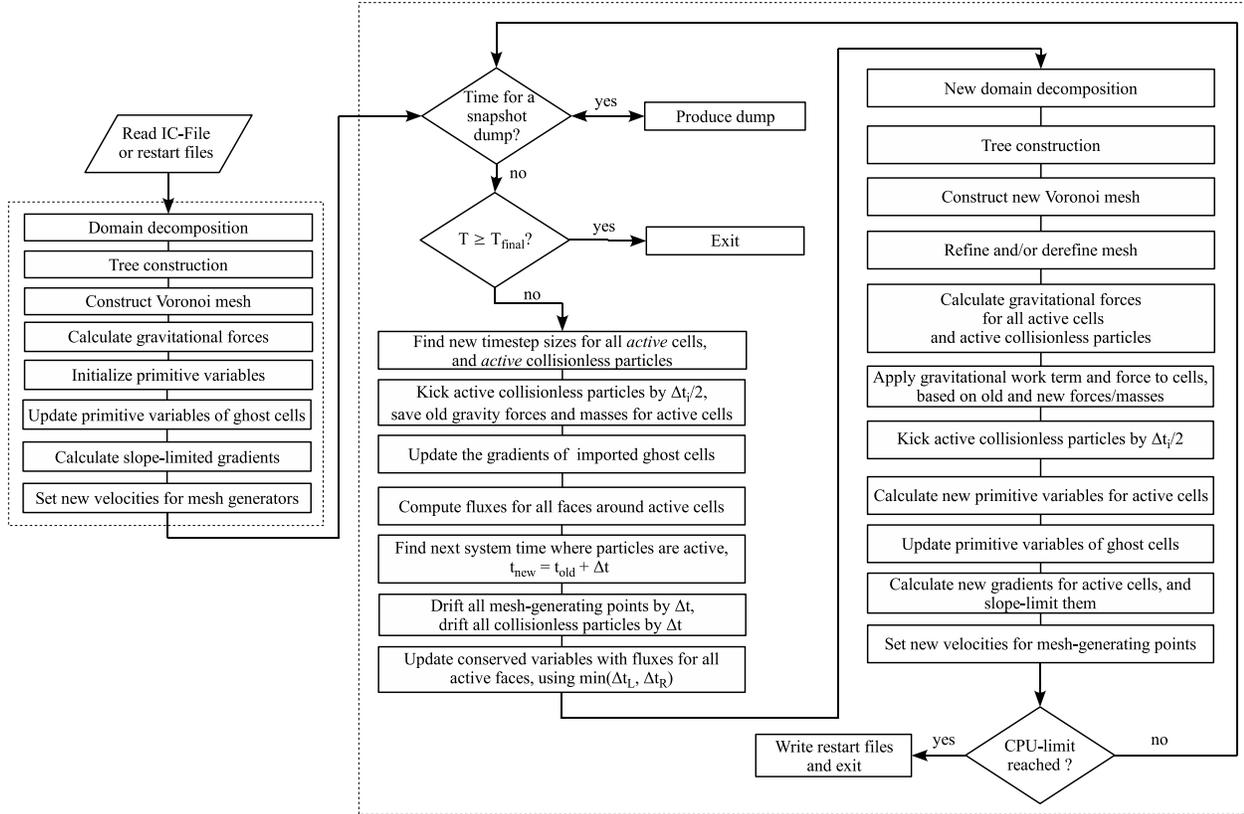
Figure 18. Flow chart of the simulation code. After a number of initialization steps (marked by the dashed box on the left), the code enters a main loop. In each iteration of the main loop, the system advances by a time interval Δt that corresponds to the smallest occupied timebin. Active cells or collisionless particles are always those with a timestep that is in sync with the current time of the system. In the first phase, operations correspond to active particles beginning their timestep, in the second phase to those that end their timestep.

1, only a much smaller set of the faces is active during the step, and only those cells of the Voronoi mesh need to be constructed that have at least one active face. We achieve this by inserting only the mesh-generating points of such active cells into the mesh, and by ensuring the completeness of their Voronoi cells with the search radius technique discussed in subsection 2.4. Fluxes are estimated only for the active faces, and used to update the conservative quantities of the involved cells. This process repeats again in step 2 and step 3. Whenever a cell has completed its timestep, its primitive variables are updated based on the accumulated changes of its conserved quantities. Also, the cell may then change its timestep size. The timestep can always become smaller after a step has been completed, but it can only increase if the higher timestep level is synchronized with the current time, i.e. if the target timebin starts one of its steps at the current time. This means that a cell may increase its timestep only every second step. An example for timestep changes is seen in step 4 of the sketch in Fig. 17: After having completed step 3, a few cells reduce their timestep, and others increase it. With this change, the system is then integrated forward in time through steps 4 and 5.

By construction, the above scheme is conservative as it only involves pairwise exchanges of conserved fluid quantities. We have also found it to perform accurately in practice, in the sense that we obtained comparable accuracy in

simulations where a global timestep or the more efficient individual timestep scheme were used. A specific test of this will be discussed in Section 8.

A crucial point lies in the determination of suitable individual timesteps; this obviously can have a large impact on the accuracy of the individual timestep scheme, as well as on the efficiency gain that can be realized with it. The timestep criterion of equation (109) is purely local, and is only appropriate for hydrodynamical waves that travel with the local sound speed. If a supersonic shock wave is approaching, the local gas element would be ignorant of it until the shock has arrived, and may therefore be put on an inadequately large timestep just before the shock strikes. We hence need to determine adequate timesteps by somehow taking information about distant regions into account. The idea is that any given cell should estimate the earliest time when it could become affected by the gas present in some other cell, and this would then provide a suitable maximum individual timestep. To make this concept more explicit, we define a 'signal speed' (Whitehurst, 1995; Monaghan, 1997) between two cells i and j,

$$v_{ij}^{\mathrm{sig}} = c_i + c_j - \boldsymbol{v}_{ij} \cdot \boldsymbol{r}_{ij}/r_{ij}, \tag{111}$$

where the velocity difference $\boldsymbol{v}_{ij}$ of the two cells is projected onto their separation vector. We then require that the timestep of cell i should be smaller than the travel time

of this signal over the distance r_{ij} of cells i and j. This means we replace the timestep criterion of equation (109) with

$$\Delta t_i = C_{\mathrm{CFL}} \min \left(\tau_i, \ \frac{R_i}{c_i + |\boldsymbol{v}'_i|} \right), \tag{112}$$

where

$$\tau_i = \min_{j \neq i} \left(\frac{r_{ij}}{c_i + c_j - \boldsymbol{v}_{ij} \cdot \boldsymbol{r}_{ij}/r_{ij}} \right). \tag{113}$$

The timestep of equation (112) is the maximum allowed timestep for cell i, and can be used in our individual timestep approach.

A brute-force calculation of this timestep criterion would be a prohibitive N^2 process. However, we can use a hierarchical tree-based grouping of the particles for a much more rapid evaluation of the timestep criterion, with a cost of order $\mathcal{O}(\log N)$ per particle. For this purpose we use the same oct-tree that we anyway employ for neighbour search (as needed in the parallelized mesh construction, see Fig. 9) and the gravity calculation. For each tree node, we store the maximum sound speed c^{max}, and the maximum velocity magnitude v^{max} for all the cells with their mesh-generating points contained in the node. The calculation of the maximum allowed timestep is then done with a special tree walk. We start the walk with a first guess for the timestep, equal to $\Delta t_{\mathrm{current}} = R_i/(c_i + |\boldsymbol{v}'_i|)$. If a single particle $j \neq i$ is encountered, its value of $r_{ij}/v^{\mathrm{sig}}_{ij}$ is computed and used to update $\Delta t_{\mathrm{current}}$ if it is smaller. If a tree node is encountered, we calculate a special tree opening criterion, of the form

$$d_{\mathrm{min}} < \Delta t_{\mathrm{current}} \left(c_i + c^{\mathrm{max}} + |\boldsymbol{v}_i| + v^{\mathrm{max}} \right), \tag{114}$$

where d_{min} is the smallest distance of the point $\boldsymbol{r}_i$ to the boundaries of the node under consideration. If this condition is fulfilled, the tree node is opened and its daughter nodes are considered in turn, otherwise the tree walk along this branch of the tree can be discontinued because there cannot be a particle inside the node that would require a smaller timestep than the current one. When the tree walk finishes, the timestep of cell i is finally given by $\Delta t_i = C_{\mathrm{CFL}} \Delta t_{\mathrm{current}}$.

We note that this scheme is more general and flexible than the suggestion by Saitoh & Makino (2009) to restrict the timestep choices of a particle (cell) by the timesteps of its immediate neighbours. Our approach can choose optimum timesteps even under extreme conditions. For example, one can imagine a high-speed collision of two self-gravitating cold blobs of gas. While the blobs are still separate, our scheme would assign large timesteps to them, allowing them to efficiently propagate through space, but right before the physical collision starts, the timesteps would be reduced appropriately. We also note that the above scheme produces Galilean-invariant timestep choices.

7.3 Cosmological integration

In an expanding Friedman-Lemaitre cosmology, the Euler equations need to be modified by source terms that describe the decay of velocities and energies due to the expansion of space. It is convenient to describe the fluid positions in terms of comoving coordinates $\boldsymbol{x} = a\boldsymbol{r}$, where a is the cosmological scale factor $a = 1/(1 + z)$ and z is the redshift. We also define a comoving density $\rho_c \equiv a^3 \rho$, and a 'comov-
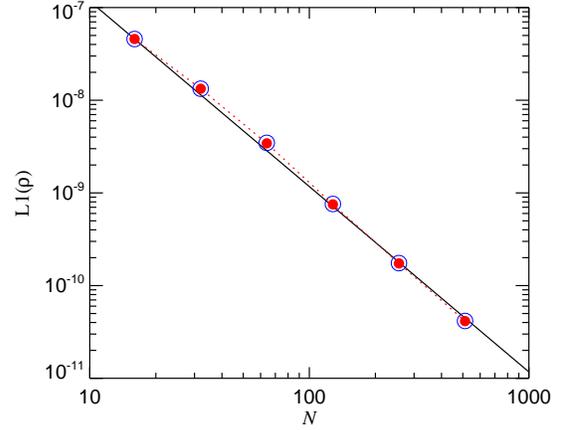
Figure 19. L1 error norm for an acoustic wave in one dimension, calculated with the moving-mesh code (red circles), or with a fixed mesh (blue open circles). The two schemes produce nearly identical errors (the moving mesh code lies only $\sim 1 - 2\%$ lower), and the solution converges as $L1 \propto N^{-2}$, i.e. with second order accuracy.
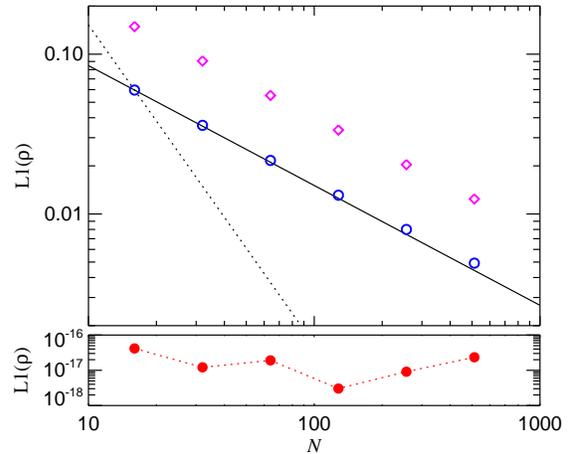
Figure 20. L1 error norm for a contact discontinuity (a density step from $\rho = 1$ to $\rho = 2$ that moves once through a box. The blue circles show the error as a function of resolution when we use our code with a Cartesian mesh with a fixed grid. In the presence of the discontinuity and the need to advect it the global rate of convergence is reduced to only about $L1 \propto N^{-3/4}$. However, for the moving-mesh code, shown with red circles, the error is *consistent with zero* within floating point rounding errors. For comparison, we also show with diamonds the L1 error of the same test carried out with ATHENA (using 2nd order reconstruction and the Roe solver). The dotted line illustrates a second-order scaling.

ing pressure' $P_c \equiv (\gamma - 1)\rho_c u$. The Euler equations in an expanding universe can then be written as

$$\frac{\partial \rho_c}{\partial t} + \frac{1}{a} \boldsymbol{\nabla}_c (\rho_c \boldsymbol{v}) = 0, \tag{115}$$

$$\frac{\partial (\rho_c \boldsymbol{v})}{\partial t} + \frac{1}{a} \boldsymbol{\nabla}_c [(\rho_c \boldsymbol{v}\boldsymbol{v}^T + P_c)\boldsymbol{v}] = -H(a)\,\rho_c \boldsymbol{v} - \frac{\rho_c}{a^2} \boldsymbol{\nabla}_c \Phi_c, \tag{116}$$

$$\frac{\partial(\rho_c e)}{\partial t} + \frac{1}{a}\boldsymbol{\nabla}_c[(\rho_c e + P_c)\boldsymbol{v}] = -2H(a)\,\rho_c e - \frac{\rho_c \boldsymbol{v}}{a^2}\boldsymbol{\nabla}_c \Phi_c. \quad (117)$$

Here $\boldsymbol{v} = a\,\dot{\boldsymbol{x}}$ is the peculiar velocity. The specific energy is defined in terms of the peculiar velocity as $e = u + \boldsymbol{v}^2/2$. The gradient operator $\boldsymbol{\nabla}_c$ acts on the comoving coordinates $\boldsymbol{x}$, and $H(a) = \dot{a}/a$ is the Hubble expansion rate. Φ_c is the comoving peculiar gravitational potential, which is the solution of

$$\nabla_c^2\,\Phi_c = 4\pi G\,[\rho_c(\boldsymbol{x}) - \overline{\rho_c}], \quad (118)$$

where $\overline{\rho_c}$ is the mean comoving density of the universe.

Integrating these equations over the comoving volume of a Voronoi cell, it is easy to see that suitable 'conservative' variables are still given by mass, momentum and energy of a cell, except that the total momentum and total energy of the simulated system are not strictly conserved any more due to the presence of the terms involving $H(a)$. However, surface integrals over cells simply yield the ordinary fluxes of the Euler equations, evaluated with the physical fluid quantities and the physical areas of the cell interfaces. Hence we can continue to use the Godunov approach for determining the fluxes, and they themselves are still fulfilling a detailed balance between cells.

To incorporate the loss terms due to cosmological expansion, we proceed similarly as for the gravitational source terms. To calculate time-centred fluxes, we incorporate the decay terms in the half-step prediction of the primitive variables and then obtain a second-order accurate update for the full step by evaluating the loss terms at the beginning and end of the step. For example, for the energy contained in a cell, this takes the form

$$E_{n+1} = E_n + \Delta E_{\text{flux}} - [H(a_n)E_n + H(a_{n+1})E_{n+1}]\,\Delta t, \quad (119)$$

where E_{n+1} is the energy at the end of the step, and ΔE_{flux} denotes the accumulated energy flux into the cell across its surface. Note that equation (119) can be easily solved for the new energy E_{n+1} at the end of the step.

7.4 Structure of the AREPO code

In Figure 18, we show a basic flow-chart of the new cosmological hydrodynamical code AREPO that implements the methods described in this paper, and which was used to calculate all the test problems discussed in the next sections. This code is parallelized for distributed memory computers, and is written in ANSI-C. Its input and output files largely match those of the TreePM/SPH code GADGET-2, such that a comparison of moving-mesh calculations with corresponding ones done with SPH is straightforward.

The AREPO code allows a variety of different types of simulations, both in 2D and 3D. Self-gravity of the gas can be included, and is either computed with a pure Tree or a TreePM approach. A collisionless dark matter or stellar fluid can be optionally included as well. Simulations both in Newtonian space, or in an expanding universe are possible. Also, fully adaptive, individual timesteps are supported both for the gas and the dark matter particles. The flow chart of Figure 18 shows how the code arranges the different calculational steps. We have also implement additional physics modules into our new code, such as radiative cooling, star formation, and energy feedback processes, following the

treatment in the most recent version of the GADGET code. Details of these implementations will be described elsewhere.

8 HYDRODYNAMICAL TEST PROBLEMS

In this section, we consider a number of hydrodynamical test problems in order to assess the accuracy and robustness of our new moving-mesh code. We will frequently compare the results with calculations that start from identical initial conditions but do not allow for a motion of the mesh-generating points. In this case, our code should behave equivalently to a standard Eulerian scheme with second-order accuracy in space and time. For a few of the test problems we investigate this aspect explicitly by also comparing with the publicly available, high-accuracy MHD code ATHENA (Stone et al., 2008). A number of our test problems also allow comparisons with results published in the literature for other codes. Note that tests involving self-gravity are discussed separately in Section 9.

8.1 One-dimensional waves

We begin with arguably one of the most elementary hydrodynamical test problems, the treatment of simple waves in one dimension. This, in particular, can serve as a sensitive test of the convergence rate of the code (see, e.g., the discussion in Stone et al., 2008). We first consider simple acoustic waves. Following Stone et al. (2008), we initialize a traveling sound wave of very small amplitude $\Delta\rho/\rho = 10^{-6}$ (to avoid any wave steepening) and with unit wavelength in a periodic domain of unit length and unit density. We use a one-dimensional version of the code in this test, where the Voronoi faces can be easily constructed at the mid-points of the mesh-generating points. However, we have checked that the same results are also obtained with the two-dimensional version of the code. The pressure is set to $P = 3/5$, such that the adiabatic sound speed is $c_s = 1$ for a gas with $\gamma = 5/3$. The mesh-generating points are moved with the local velocity of each cell, without terms for mesh regularization.

We let the wave travel once through the box, and compare the final result with the initial conditions in terms of an L1 error norm. We define the latter as

$$\text{L1} = \frac{1}{N}\sum_i |\rho_i - \rho(x_i)|, \quad (120)$$

where N is the number of cells, ρ_i the numerical solution for cell i, and $\rho(x_i)$ is the expected analytic solution for the problem (which is equal to the initial conditions in this first test).

In Figure 19, we show results for the error norm for the acoustic sound wave test as a function of the number of cells, both for a fixed-mesh, and for the moving mesh. Reassuringly, the results demonstrate global second order convergence of the code, as expected for a smooth problem like this one. This is true both for the moving-mesh approach, as well as when we keep the mesh fixed, with almost identical errors. Furthermore, we note that the absolute size of the errors are very similar to what Stone et al. (2008) achieved with ATHENA.

Next, we consider a more demanding test, the advection of a contact discontinuity once through the box. To this end,
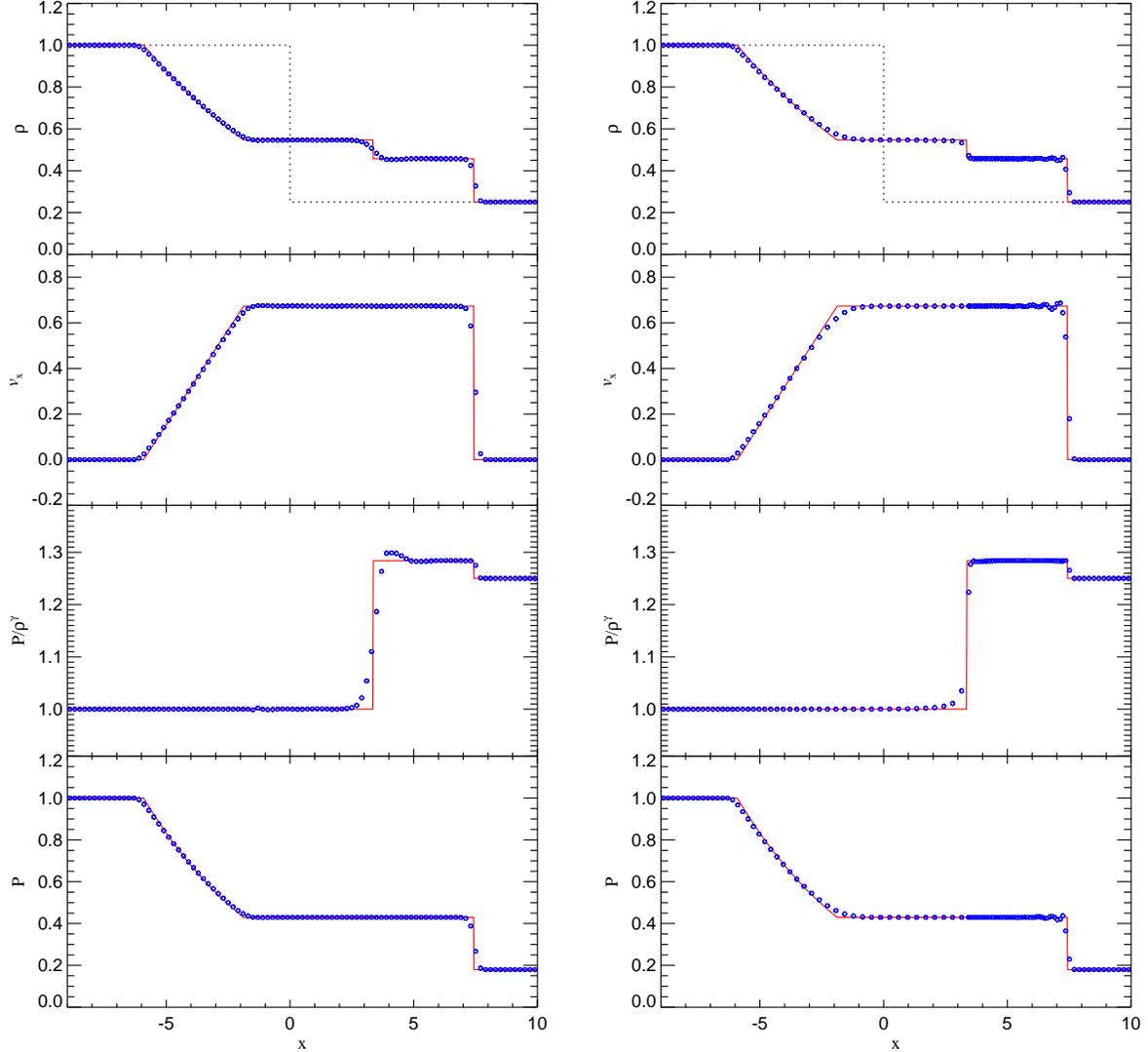
Figure 21. A shock tube test with initial conditions frequently used in previous code tests (Hernquist & Katz, 1989; Rasio & Shapiro, 1991; Wadsley et al., 2004; Springel, 2005). The panel on the left shows the result (symbols) of a 2D test with equal volume per cell and a fixed mesh, the right when the mesh is allowed to move. The solid lines show the analytic solution, and the dotted lines in the top row mark the initial conditions.

the left half $x < 0.5$ of the box is set to density $\rho = 1$, and the right half to density $\rho = 2$, with pressure $P = 3/5$ everywhere. We now let this contact discontinuity move once through the box with velocity $v_x = 1.0$ everywhere. In Figure 20 we show the L1 error as a function of resolution if a fixed mesh is used. Now the convergence is in fact only $L1 \sim N^{-0.75}$. This is simply reflecting the numerical diffusivity of the Eulerian approach for contact discontinuities. We have checked that ATHENA also shows the same scaling of the error if second-order reconstruction is used. On the other hand, for our moving mesh code, the error is *consistent with zero to machine precision, $L1 \lesssim 10^{-17}$*. This is of course the expected result for a Galilean-invariant scheme, as for $v_x = 0$ the fixed mesh recovers the analytic result. This illustrates in a first practical application the accuracy gain offered by a moving-mesh: pure advection errors are reduced or eliminated. On the other hand, the error for the

Eulerian result is primarily set by the distance over which the discontinuity needs to be advected, largely independent of the velocity of the flow. It is hence a strong function of the reference frame picked for the calculation.

8.2 Shock-tube test

We continue our investigation of basic hydrodynamical test problems with a one-dimensional Sod shock tube. For definiteness, we pick a left state ($x < 0$) described by $P_1 = 1$, $\rho_1 = 1$, and $v_1 = 0$, and a right state ($x \geq 0$) given by $P_2 = 0.1795$, $\rho_2 = 0.25$, and $v_2 = 0$, in a gas with adiabatic index $\gamma = 1.4$. Of course, a large number of other simple Riemann problems are equally well possible. We have adopted these parameters because they were previously used in a number of other code tests (Hernquist & Katz, 1989; Rasio
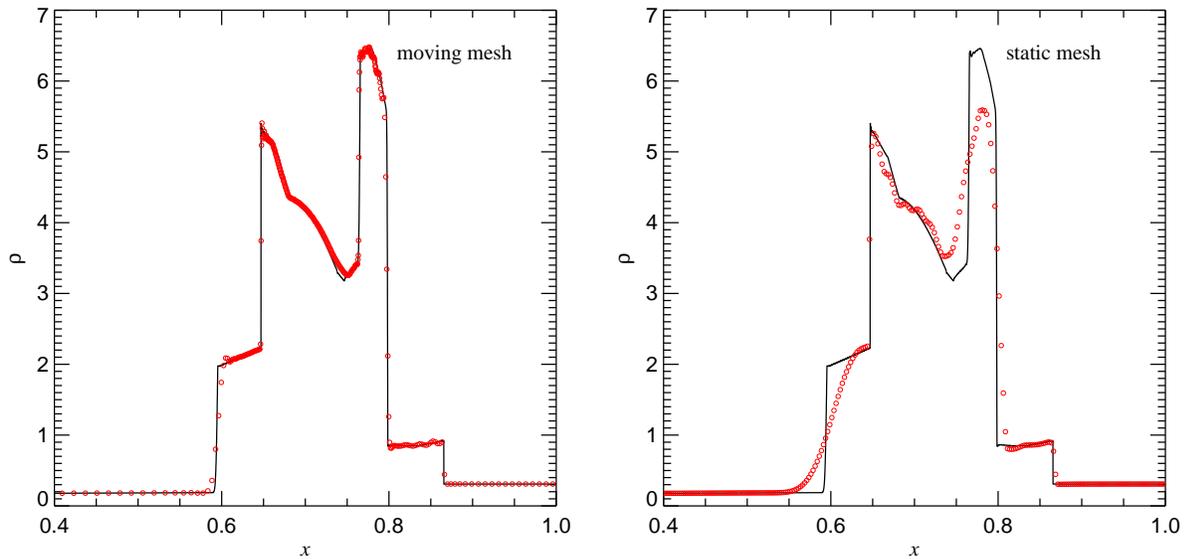
Figure 22. Density profile at time $t = 0.038$ of the interacting double blast wave problem of Woodward & Colella (1984), for a resolution of 400 cells in the domain $[0, 1]$. The panel on the left shows our result for the moving mesh-code, while the panel on the right is based on the same initial conditions but using a fixed mesh. The red circles mark density values for individual cells of the 400-cell calculation, while the solid line is a high-resolution calculation with 20000 cells and a fixed mesh, for comparison.

& Shapiro, 1991; Wadsley et al., 2004; Springel, 2005, among others).

We sample the problem with points of spacing $\Delta x = 0.2$ along the x-axis, and examine the solution at time $t = 5.0$. Note that in our moving mesh-calculation this means that the cells start out with unequal masses. We however refrain here from trying to adjust the mesh motion such that the masses per cell become equal. Rather, the mesh motion is simply taken to be given by the local flow velocity in the moving-mesh case. We have set-up this problem in a two-dimensional domain to also test the 2D mesh generation, even though this problem could of course be more efficiently calculated with the 1D version of our code.

In Figure 21, we compare the shock-tube results, both for our moving-mesh code and the fixed-mesh case, with the analytic result expected for this Riemann problem. Both calculations produce a sharply resolved shock (of Mach number $\mathcal{M} = 1.48$), but there is a trace of small post-shock oscillations in the Lagrangian calculation. Presumably, this could be avoided with a more sophisticated wave-by-wave flux limiting procedure that would give our scheme the total-variation-diminishing (TVD) property, which it presently does not have due to the simpler MUSCL-Hancock approach. Note that the contact discontinuity is smoothed out quite noticeably in the Eulerian calculation, which also gives rise to a corresponding error in the entropy profile across the contact discontinuity. As we have also seen above, this is a generic feature in Eulerian methods and results from advection errors in evolving the moving contact discontinuity. In contrast, the contact discontinuity is very sharp in the moving-mesh calculation, and it *stays sharp* as a function of time. The conclusion that one may draw from this test is hence that the moving-mesh approach can resolve shocks just as well as an Eulerian method on a fixed mesh, but it

is able to produce more accurate results for contact discontinuities.

8.3 Interacting blast waves

Another classic one-dimensional test problem is the interaction of two strong blast waves, as introduced by Woodward & Colella (1984). Here a gas of density $\rho = 1$ with adiabatic index $\gamma = 1.4$ in the domain $x \in [0, 1]$ is initially at rest. The pressure is set to $P = 1000$ for $x < 0.1$, to $P = 100$ for $x > 0.9$ and to $P = 0.01$ elsewhere. The boundary conditions are reflective on both sides. The time evolution of this problem features multiple interactions of strong shocks and rarefactions, which provides for a sensitive test of a hydrodynamical code.

We follow Stone et al. (2008) and study a low resolution calculation of the problem with 400 equally spaced points in the domain of width $L = 1$. We consider both a calculation with a fixed mesh, and one with a moving mesh; in the latter case, the mesh-generating points are moved with the local flow velocity, so that the calculation is effectively Lagrangian, and mesh-regularization is carried out with $\eta = 0.1$ and $\chi = 1.0$. We use the 1D version of the code. For comparison purposes, we also compute a high-resolution result with a fixed mesh of 20000 cells, which serves as a proxy for a nearly exact solution.

In Figure 22, we show the density profile at time $t = 0.038$, at which point our results can also be compared with those of Stone et al. (2008) and Woodward & Colella (1984). Our 'Eulerian' fixed-mesh solution is similar in quality to that obtained with ATHENA by Stone et al. (2008), except that it shows slightly more diffusion in the contact discontinuities. This presumably reflects the benefits of the third-order reconstruction that Stone et al. (2008) had used for
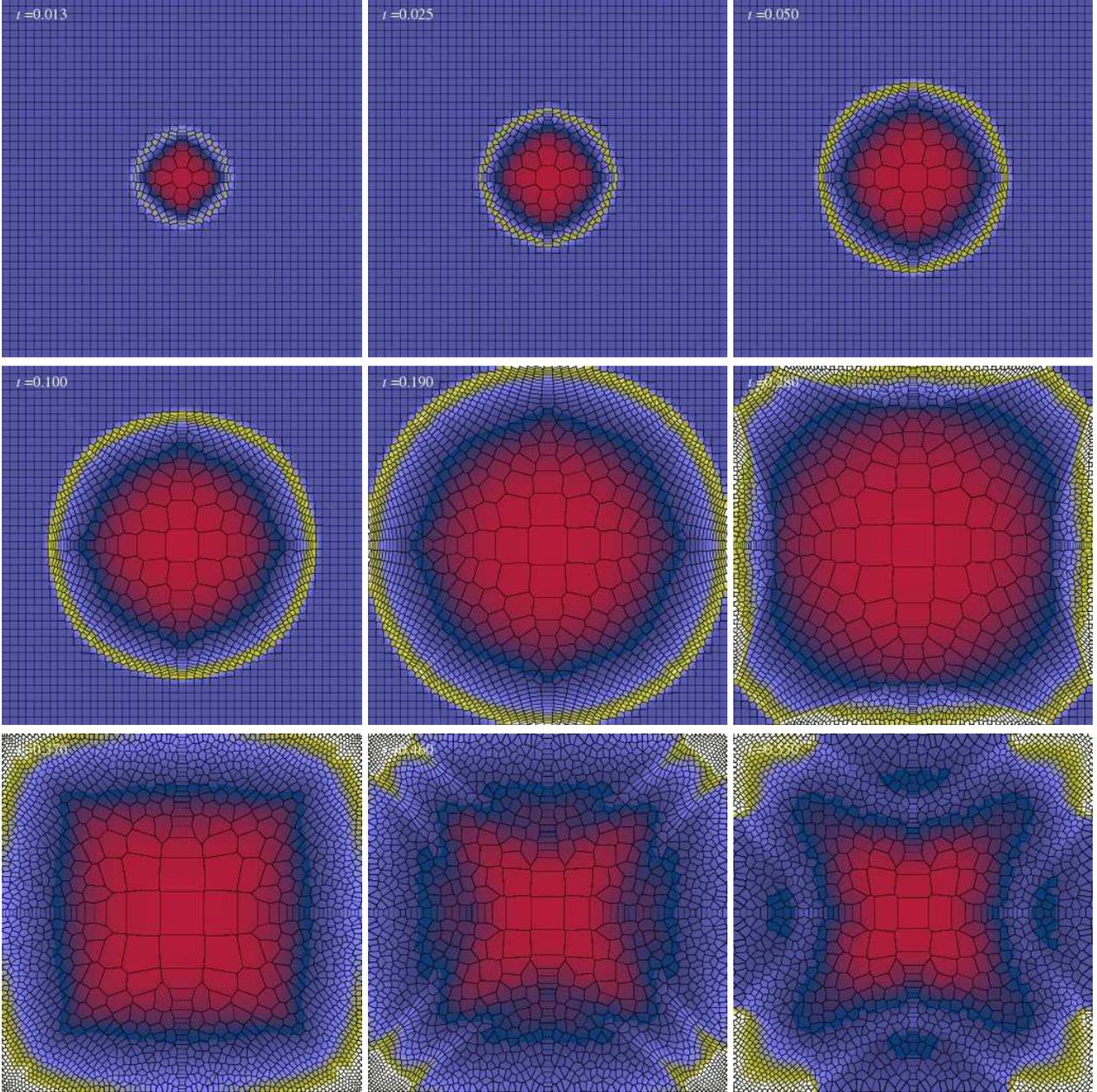
Figure 23. Time evolution of the density field in a 2D Taylor-Sedov blast wave calculation with the moving-mesh code. The time of each snapshot is indicated in the panels. The evolving Voronoi mesh is overplotted, and has a resolution of 45×45 cells. Roughly at time $t = 0.19$, the shock reaches the periodic boundaries of the domain of unit side length $L = 1$, and effectively collides with the blast wave of the periodic grid of explosions described by this set-up. This compresses much of the matter into the corners of the domain, a process that is well followed by the moving mesh.

this problem, while we have only employed our standard second-order scheme. Nevertheless, both Eulerian results show quite sizable smoothing of the contact discontinuities, especially for the one at $x \simeq 0.6$. On the other hand, the moving-mesh solution does much better in this respect. The deviations to the high-resolution result are much smaller everywhere, and in particular, the density maximum at $x \sim 0.8$ is recovered quite well and the discontinuities are resolved sharply. For the same number of cells, the moving-mesh code therefore clearly produces a more accurate solution. Similar

to the simple shock tube problem, we see that it is again the contact discontinuities that are improved most.

8.4 Point explosion

In this test, we inject an energy E into a point-like region in an initially homogeneous cold gas of density ρ. This results in a spherical Taylor-Sedov blast-wave, which has a well-known analytic self-similarity solution (e.g. Landau & Lifshitz, 1966). After a time t, the blast wave propagates to a distance $r(t) = \beta(Et^2/\rho)^{1/5}$, where the constant β de-
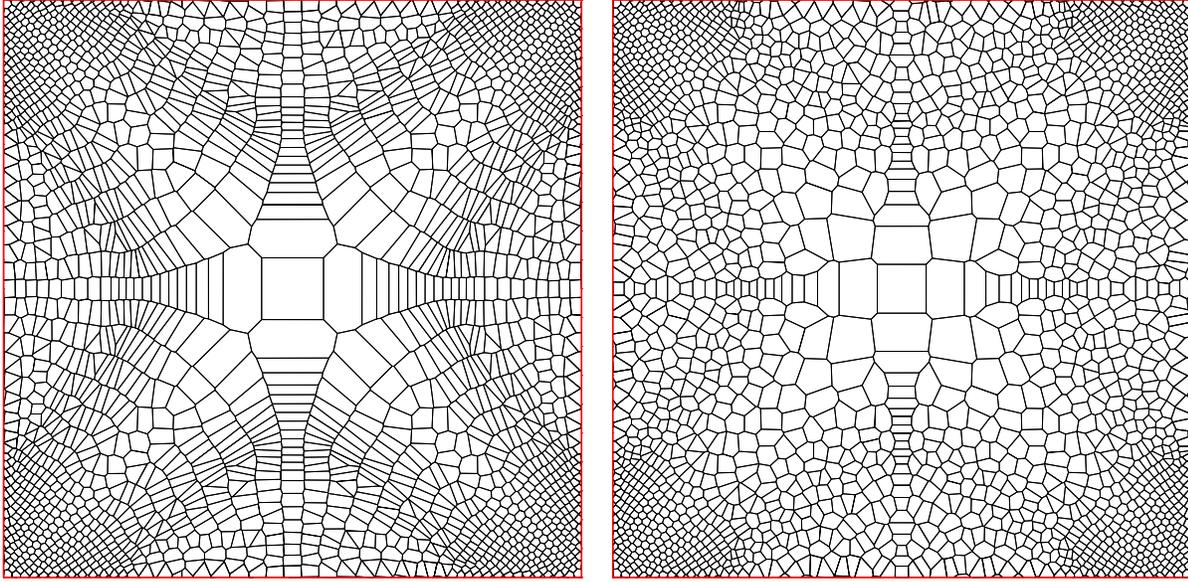
Figure 24. Effect of mesh regularization on the geometry of the Voronoi mesh. The panel on the left shows the Voronoi mesh obtained at $t = 0.55$ for the Sedov-Taylor blast wave test of Figure 23 when the mesh-generating points are only moved with the local gas velocity. While this produces a mesh well adjusted to the particular flow properties and symmetries of this problem, the high aspect ratio of some cells may be unfavourable in more general flows. The panel on the right shows the Voronoi mesh if we apply our standard mesh regularization procedure during the mesh motion. This tends to make the cells 'rounder' and more isotropic. Note that the predicted density distributions of both simulations are very similar.
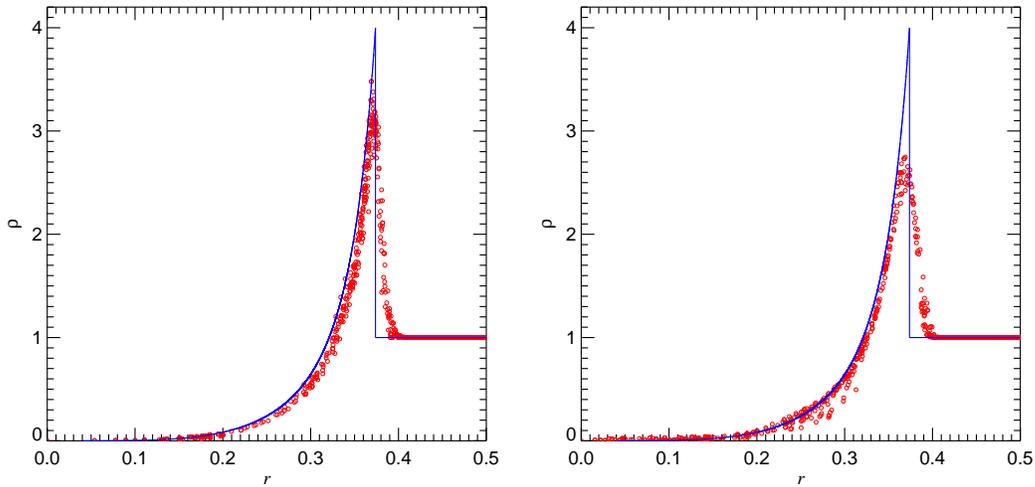
Figure 25. Density profile for a 3D Taylor-Sedov blast wave calculation at time $t = 0.06$. The initial resolution was 64^3 cells, with all the explosion energy injected into a single cell. We compare results for our moving-mesh code (left panel) with the result obtained for a fixed Cartesian mesh (right panel). The circles give the densities of individual cells, which have been randomly subsampled by about 1/200 to avoid too strong crowding.

pends on the adiabatic index γ ($\beta \simeq 1.15$ for $\gamma = 5/3$ in 3D), E is the explosion energy, and ρ describes the initial density of the ambient gas. Directly at the spherical shock front, the gas density jumps to a maximum compression of $\rho'/\rho = (\gamma + 1)/(\gamma - 1)$, with most of the mass inside the sphere being swept up into a thin radial shell. Behind the shock, the density rapidly declines and ultimately vanishes towards the explosion centre.

We first consider the 2D case, which allows us to illustrate the mesh motion in an easy way. In Figure 23, we show the time evolution of the density field with the mesh overlaid for a low-resolution calculation of the blast wave problem. Initially, the mesh-generating points for a gas of unit density are arranged in a 45×45 Cartesian mesh, and an energy of $E = 1$ is injected into the central cell. The mesh is allowed to move with the local flow velocity. We see that the prop-
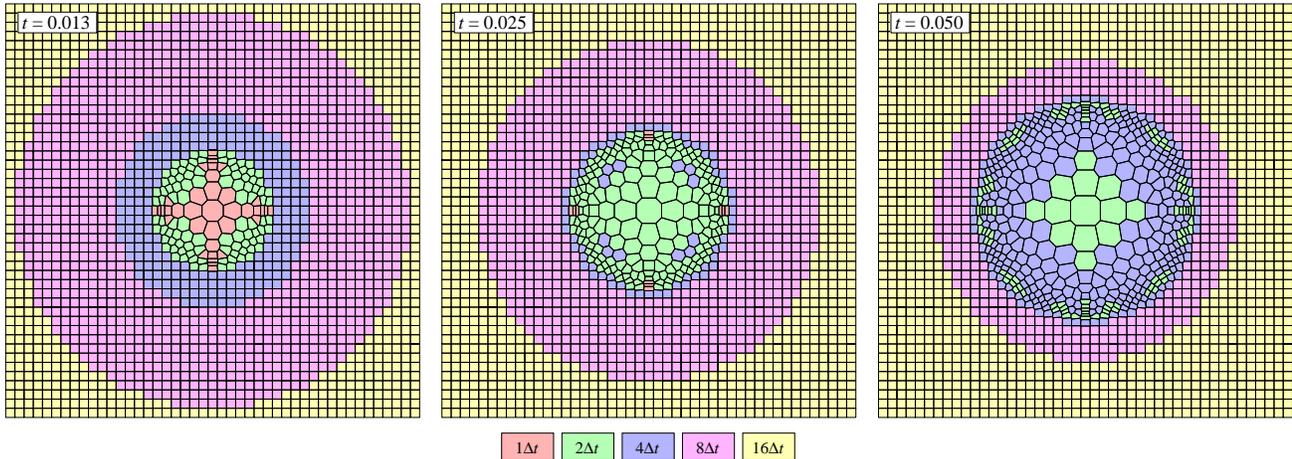
Figure 26. Spatial distribution of the sizes of individual timesteps in an integration of the two-dimensional Taylor-Sedov blast problem. The cells shaded in different colours are evolved with different timesteps in a power-of-two timestep hierarchy, as labeled. Fluxes between cells are always calculated on the smallest timestep of the two adjacent cells. Our tree-based approach to calculate the first possible arrival time of a signal from any other cell puts cells well ahead of the blast wave on sufficiently small timesteps.

agation of the blast wave is reflected in an evolving mesh geometry, with the smallest cells occurring where the mass piles up behind the shock. Periodic boundary conditions are used in this problem, so that the shock eventually collides with its mirror copies at the boundaries of the box. This compresses most of the mass temporarily into the corners of the box. However, the moving mesh algorithm can deal with this gracefully and robustly.

Actually, for the simulation displayed in Figure 23, the mesh was not moved just with the local flow velocity of each cell, but in addition the correction scheme of equation (63) was applied (using $\eta = 0.3$ and $\chi = 1.0$), which tries to keep mesh cells round. The effect of this can be seen in Figure 24, where the mesh geometry at time $t = 0.55$ is compared with (right) and without (left) any mesh regularization. Clearly, when the cells are moved with the local flow velocity alone, the mesh acquires some cells of quite high aspect ratio. Actually, the shape of the cells tends to adapt to the local flow features, for example, the cells become elongated parallel to the blast wave. This improves the spatial resolution in the direction of propagation of the shock front, which can be desirable in principle. In fact, this automatic resolution adjustment mimics attempts to make SPH more adaptive to local resolution requirements with the help of anisotropic kernels (Owen et al., 1998). However, for general flow problems, we argue that it is safer and more robust to avoid high aspect ratios, as one cannot rely on local symmetries for long, and the next shock wave may strike from another random direction. Also, as we discussed earlier, 'roundish' cells offer the best accuracy for spatial reconstruction and the treatment of self-gravity.

We now consider the accuracy of the shock front by comparing with the analytic solution. In Figure 25, we compare the densities of individual cells as a function of radial distance to the explosion centre, both for the moving-mesh approach, and for the code run with a fixed Cartesian mesh. The comparison is made at time $t = 0.06$, for an initial grid of 64^3 cells, now in 3D. Clearly, the moving-mesh approach resolves the sharp density spike of the blast wave

better, due to its improved spatial resolution in regions of high density. It also shows slightly weaker deviations from spherical symmetry at $r \sim 0.25$ compared with the Cartesian grid. There is a small phase error in the sense that the numerical simulation appears slightly more evolved than the analytical solution; the origin of this lies in the poorly resolved early phase of the point explosion. At later times, or for better resolution (which is essentially the same for this self-similar problem), this error becomes ever smaller. We note that Feng et al. (2004) give 256^3 results for their WENO solver, which curiously look somewhat worse than our results here despite their higher mesh resolution.

Finally, in Figure 26 we illustrate the behaviour of our individual timestep integration scheme for the 2D Taylor-Sedov blast wave problem. We show the mesh at three different times (corresponding to the first three panels shown in Fig. 23), with each cell shaded according to its assigned timestep. Far away from the explosion site, the allowed timesteps are significantly larger than close to the shock wave and in the heated central bubble. The timesteps are restricted in a sequence of spherical shells even ahead of the shock, such that the arriving shock wave is guaranteed to be integrated accurately in time, even though the cold gas far away can be integrated on timesteps that can in principle be orders of magnitude larger. This choice of timesteps is made possible by our tree-based scheme to estimate the earliest possible arrival time for every cell of a signal from any other cell.

We note that the results of the individual timestep scheme are essentially indistinguishable from a fixed timestep integration, but require significantly less computational effort. Compared to the equivalent calculation with a global timestep (set equal to the minimum of the local timestep constraint of all cells), 4.3 times fewer flux computations and Riemann problems have to be calculated over the course of a calculation from $t = 0$ to $t = 0.1$. For higher resolution or in 3D, the saving would be still larger. In fact, many physical applications in cosmic structure formation feature such a large dynamic range in timescales that indi-
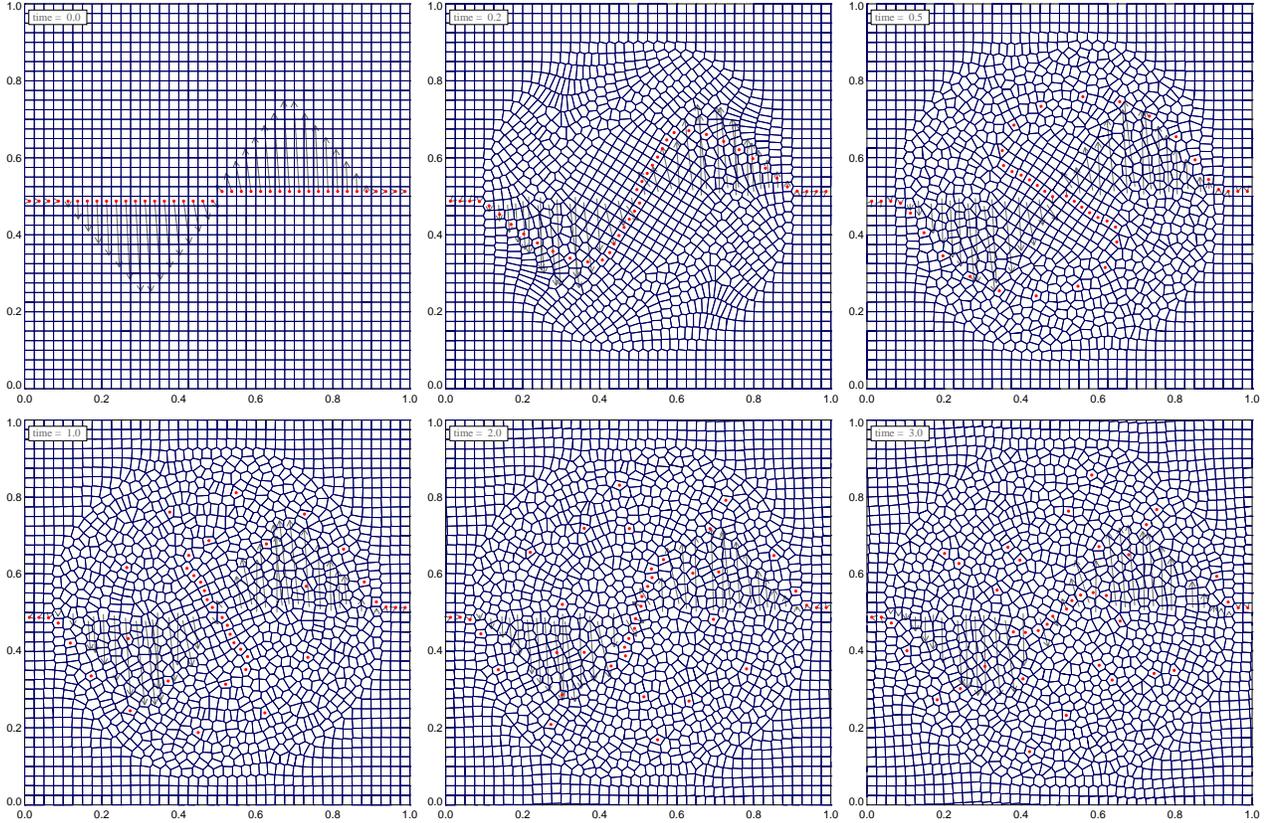
Figure 27. Mesh-motion in the 'triangular' vortex problem of Gresho, calculated with a 40×40 grid of particles. One horizontal row of particles in the initial distribution is marked with circles, and the same cells are labeled with circles in all subsequent frames.

vidual timesteps are mandatory to make large simulations still tractable.

8.5   The Gresho vortex problem

An interesting test for the conservation of vorticity and angular momentum is provided by the 'triangle vortex' problem of Gresho & Chan (1990), which we apply here to the Euler equations in 2D, following Liska & Wendroff (2003). The vortex is described by an azimuthal velocity profile

$$v_\phi(r) = \begin{cases} 5r & \text{for} \quad 0 \leq r < 0.2 \\ 2 - 5r & \text{for} \quad 0.2 \leq r < 0.4 \\ 0 & \text{for} \quad r \geq 0.4 \end{cases} \quad (121)$$

in a gas of constant density equal to $\rho = 1$. Thanks to a suitable pressure profile (Liska & Wendroff, 2003) of the form

$$P(r) = \begin{cases} 5 + 25/2r^2 & \text{for} \quad 0 \leq r < 0.2 \\ 9 + 25/2r^2 - & \\ \quad 20r + 4\ln(r/0.2) & \text{for} \quad 0.2 \leq r < 0.4 \\ 3 + 4\ln 2 & \text{for} \quad r \geq 0.4 \end{cases} \quad (122)$$

the centrifugal force is balanced by the pressure gradient and the vortex becomes independent of time. Note that in principle an arbitrary constant pressure could be added to the pressure profile.

We shall consider three different variants of this test. In the first, the vortex is at rest in the calculational frame,

which we describe by 40×40 cells in the unit domain at our default resolution (arranged initially as a Cartesian mesh). In the second and third variants, we follow Liska & Wendroff (2003) and let the vortex move with a constant velocity v_{vortex} along the positive x-direction, i.e. all the gas gets an additional velocity component of $\Delta v_x = v_{\text{vortex}}$. We consider the choices $v_{\text{vortex}} = 1$ and $v_{\text{vortex}} = 3$, and use periodic boundary conditions, such that the vortex moves 3 and 9 times, respectively, through the box over the simulated time span of $t = 3$ time units. The additional gas motion in the $v_{\text{vortex}} > 0$ case makes the problem more difficult for the Eulerian approach because it becomes more demanding to advect the gas accurately over the grid. In all cases, we run the problem for $t = 3$ time units, and then compare the azimuthal velocity profiles of the final with the initial state.

Before we discuss these results, we first illustrate in Figure 27 the time evolution of the mesh geometry produced by our moving-mesh code in the stationary vortex case. In order to guide the eye and to show the motion of individual mesh cells, a horizontal row of cells has been marked with circles in the initial conditions, and the same cells are then labeled again in all subsequent time frames. Also, for a vertical strip of cells, velocity vectors are added in the plots at each output time. It is nicely seen how the central region of the mesh accurately follows a solid body rotation in the early evolution, and how it is surrounded by an outer shell that exhibits strong shear. However, there is no pathological mesh twisting or tangling due to this shear. Rather,
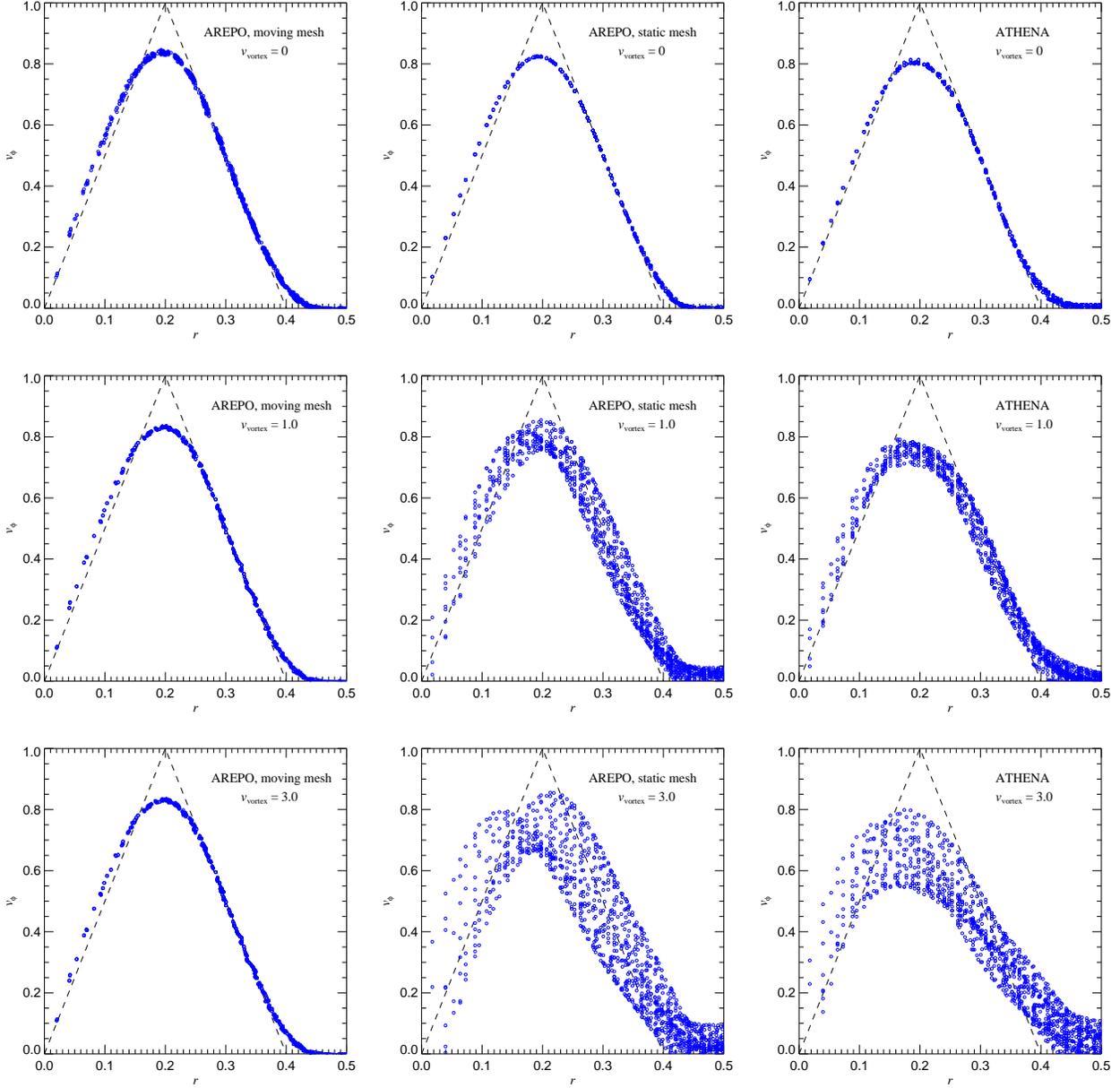
Figure 28. Azimuthal velocity profiles at time $t = 3.0$ for Gresho's 'triangular' vortex problem when calculated with different codes and for different bulk velocities of the vortex. In the panels of the top row, the vortex is stationary, while in the middle row it moves with a speed $v_x = 1.0$, and in the bottom row with $v_x = 3.0$, which is comparable to the speed-of-sound of the gas. We compare results calculated with our AREPO code, both for a moving mesh and a fixed Cartesian mesh, with those obtained using the ATHENA code (Stone et al., 2008). For $v_x = 0.0$, all three methods produce results of comparable quality. However, if the vortex is non-stationary, the Eulerian approaches develop significant asymmetries and show elevated diffusivity and angular momentum transport due to the increase in advection errors. In contrast, the Lagrangian moving-mesh result is invariant when the vortex is set in motion.

the Voronoi mesh transforms its geometry continuously, and changes the local neighbourhood relations between cells in a smooth fashion. As time goes by, the initial symmetry in the mesh geometry slightly deteriorates, but the mesh motion stays nicely regular.

In Figure 28, we compare the results for the azimuthal velocity profiles at the final time of all of our runs. In the top row of panels, we show calculations where the vortex was stationary relative to the computational frame. We give

results obtained with our new code both with a fixed mesh and with a moving mesh, based on identical initial conditions. To compare our results with another high-accuracy Eulerian code, we have also computed this problem with the publicly available code ATHENA by Stone et al. (2008). For the latter, we used second-order spatial reconstruction and the Roe solver. After 3 time units, all three codes show some significant smoothing of the initial velocity profile, but they do not differ strongly in the quality of the results.
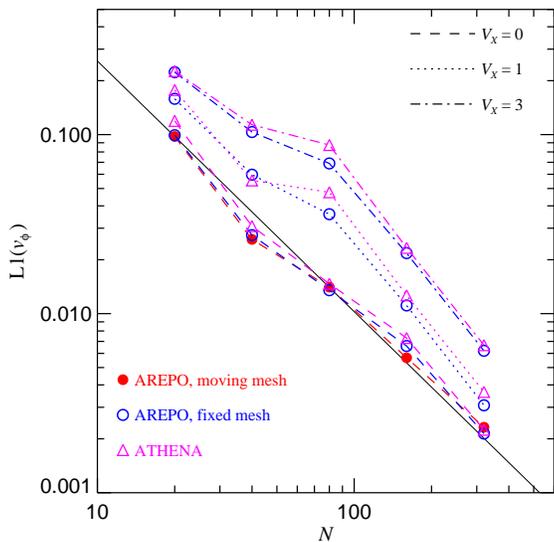
Figure 29. L1 error norm of the azimuthal velocity profile of the Greho vortex problem at time $t = 3.0$, as a function of initial mesh resolution ($N \times N$). We show results for three different bulk velocities of the vortex, $v = 0$, $v = 1$ and $v = 3$. The results for our moving-mesh code are shown as red circles – they are independent of the bulk velocity to machine precision. If we use a fixed Cartesian mesh instead, we obtain the results shown by the open blue circles. The three sets of results correspond to the different bulk velocities. In contrast to the moving-mesh code, the errors grow with increasing bulk velocity. Finally, for comparison with an independent Eulerian hydrodynamics code, we show the results obtained with ATHENA as triangles.

It is now interesting to consider the changes in these results when the vortex is set in motion. We show the corresponding results in the middle and bottom row of Figure 28, for the cases $v_{\rm vortex} = 1$ and $v_{\rm vortex} = 3$. Of course, in principle nothing should change, as the physical problem only differs by a Galilean transformation from the original setup of a stationary vortex. Indeed, our moving-mesh code produces the same result as before, and proves completely insensitive to this velocity boost, as expected for a Galilean-invariant formulation. Quite in contrast, both our own code when used with a fixed mesh as well as ATHENA show substantially degraded results in the moving vortex case. In particular, the symmetry of the vortex motion is partially lost (consistently with the results of Liska & Wendroff, 2003), and there is a larger degree of smoothing of the azimuthal velocity profile. Clearly, this is the result of additional numerical diffusivity and advection errors that now occur in the Eulerian treatment. A particularly troubling aspect of these errors is that they are a strong function of the velocity with which the vortex moves, as this determines the distance over which the system has to be advected during the simulated timespan. This becomes clear by comparing the results for different vortex velocities; increasing $v_{\rm vortex}$ and keeping the simulated timespan fixed, the error in the Eulerian calculations can be increased nearly arbitrarily. In contrast, the moving mesh code retains its original solution independent of the bulk motion of the vortex, which is physically a much more meaningful behaviour.

We now examine more quantitatively the convergence rate for this vortex problem. To this end we measure the L1 error for the azimuthal velocity profile at time $t = 3.0$, as a function of the mesh resolution. We compare the results obtained for the moving-mesh approach with those of the fixed mesh, again for our three different bulk velocities, $v_{\rm vortex} = 0$, $v_{\rm vortex} = 1$ and $v_{\rm vortex} = 3$. Our results are summarized in Figure 29, where we also include results obtained with ATHENA, for comparison. Clearly, for zero bulk velocity, the errors of our code AREPO are quite similar between the moving-mesh and the fixed-mesh, and also very close to the independent code ATHENA. Note that the results converge only approximately as L1 $\propto N^{-1.4}$, as indicated by the solid line in the plot. This is presumably a consequence of the discontinuities in the vorticity profile present in this problem, at $r = 0.2$ and $r = 0.4$. If a non-vanishing bulk velocity is included, we see significant accuracy differences between the moving-mesh and the fixed mesh. Whereas the moving-mesh results *do not change at all*, the error increases for the Eulerian approach with growing bulk velocity. The magnitude of this deterioration is consistent between AREPO and ATHENA. We argue that this highlights an important shortcoming of traditional Eulerian approaches.

In passing, we want to note that we also tried SPH on this problem, with the implementation of SPH in the GADGET3 code. It turns out that this is a hard problem for SPH, and a direct comparison with the results presented above shows SPH to be substantially less accurate when the same number of particles is used. In fact, for the lower resolutions, the vortex typically does not survive until $t = 3.0$; the angular momentum is transported to the boundaries of the domain before this time, where it is then effectively canceled by encounters with oppositely moving gas from the adjacent periodic image domains. We defer a more detailed comparison of SPH with the moving-mesh code to a future study.

8.6 The Noh problem

We now consider the strong shock test proposed by Noh (1987), which has an analytic solution. This is generally considered a very difficult problem, and quite frequently, numerical methods have problems running this test without crashing. In fact, in the test suite of Liska & Wendroff (2003), only four out of the studied eight schemes managed to run this problem at all. The set-up consists of a $\gamma = 5/3$ gas that has initially uniform density equal to $\rho_0 = 1$, vanishingly small pressure, and everywhere a radial inflow velocity towards the origin of $v = -1$. As a result of the inflow, a strong spherical shock wave of formally infinite Mach number develops and travels outwards with a speed $v_s = 1/3$. Inside of the shock front, the density is constant; it has a value of 4 in the 1D case, 16 in the 2D case, and 64 in the 3D case. Outside of the shock, the density profile is given by

$$\rho(r, t) = \rho_0 \left(1 + t/r\right)^n, \tag{123}$$

with $n = 2$ in the 3D case, $n = 1$ for the 2D case, and $n = 0$ for the 1D case.

The problem has been considered in 1D, 2D, and in 3D in the literature, but we restrict ourselves to two- and three-dimensional tests. As in previous studies of this problem, we calculate only one quadrant when a Cartesian mesh is used,
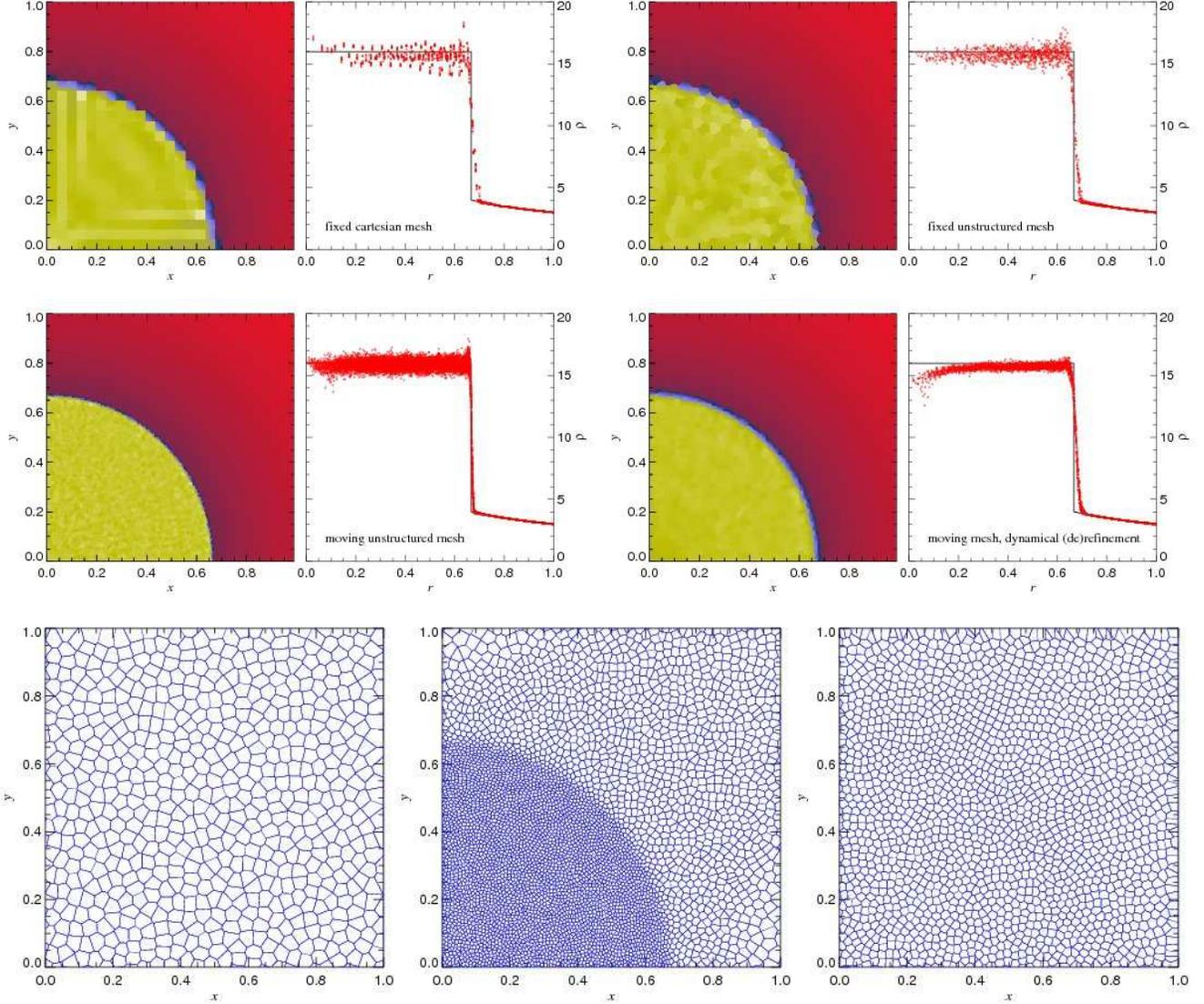
Figure 30. The Noh-problem in 2D at low resolution, calculated with four different strategies for the treatment of the mesh. The top four pairs of panels illustrate the result of the calculation at time $t = 2.0$ for each of these schemes. In each case, we show a projected density field in one quadrant of the implosion, and we give the radial density profile where we compare the densities of all mesh cells with the analytic solution. In the top left, the result for a stationary Cartesian mesh with 25^2 cells in the unit quadrant is shown. For comparison, the top right gives the result for an unstructured stationary mesh with the same number of cells. The middle left pair of panels shows the case of an unstructured moving mesh with constant mass resolution of $m_i \simeq 1/25^2$. Finally, the fourth case (middle right panels) is for a dynamically refined/derefined mesh, where cells are split if $m_i > 1.5/25^2$ or eliminated if their volume falls below $V_i < 0.25/25^2$. The bottom three panels show the mesh geometries at the final time of the three schemes where an unstructured mesh is used. From left to right: the stationary unstructured case, the moving-mesh case with constant mass resolution, and finally the dynamically refined/derefined mesh.

and apply reflective boundary conditions at the inner boundaries. However, when an unstructured mesh is used, we calculate all four quadrants in order to avoid imposing mirror symmetry along the coordinate axes. The outer boundaries are modelled with a special inflow boundary that makes use of the analytic solution known for the problem.

We begin by considering the 2D problem carried out with different strategies for treating the mesh. The simplest approach is a fixed Cartesian mesh of resolution 25×25 cells in one quadrant. Our second calculation was done with an unstructured mesh that has the same total number of cells

as in the Cartesian case, but is also kept stationary. Comparison of these two schemes allows an assessment of how well the unstructured mesh performs relative to a Cartesian mesh of equal spatial resolution. Our third calculation uses a moving unstructured mesh where the mesh cells are moved with the local velocity of the gas, such that the mass per cell stays constant to good approximation. We here use an initial mesh that has been extended to $[-3, 3] \times [-3, 3]$ in order to provide enough mesh area for the implosion problem. Finally, in our last variant of this problem we also use a moving mesh but exercise our schemes for dynamically refining

and derefining the mesh, as described in Section 6. Specifically, we split cells into two when their mass has gone up above 1.5 times the initial average mass of a cell, $\overline{m} = 1/25^2$. This automatically generates new cells in the inflow region, and maintains a constant mass resolution there. In this case we do not have to extend the mesh beyond the $[-1, 1]^2$ domain; rather, new mesh cells appear dynamically as needed. In addition, we also derefine cells (i.e. delete them) if their volume falls below 0.25 times the initial volume $\overline{V} = 1/25^2$ of the cells. This prevents the spatial resolution in the high-density region from getting better than a certain limit. In fact, it limits the maximum effective resolution per dimension to $N_{\rm eff} = 1/(0.25 \times \overline{V})^{1/2} = 50$.

In Figure 30, we compare the results of these four different mesh strategies. In each case we show a projected density field at time $t = 2.0$, and we compare the densities of individual mesh cells with the expected analytic solution for the radial density profile. In all four cases, the postshock flow shows some substantial density scatter. This is presumably a combination of weak post-shock oscillations present in our scheme, and geometrically induced asphericities. The oscillatory behaviour is particularly noticeable and coherent in the Cartesian case, where also the so-called 'carbuncle' phenomenon is at work, which can produce artefacts for very strong grid-aligned shocks. Stone et al. (2008) invoke a special cure for this problem and achieve a quiet post-shock flow in the Noh problem with the help of judiciously introduced extra dissipation. We expect that the unstructured fixed mesh should be less susceptible to such grid alignment effects. Indeed, the result for this case (top right panel of Figure 30) shows no coherent oscillations and preferred directions of the kind seen for the Cartesian grid, but it nevertheless exhibits a similar degree of noise.

Our calculation with a *moving* unstructured mesh and constant mass resolution (middle left in Figure 30) benefits from an automatically higher spatial resolution in high density regions. As a result, the position of the shock front is recovered more accurately, and the shock is nicely round. Nevertheless, this solution suffers from a similar degree of oscillatory behaviour in the post-shock region. Finally, we consider our calculation with a dynamically refined/derefined moving mesh, shown in the middle right of Figure 30. Here the shock is also recovered well, with an accuracy that is slightly better than for the fixed mesh results, thanks to slightly smaller cell sizes at the shock front. In the post-shock region, the oscillations are noticeably reduced. This is a result of the derefinement procedure that is active in this region, which tends to smooth out high frequency noise. It is in any case reassuring that our dynamical mesh refinement and derefinement schemes work robustly in this difficult hydrodynamic problem without introducing any artefacts. The suppression of the density at the origin is perhaps caused by so-called 'wall heating' (Ryder, 2000), which is commonly seen at a similar level in other calculations of the Noh problem (e.g. Liska & Wendroff, 2003; Stone et al., 2008).

The bottom three panels of Figure 30 show the mesh geometry at the final time of the three calculations that use an unstructured mesh. It is nicely seen how the constant mass-resolution case (bottom middle panel) produces a mesh that varies strongly in spatial resolution. On the other hand, the dynamically created and derefined mesh (bottom right panel) shows almost no trace of the spherical shock front,

due to the particular derefinement criterion used. Note that the latter is arbitrary, and if desired, one could for example refine the mesh only in the region of the shock, and derefine it elsewhere.

Finally, we now consider 3D calculations of the Noh problem. This represents a still more demanding test than the 2D problem due to the larger density contrast reached in the 3D case. To test many of the new features of our moving-mesh code, we carry out this test with dynamic generation of mesh cells, and dynamic derefinement in the high-density region. Specifically, a cell is created if its mass content lies above $m_i > 1.5\,\overline{m}$, and it is dissolved if its volume has dropped below $V_i < 0.05\,\overline{V}$, where $\overline{m}$ and $\overline{V}$ are the initial average mass and volume per cell. In Figure 31, we give results for two different initial resolutions, corresponding to $\sim 16.7^3$ ($\overline{m} = \overline{V} = 2.16 \times 10^{-3}$) and $\sim 50^3$ cells in the unit octant. With the above refinement/derefinement criteria, by $t = 2.0$ the effective resolution in the lower resolution calculation has grown to $N_{\rm eff} \sim 34$ at $r = 1$, and in the central high-density region, it is limited to a maximum of ~ 45.2. For the higher resolution calculation, these numbers are three times as large. We note that in the lower resolution calculation, about 812620 cells have been created, and 225209 were destroyed during the course of the calculation. For the higher resolution calculation, these numbers are a factor ~ 27 higher. In Figure 31, we see that the moving-mesh code with dynamic mesh refinement/derefinement is able to integrate this problem robustly, with satisfactory accuracy given the effective resolutions employed here, nevertheless some limited postshock oscillations are present. Also, some 'wall heating' is clearly present at the centre (Ryder, 2000; Liska & Wendroff, 2003).

8.7   Kelvin-Helmholtz instability

Fluid instabilities are among the most interesting phenomena of hydrodynamics, and they play a crucial role in mixing processes and the production of turbulence. Their importance in cosmological gas dynamics is potentially very large. For example, fluid instabilities are thought to be important for an accurate treatment of stripping of gas from satellite galaxies, and for calculating the correct level of turbulence and entropy expected in the intracluster gas of clusters of galaxies. Recently, numerical inaccuracies of SPH in the treatment of fluid instabilities across contact discontinuities with large density jumps have caused concern about the scheme's ability to adequately treat such problems (Agertz et al., 2007). Fixes have been proposed for this issue (Price, 2008; Wadsley et al., 2008), but it is not clear yet whether they can be applied successfully in general calculations without introducing inaccuracies in other regimes.

On the other hand, it is not obvious that Eulerian methods provide superior accuracy for fluid instabilities in all regimes, even though this is often assumed by advocates of these schemes. One can certainly expect that problems due to the Galilean non-invariance of Eulerian codes could be a source of concern here. In this subsection we will examine these issues with the important example of the Kelvin-Helmholtz (KH) instability. This occurs across contact discontinuities in the presence of a tangential shear flow.

For simplicity, we first consider a simple shear-flow in two dimensions, where we strongly excite a single mode by
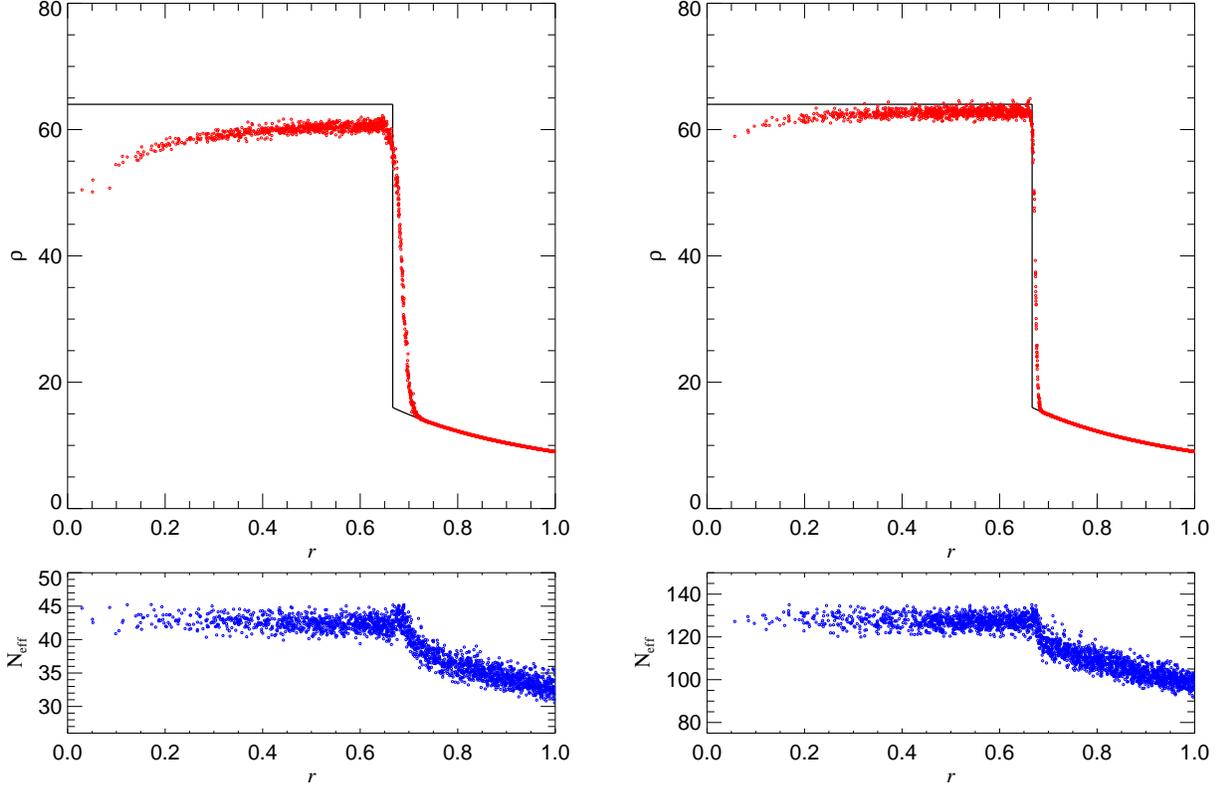
Figure 31. The Noh-problem in 3D at two different effective resolutions, calculated with dynamical mesh creation and mesh derefinement. The panels on the left are for a low-resolution calculation, where cells are created at the edge of the box such that the mass resolution does not drop below $1.5 \times \overline{m}$, with $\overline{m} = 2.16 \times 10^{-3}$, and cells in the high-density region are eliminated if their volume drops below $V_i < 0.05\overline{V}$, with $\overline{V} = 2.16 \times 10^{-3}$. The high-resolution calculation on the right hand side has 27 times better mass and volume resolution. In both cases, the bottom panels give the effective resolution per dimension for the cells as a function of radius, defined as $N_{\mathrm{eff}}^i = 1/V_i^{1/3}$, where V_i is the volume of a cell. Only a random subset of 2000 of the cells is shown in each panel.

imposing a suitable velocity perturbation. In a periodic domain of unit length on a side, with principal coordinate range $[0, 1]^2$, we set-up gas with density $\rho = 2$ in the central horizontal strip described by $|y - 0.5| < 0.25$, and give it velocity $v_x = 0.5$ to the right, whereas the rest of the box is filled with gas of density $\rho = 1$ that moves to the left with speed $v_x = -0.5$. The pressure is set to $P = 2.5$ everywhere, with $\gamma = 5/3$. There are hence two contact discontinuities along which KH instability can develop.

To make sure that initially a single mode will dominate the linear growth of the instability, we excite a single mode with a wave-length equal to half the box size by perturbing the v_y velocity field according to

$$v_y(x, y) = w_0 \sin(4\pi x) \times \qquad (124)$$
$$\left\{ \exp\left[-\frac{(y - 0.25)^2}{2\sigma^2} \right] + \exp\left[-\frac{(y - 0.75)^2}{2\sigma^2} \right] \right\}$$

with $w_0 = 0.1$ and $\sigma = 0.05/\sqrt{2}$. The two exponential damping factors restrict the perturbation to the region close to the two interfaces. The details of how this perturbation is imparted are relatively unimportant for the test.

We first carry out a test at low resolution, using 50×50 cells that are initially arranged as a Cartesian mesh. This allows us to visualize the motion of the mesh as a function of time when our moving-mesh approach is used. This is

illustrated in the time-sequence shown in the top four panels of Figure 32[§], which includes an overlay of the Voronoi mesh. We see that the moving-mesh approach develops well-defined KH-billows and is able to maintain a relatively sharply defined boundary between the two fluids, with only a small amount of mixing between them. Also, the moving mesh approach has no problem coping with the strong shear present in this simulation. This has traditionally been a significant challenge for Lagrangian hydrodynamics codes.

In the bottom two panels of Figure 32 we show the final result at $t = 2.0$ obtained for the same initial conditions when the mesh is kept fixed instead, in one case calculated with our own code, in the other with ATHENA. Reassuringly, the two codes give nearly indistinguishable solutions when a fixed mesh is used. This confirms that our code AREPO is comparable in accuracy to state-of-the-art second order accurate Eulerian codes when run with a fixed mesh. The two fixed-mesh calculations of Figure 32 can also be compared to the moving-mesh result shown in the top four panels. Clearly, the results are qualitatively similar, but there is substantially more mixing in the fixed-mesh calculations,

---

[§] A video of this simulation as well as other videos of our example calculations may be found at http://www.mpa-garching.mpg.de/~volker/arepo
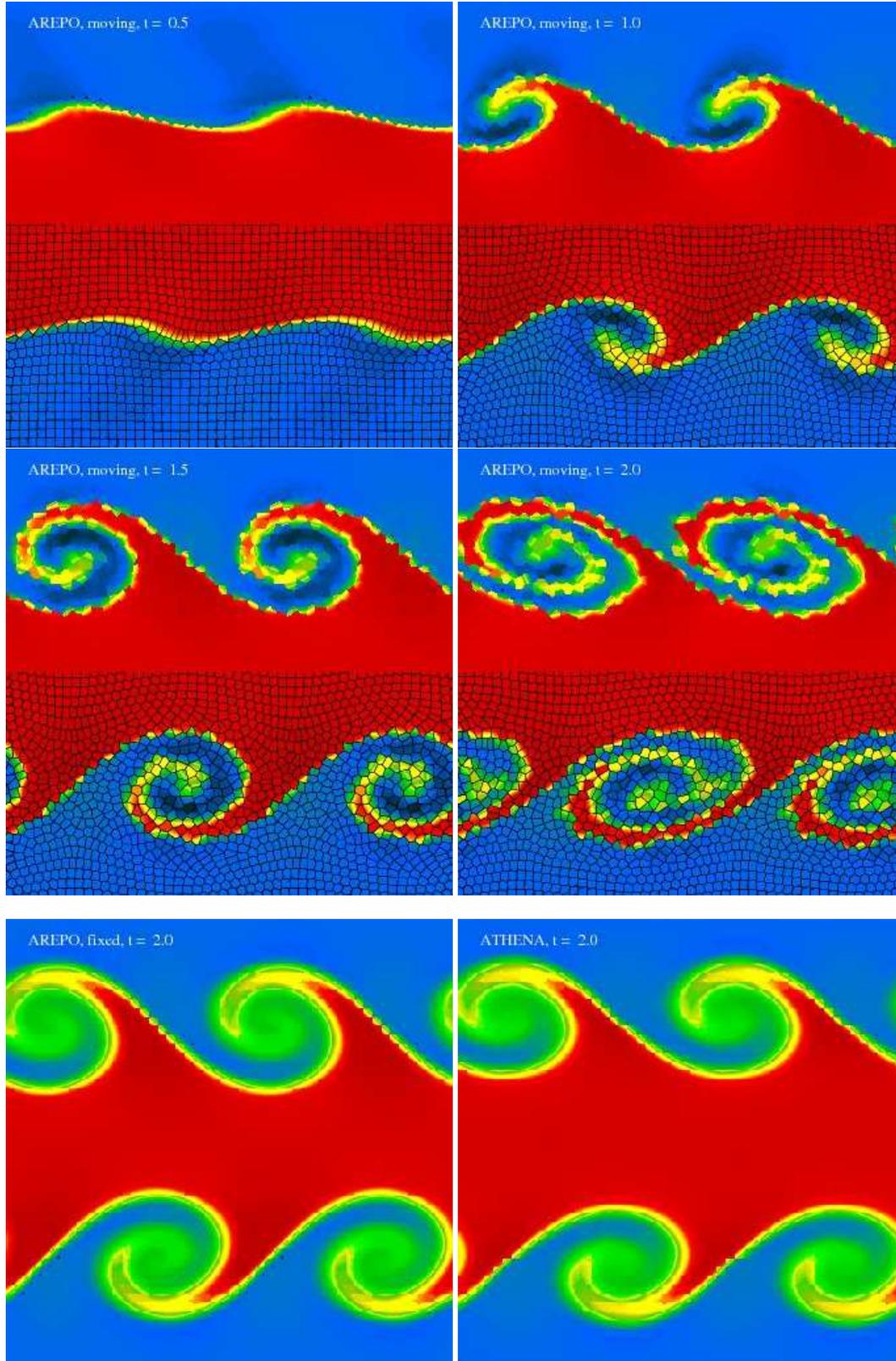
Figure 32. The top four panels show the time evolution of the Kelvin Helmholtz instability in a low resolution (50×50) test calculation with the moving-mesh method. Each panel gives the density field (at times $t = 0.5$, 1.0, 1.5 and 2.0), with the Voronoi mesh overlaid in black in the lower half of the box. For comparison, the lower two panels show the results for the same initial conditions, but this time computed keeping the initial Cartesian mesh fixed. The panel on the bottom left shows the result at time $t = 2.0$ obtained with our code AREPO for a fixed mesh, while the bottom right gives the result of ATHENA (with second order reconstruction and the Roe solver). The latter two results are nearly identical. Note however that in the non-linear regime the KH instability appears to evolve somewhat faster for the moving-mesh code compared with the fixed grid.
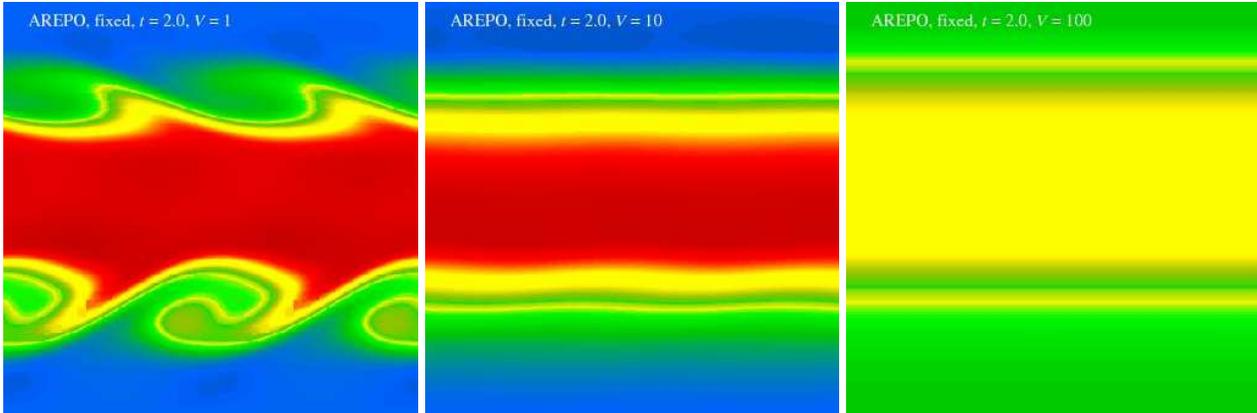
Figure 33. Kelvin Helmholtz instability test at time $t = 2.0$, computed with AREPO with a fixed mesh. In the three cases, different boost velocities along both the x- and y- directions have been applied. The fact that the results do not agree (and in particular not with the $V = 0$ result shown in the bottom of Figure 32) is direct evidence for a violation of Galilean invariance of the Eulerian approach. We note that we have obtained nearly identical results for this test when it is carried out with ATHENA instead of our code AREPO.
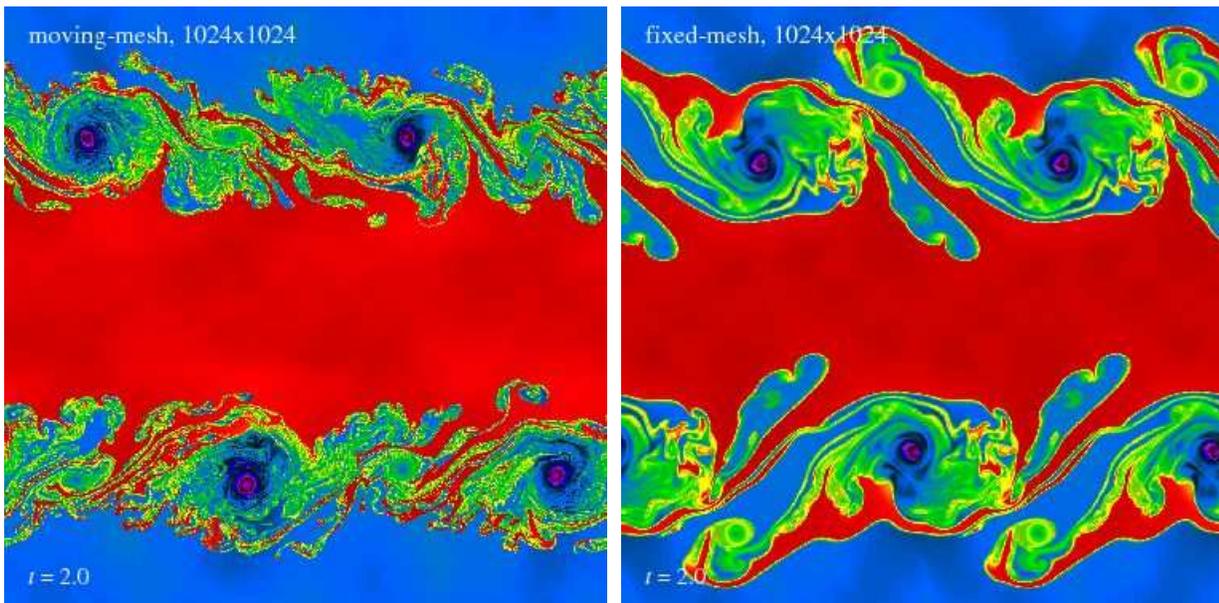
Figure 34. Kelvin Helmholtz instability test at high resolution, using a 1024×1024 initial mesh. We compare results obtained with the moving-mesh approach (left panel) to those on a fixed grid (right panel), at time $t = 2.0$. Quite strikingly, small-scale features of the flow are preserved in the moving mesh code with much less mixing, albeit at the price of earlier generation of asymmetries in the flow.

which wash out the KH-billows to nearly constant density at this resolution. While this effect is expected to become smaller with increasing resolution, the effective numerical diffusivity of the Eulerian calculation is clearly much higher than that of the moving mesh approach, a finding that is also expected based on the advection tests of a contact discontinuity carried out at the beginning of this section. There is also a further important difference between the moving-mesh and the fixed-mesh results. In the non-linear regime, the KH instability appears to evolve somewhat faster for the moving-mesh approach than for the fixed mesh. In fact, the fixed-mesh result at $t = 2.0$ is more similar to the $t = 1.5$ moving-mesh output than to its $t = 2.0$ output.

We next consider the ability of the schemes to cope with

additional bulk fluid motion, or in other words, with a transformation into a boosted frame of reference. To this end we simply add a constant velocity vector to all cells of the initial conditions, and we shall again compare the results at time $t = 2.0$. The physics does not change due to such a Galilean boost, and we should therefore get the same results. We have already seen that this is not in general the case for Eulerian codes. Here we test how strong the resulting effects are in practice. In Figure 33, we show what AREPO returns for velocities equal to $v = 1$, 10, or 100, imposed both in the x- and y-directions, *if the mesh is kept fixed*. Thanks to the periodic boundary conditions, the system will have returned at time $t = 2.0$ again to the its original position, after the code had to advect it one or several times through the box. In
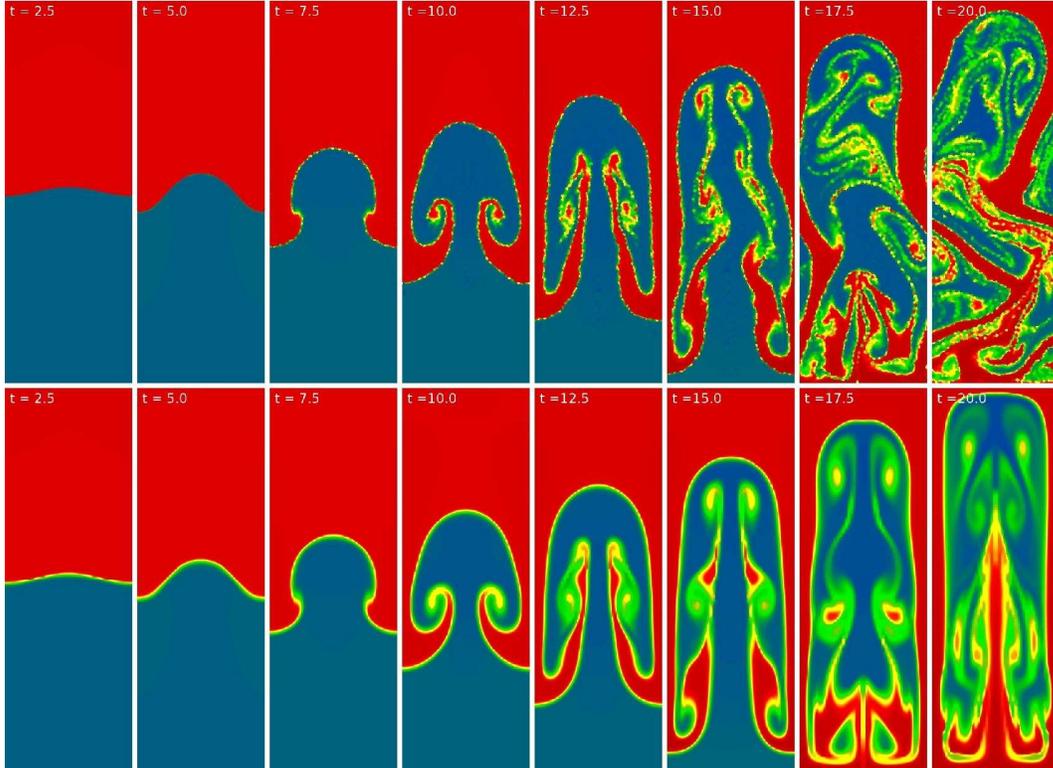
Figure 35. Time evolution of a Rayleigh-Taylor instability in simulations with a moving (top) and a static (bottom) mesh. The resolution is quite low, only 48×144 cells have been used for this test.

principal, all three results should therefore be identical. But the actual results are very different; in this Eulerian mode, the code's result and hence the error in the calculation is a strong function of the magnitude of the bulk velocity relative to the rest-frame of the calculation. Especially when these velocities become supersonic, the calculated solution can become qualitatively and quantitatively inaccurate. For the somewhat brutal test of $v = 100$, the calculated solution is completely dominated by advection errors, with the density field in the box becoming almost homogeneous. We have also evolved the same initial conditions with the ATHENA code, finding very similar results. We expect this behaviour to be generic for Eulerian codes. The accuracy with which fluid instabilities are calculated across contact discontinuities quickly deteriorates if the contact discontinuity moves. In contrast, when we run the same initial conditions with the *moving mesh* of AREPO, we recover the same results in all three cases, and they are identical to the $v = 0$ result shown in Figure 32.

Is this a serious problem for Eulerian codes? This very much depends on the problem that is studied. In many applications, an individual system is studied and one can freely choose a convenient reference frame for the calculation. One will then pick one in which velocities relative to the calculational frame are small. The issue of Galilean non-invariance may then not be of great concern. However, we argue that this is not the case for cosmological simulations, where multiple objects are simulated at the same time, many of them moving with large velocities compared to their sound speed. In this case, the accuracy of the cal-

culation correlates strongly with the bulk velocity of the galaxies, a rather worrying effect.

However, Galilean non-invariance may not be the only problem that troubles the Eulerian approach when the Kelvin-Helmholtz instability is considered. We have found that in an Eulerian calculation of this problem at high resolution, multiple secondary KH billows are spawned in the early evolution due to grid irregularities. On the other hand, the moving-mesh method appears less susceptible to this problem, thanks to its ability to advect the mesh with the contact discontinuity. Some of these grid-induced features can even affect the long-term evolution of the instability. In Figure 34, we compare fixed and moving-mesh versions of the same KH instability test at a resolution of 1024^2. The moving-mesh preserves much more fine detail in the flow. This is because contact discontinuities between different phases can be advected with large speeds without being necessarily mixed. We think this is a very interesting difference, which makes the moving-mesh code particularly attractive for the study of multi-phase media.

8.8 Rayleigh-Taylor instability

Another important type of fluid instability arises in stratified atmospheres in approximate hydrostatic equilibrium if a denser fluid lies above a lighter phase. In such a Rayleigh-Taylor (RT) unstable state, energy can be gained if the lighter fluid rises in the gravitational field, triggering buoyancy-driven fluid motions.

We consider a simple test in 2D where we excite a sin-
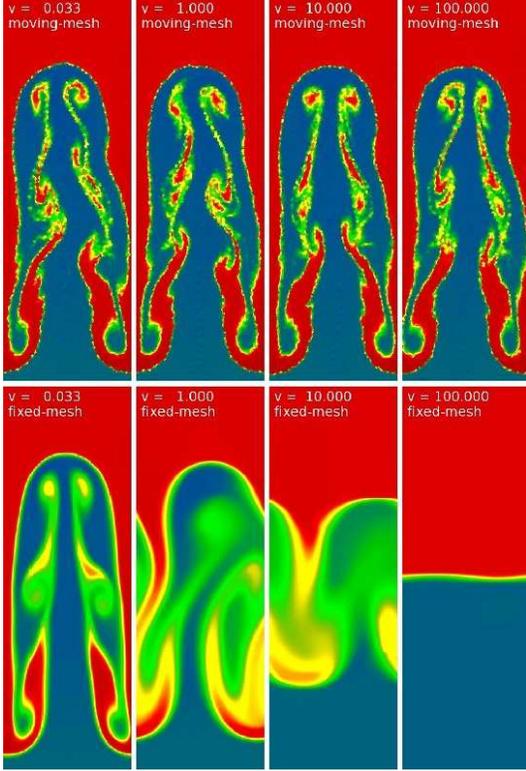
Figure 36. Rayleigh-Taylor instability calculated with different Galilean boosts v_x in the horizontal direction (the simulation domain is periodic in the x direction). The correct result should in principal be independent of v. The top row shows the result at time $t = 15.0$ computed with our moving-mesh approach, while the bottom row of panels gives the corresponding results for a fixed-mesh calculation with AREPO.

Figure 37. Kinetic energy in our Rayleigh-Taylor test calculations as a function of time. For the boosted simulations, the kinetic energy was defined by first subtracting the horizontal boost from the v_x velocity component. The black solid lines show the moving-mesh calculations, for velocity boosts $v_x = 0$, $v_x = 1$ and $v_x = 10$ (the thickness of the lines decreases in this sequence). The dashed lines give the results for fixed-mesh calculation with our code, for the same three velocities, from top to bottom. Finally, for comparison, the dotted line gives the result obtained with ATHENA for $v_x = 0$.

gle Rayleigh-Taylor mode for clarity. Our setup is a small variation of a similar test considered in Liska & Wendroff (2003), and also similar to a test described in Jim Stone's test suite of ATHENA. The computational domain is chosen as $x \in [0, 0.5]$ and $y \in [0, 1.5]$, with periodic boundary conditions at the x-boundaries, and reflecting walls at the top and bottom of the domain. The density is $\rho = 2$ in the top half of the domain, and $\rho = 1$ in the bottom half. The pressure in the vertical midplane is $P_0 = 2.5$ (with $\gamma = 1.4$) and varies vertically as $P(y) = P_0 + g\,(y - 0.75)\rho$, where $g = -0.1$ is an imposed external gravitational field. This ensures an initial hydrostatic equilibrium. The initial velocities are zero everywhere, except for a small perturbation that is designed to excite a single mode for the Rayleigh-Taylor instability. We adopt for this perturbation

$$v_y(x,y) = w_0 \left[1 - \cos(4\pi x)\right]\left[1 - \cos(4\pi y/3)\right], \qquad (125)$$

where $w_0 = 0.0025$. For the tests discussed in the following, we deliberately use a comparatively low resolution of 48×144 cells.

In Figure 35, we first compare the time evolution of the system between a calculation carried out with a static Cartesian mesh, and one with our new moving-mesh approach. Clearly, the evolution is rather similar during the early linear growth of the perturbation. However, the moving-mesh approach is able to maintain a sharper contact discontinuity, as

expected. Eventually, the evolution starts to differ markedly once the dynamics becomes very non-linear. The moving-mesh solution loses vertical symmetry and starts to develop turbulence. In contrast, the fixed mesh calculation is able to maintain perfect symmetry for a longer time, but it shows much stronger mixing than the moving-mesh calculation, which also damps the fluid motion. In both cases, the loss of symmetry is caused by small round-off errors, but in the moving mesh approach their growth in the transverse direction is faster and less benign. This is due to a kind of bending instability in the mesh. When the mesh is compressed strongly in one direction, it automatically means that the cells develop a large aspect ratio, which can only be relaxed (in the sense that the cells become rounder again) through some transverse motions. It turns out that the mesh likes to respond to transverse perturbations in this situation; they tend to grow quickly, and numerical round-off is sufficient to trigger this. This also means that the moving mesh can itself be a source of unwanted perturbations, but they only really become relevant in poorly resolved flows, where the shape of an individual cell directly matters. This is similar to the Kelvin-Helmholtz problem on a Cartesian mesh, where at high resolution small-wavelength secondary billows are triggered by perturbations originating at the mesh corners. If the Rayleigh-Taylor problem is simulated with higher resolution and with resolved (i.e. softened) phase boundaries, symmetry is maintained much longer in the moving-mesh approach.

We have also used this Rayleigh-Taylor test to investigate once more the question of Galilean invariance. To this end we have added a constant velocity v_x to the initial state.

As the system is periodic in the x-direction, the evolution should in principle not change if viewed in the rest-frame of the moving fluid. In Figure 36, we show a comparison of the resulting fluid state when either a moving mesh or a fixed mesh is used in our code AREPO. We carry out this comparison for horizontal flow velocities of $v_x = 0.033$, $v_x = 1$, $v_x = 10$, and $v_x = 100$. It is seen that the Eulerian result changes significantly along this sequence. The horizontal motion leads to a damping of the growth rate of the instability, additional mixing, and also to a loss of symmetry. In fact, for a sufficiently large velocity boost, the instability is suppressed entirely. We note that in this case the Eulerian calculations also become much more expensive, as their Courant condition becomes limited by the bulk velocity. The moving-mesh calculation does not suffer from this problem, and it produces a Galilean-invariant solution as expected. However, the way the symmetry is lost in the calculation tends to vary, as this is determined by small numerical noise in the mesh motion.

In Figure 37 we show the kinetic energy in the simulations as a function of time. The thick dashed line and the dotted line show the results for a fixed mesh with no velocity boost, comparing our code AREPO with ATHENA (the latter using the Roe solver and second-order accurate reconstruction). The results of the two codes for the evolution of the kinetic energy agree qualitatively very well, showing first a maximum, followed by a rapid decline to a nearly constant level that then declines over a much longer timescale. This is produced by the initially very symmetric evolution of the RT instability when a Cartesian mesh is used, and the subsequent transition to turbulent motions at later times. The symmetry is broken when a velocity boost is applied in the Eulerian calculations, and even a velocity as small as $v_x = 0.033$ is sufficient for that. The other two dashed lines of Fig. 37 show the evolution of the kinetic energy (relative to the rest frame of the gas) when a boost of $v_x = 1$ or $v_x = 10$ has been applied, respectively. Now the pronounced maximum is gone, and for increasingly larger boost velocities the plateau of the kinetic energy becomes ever smaller. For the moving mesh case on the other hand, the results are insensitive to the velocity boost. This is shown by the three solid lines, which give the kinetic energy for $v_x = 0$, $v_x = 1$ and $v_x = 10$, respectively. These Lagrangian calculations also do not produce the strong maximum seen in the $v_x = 0$ case for the Eulerian code, which we interpret as effectively being an artefact of the grid symmetry, because the higher asymmetries in the numerical round-off errors present in the moving-mesh approach are sufficient to break the symmetry in the evolution early on.

8.9   Moving boundaries

As briefly discussed earlier, the moving mesh approach can also be quite easily adapted to describe curved boundaries of essentially arbitrary shape, and if desired, these boundaries can also move in complex ways. While this feature is probably not helpful in most astrophysical problems, it has potentially very useful applications in other areas, for example aerodynamics. We here discuss a simple example to illustrate this possibility.

In Figure 38, we show how a special curved boundary can be constructed in terms of two parallel strings of
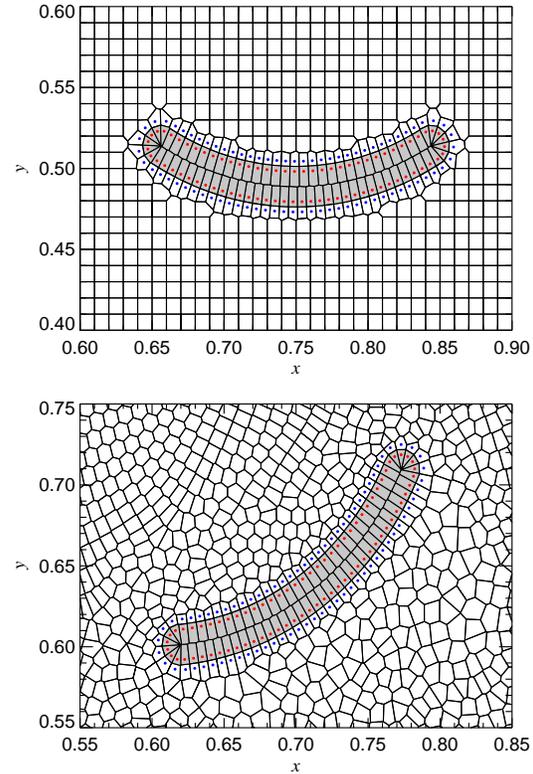

Figure 38. Example of a reflective curved boundary condition, realized with two adjacent strings of 60 mesh-generating points (top panel). The blue points are on the fluid side, while the red points are 'outside'. The Voronoi faces between these points are given reflective boundary conditions, while the rest of the mesh is treated in a regular fashion. In the bottom panel, we show the mesh geometry at a slightly later time, when the special points have moved as a solid body on a prescribed path, while the rest of the mesh and the surrounding fluid have reacted to this motion.

mesh-generating points that have an equal distance from either side of the desired contour. In our example, we want to model a solid obstacle, where the red points are meant to be inside the obstacle, and the blue points are outside, i.e. on the side of the fluid. The Voronoi faces between the points will be modelled with reflecting boundaries by the code, and represent the surface of the solid body. Unlike the other mesh-generating points that define the mesh, the red and blue points are only moved together, as a rigid body. We can now impose a motion for our solid object, and the fluid will always be forced to flow around it. In our chosen example, we will move the object with constant velocity according to a prescribed path, with the fluid being initially at rest. This means we will effectively stir the fluid with the object, much like moving a spoon in a coffee cup, except that our "coffee cup" is two-dimensional here. The lower panel of Figure 38 shows the mesh geometry around the object after it has moved by a small amount. It is nicely seen that the points that model the curved boundary condition have moved together as a rigid body, while the background mesh reacted to this motion by starting to flow around the object.

In Figure 39 we show the time evolution of a test problem calculated with such a moving boundary. The back-
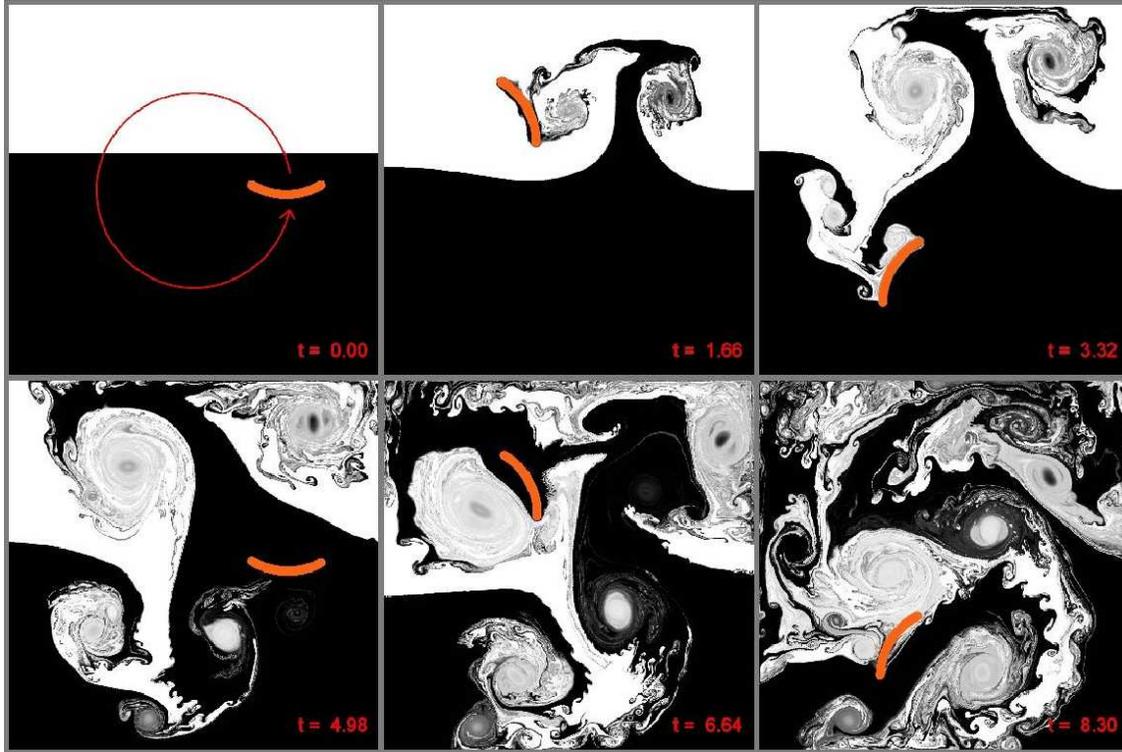
Figure 39. Time evolution of the mixing of two fluids induced by the motion of a solid object. This test illustrates the ability of AREPO to cope with arbitrarily curved, moving boundary conditions. As illustrated, the orange 'spoon' is moved on a circular path, through a two-phase gaseous medium that is initially at rest. The mixing is shown in terms of a tracer dye that is advected with the flow, and which was given an initial value of 1 (white) in the lower-density top phase, and a value of 0 (black) in the higher-density lower phase. Each frame shows the value of the dye in grey-scale, at different times as labeled. The square domain was initially populated with a 768×768 mesh-generating points on a Cartesian grid, and has reflective boundary conditions at the outer walls.

ground fluid is represented with 768×768 points, and the solid object with 600 particles. The domain $[0, 1] \times [0.1]$ is modelled with reflecting boundaries on the outside. The upper half for $y > 0.6$ is filled with gas of density $\rho = 0.5$, the lower with gas at unit density $\rho = 1$. The pressure is $P = 1$ everywhere, with $\gamma = 5/3$. Our solid object is rotated around the centre in counter-clockwise direction with an angular velocity $\omega = 2\pi/5$. In this particular example we are especially interested in the mixing of the two phases of the initial configuration. To this end we give each phase a 'dye', a conserved tracer variable. This is followed as a passive conserved scalar along with the ordinary fluid variables by the code. In Figure 39, we show the value of this dye as function of time, with the solid body displayed in orange.

It is nicely seen how the motion of the object induces complex gas motions, including the generation of vorticity and turbulence. This eventually leads to a complete mixing of the two phases, but for a long time partially mixed regions survive. Thanks to the motion of the mesh with the flow, contact discontinuities between the two media can be advected almost without numerical errors, allowing the foliated structure of partially mixed fluid to remain intact even while moving. Such a low level of numerical diffusivity would be very difficult to achieve with an Eulerian treatment.

9 TEST PROBLEMS WITH SELF-GRAVITY

As the long discussion in Section 5 made clear, an accurate treatment of self-gravity in finite volume codes is actually a surprisingly subtle and tricky problem, more so than in SPH. In this section we will first discuss a three-dimensional gravitational collapse problem of a cold gaseous sphere, which is a good test for energy conservation in the presence of a strong virialization shock, a scenario that is of direct relevance for cosmological simulations. We then examine the collapse of Zeldovich pancakes as a basic test of the cosmological integration in AREPO. We finally turn to two example applications of our new code, a colliding galaxy problem and the 'Santa Barbara cluster'. Both of these problems are primarily meant to illustrate that the AREPO code introduced here is fully functional and suitable for science applications in computational cosmology.

9.1 Evrard's collapse test

Evrard (1988) has introduced an interesting collapse problem that has been frequently used in the literature to test SPH simulation codes (e.g. Hernquist & Katz, 1989; Dave et al., 1997; Springel et al., 2001; Wadsley et al., 2004), but results for mesh codes have been rarely reported. The initial conditions consist of a sphere of gas with mass $M = 1$ and radius $R = 1$, with an initial density profile of the form

$$\rho(r) = \begin{cases} M/(2\pi R^2 r) & \text{for } r \leq R \\ 0 & \text{for } r > R. \end{cases} \qquad (126)$$

The gas with adiabatic index $\gamma = 5/3$ is initially at rest and has thermal energy $u = 0.05$ per unit mass, which is negligible compared with the gravitational binding energy (assuming $G = 1$).

In the beginning of the evolution, the gas is freely falling towards the origin under self-gravity. Eventually, it bounces back in the centre, with a strong shock propagating outwards through the still infalling outer parts of the gas sphere. The system then virializes and settles to a spherical distribution in hydrostatic virial equilibrium. The time evolution of the system is hence characterized by a conversion of gravitational potential energy first to kinetic energy, and then to heat energy. As such, it tests a situation that is prototypical for gravitationally driven structure growth, and also provides a sensitive test of the ability of a code to conserve the total energy accurately in self-gravitating gaseous systems.

In Figure 40, we show radial profiles of density, velocity, and entropic function $A = P/\rho^\gamma$ at time $t = 0.8$, when the strong shock has formed. We compare simulations carried out with different calculational schemes, but all with the same number of 24464 resolution elements in the initial radius of the sphere. The top three rows give results calculated with our mesh-code AREPO. In the first case, we consider a fixed Cartesian mesh, which we expect to be challenged by the large dynamic range of this problem. In the second and third row we use a radially stretched mesh as initial conditions, which has equal mass per cell initially. This mesh is much better adjusted to the radial symmetry of the system, and the increase of density towards the origin. The simulation shown in the second row keeps this unstructured mesh fixed throughout the evolution, while in the third row the full moving-mesh approach is applied, where the mesh-generating points are moved with the local flow velocity. Finally, in the bottom row, an alternative Lagrangian result is shown, this time based on SPH, using the 'entropy-formulation' of Springel & Hernquist (2002) as implemented in GADGET-2 (Springel, 2005).

Among these calculations, the least accurate result is clearly produced by the fixed Cartesian mesh, which offers the poorest spatial resolution in the central regions of the sphere, as a result of its lack of adaptivity. The stretched fixed grid already gives much better results, but the central density distribution is still significantly underestimated. However, if the mesh is allowed to move, a significantly improved solution is obtained, even though here also the limited spatial resolution produces a shock front that is radially too far advanced compared to the expected solution for close to infinite resolution. The latter is shown as a solid line and was produced by a one-dimensional PPM calculation kindly provided by Steinmetz & Müller (1993). We note that the SPH result shown in the bottom row also produces the main features quite well, but its shock is significantly broader than in the moving mesh calculation, and there is also substantial pre-shock entropy production in the infall region ahead of the shock, as a result of the artificial viscosity that becomes active in converging parts of the flow.

The timing offset in the shock location appears to be a result of the low resolution used in this test, as this vanishes for better resolution. To illustrate this point, we show in Figure 41 an equivalent plot for a high-resolution simulation of the same problem using 1.56×10^6 mesh-generating points, arranged in a stretched mesh that is here kept fixed during the evolution (the moving mesh gives an essentially indistinguishable result). The result reveals an excellent agreement with the high-accuracy one-dimensional calculation.

Finally, we consider the conservation of total energy in this problem, as this is not readily guaranteed in the finite volume approach with self-gravity. In Figure 42, we show the time evolution of the thermal, kinetic, and potential energy, for simulations of the Evrard collapse carried out with different numerical resolutions and different strategies to couple the gravitational field to the hyperbolic Euler equations. In the left panel, results for the "standard" approach to treating self-gravity, discussed in subsection 5.2 are shown. We can see that there are substantial errors in the total energy, which amount to a relative error as large as $\sim 50\%$ for the poorest resolution considered here, where 24464 cells are inside the initial radius of the sphere. With better spatial resolution, the size of the error progressively shrinks. However, it cannot be made smaller by improving the time integration as it is ultimately caused by *spatial* discretization errors. The cell-centred mass fluxes used to estimate the gravitational work on a cell are not accurately balancing the amount of energy actually extracted from the gravitational field when the strong virialization shock propagates outwards. As a result, a substantial energy error is produced, which, in this example corresponds to a gain of energy of the whole system. Clearly, the energy error from this can become quite severe, especially for poor resolution, so the first generation of cosmic structures could be quite strongly affected by this problem.

However, rewriting the gravitational work term in terms of a surface integral, as described in subsection 5.4, leads to much better energy conservation. This is shown in the right-hand panel of Fig. 42, where the same simulations are shown but this time using our improved coupling of self-gravity to the Euler equations. We see that in this case the relative error in the total energy stays well below 10^{-3} and does not show any systematic resolution dependence, which is a dramatic improvement relative to the results above. For these results, the gravitational work-term was calculated with the gravitational potentials, as described in equation (96). If the simpler formulation of equation (94) is used instead, the maximum relative errors become considerably larger (up to 10^{-2} in the peak) but are still acceptable. All the simulations shown in Fig. 42 were calculated for an unstructured stretched mesh that was kept fixed; if the mesh is allowed to move instead, the errors tend to be slightly smaller.

Lastly, we would like to examine whether the softening correction factors discussed in subsection 5.5 make a significant difference for the energy conservation. First, note that such a difference is really only expected if the gravitational interaction between two neighbouring points is affected by the softening kernel. In other words, the quantities η_j defined in equation (103) are only different from zero if the gravitational softening lengths are large enough so that some 'overlap' with neighbouring cells occurs at least in a fraction of the cells. This can be guaranteed by choosing a sufficiently large value for the softening constant f_h, for example $f_h = 2.5$. In simulations of the Evrard collapse with this setting, we find a maximum energy error of the same
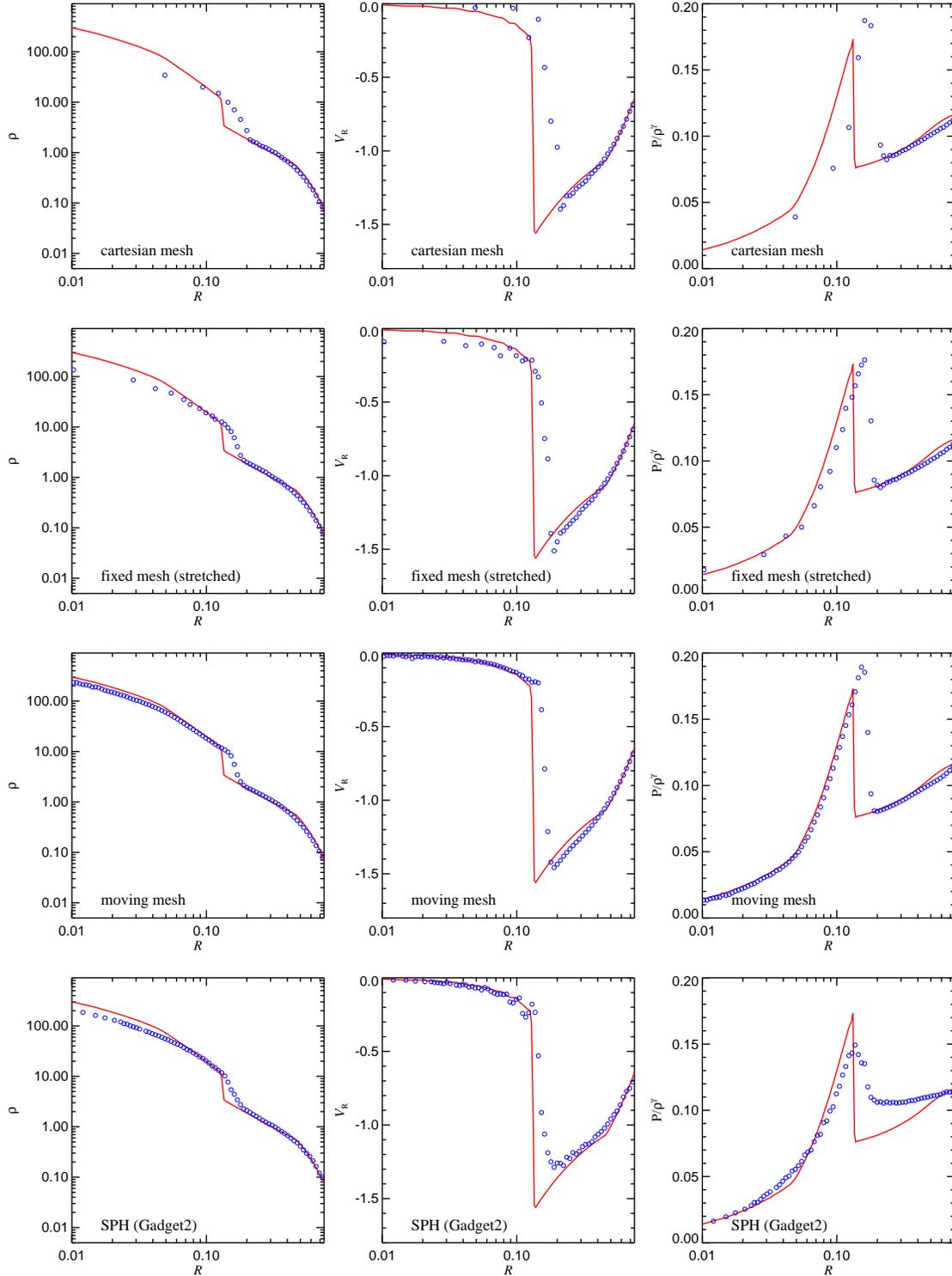
Figure 40. Shock profiles in the 'Evrard-collapse' problem, carried out with different simulation techniques. In all cases, the same number of resolution elements inside the initial radius $R = 1$ of the gas cloud has been used. The top panel gives the result at $t = 0.8$ for a fixed Cartesian grid. The second row shows the result for AREPO when the mesh-generating points are arranged as a stretched grid of points such that the mass per cell is constant for the *initial $\rho \propto 1/r$* profile, but the mesh was kept static in this case. This is different in the third row; here the mesh was allowed to move with the flow, and in addition the mesh-shaping scheme based on the 'inverse Zeldovich' approach was enabled. Finally, the bottom row gives the equivalent result obtained with the same particle number using SPH, as implemented in the GADGET-2 code. The red solid line is a one-dimensional PPM result obtained by Steinmetz & Müller (1993).
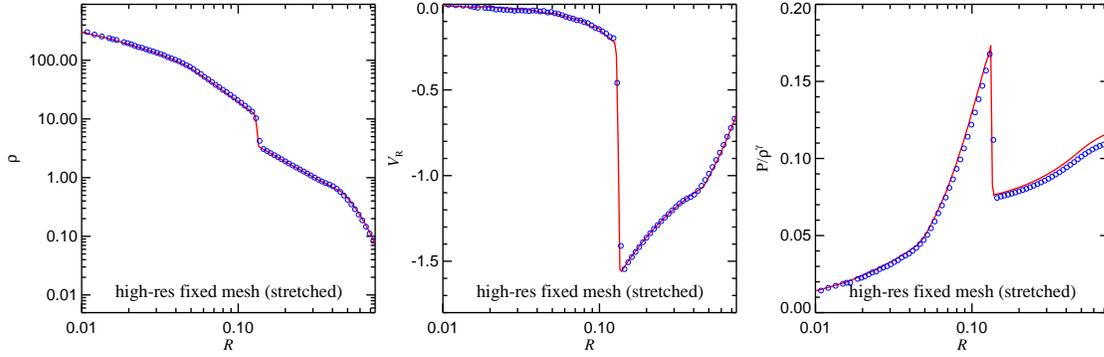
Figure 41. High resolution result (symbols) for the Evrard collapse problem calculated with AREPO, using 1.56×10^6 resolution elements in the initial gas sphere of radius $R = 1$. An analytic solution for this problem is unavailable, but the solid gives the results of a one-dimensional high-resolution PPM calculation kindly provided to us by Steinmetz & Müller (1993) which should be fairly close.
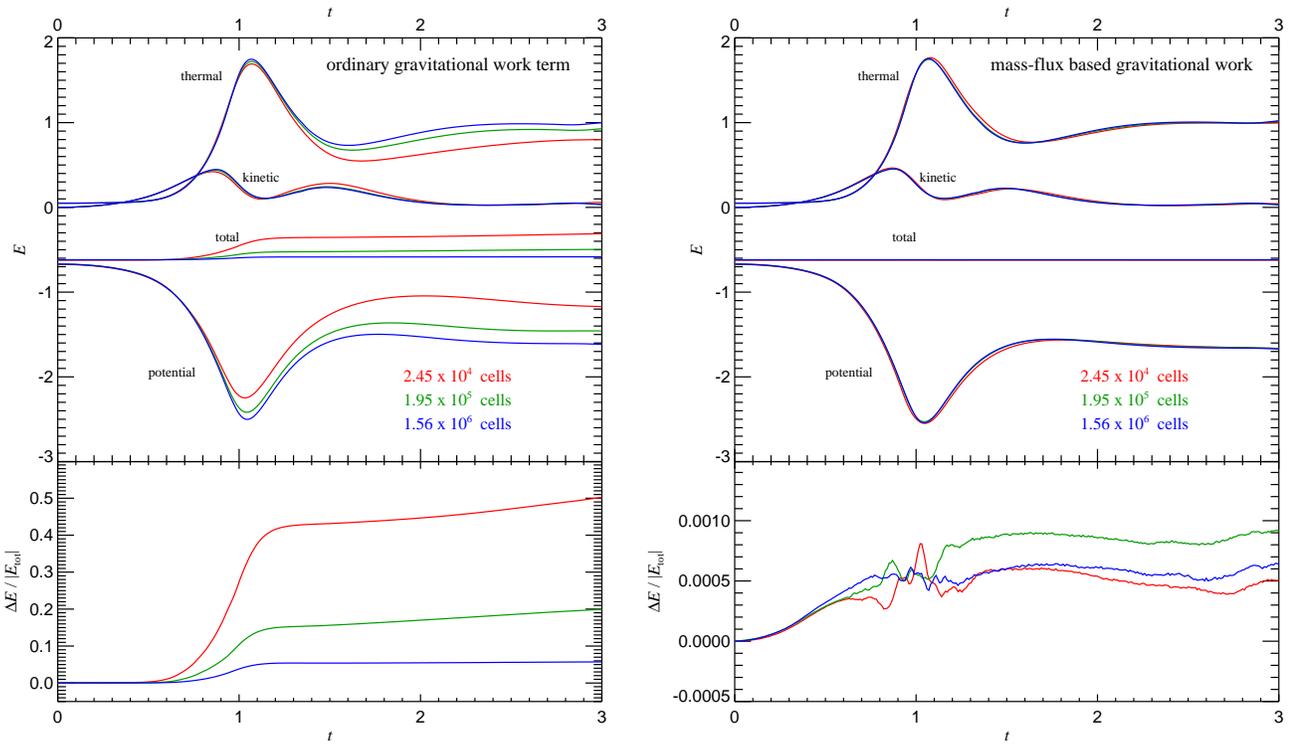
Figure 42. Energy evolution in the 'Evrard-collapse' problem, calculated for different numerical resolutions and different calculational schemes to couple self-gravity to the Euler equations. In the panel on the left, results for a standard approach to treat self-gravity are shown. Here the gravitational work on a cell is estimated with cell-centred mass fluxes. This can however produce substantial errors in the presence of strong shock waves, especially when the spatial resolution is quite coarse. The plot on the right gives results for the same simulations, except that the gravitational work term is estimated based on the mass-fluxes determined by the Riemann solver at the surfaces of cells. This leads to a quite accurate conservation of the total energy of the system.

size as above, i.e. it stays below 10^{-3}. However, if we disable in the code the corrective force of equation (107) that accounts for changes of the softening lengths, the energy error goes up by more than a factor of 10, and reaches slightly more than 1% in the peak. This shows that this correction factor should indeed be included for high-precision results.

9.2 Zeldovich pancake

A useful standard test for cosmological codes is the evolution of a sinusoidal density perturbation in an expanding Einstein-de-Sitter universe. After an initial linear growth phase, the one-dimensional wave collapses to a Zeldovich pancake, involving a pair of very strong shocks. As this problem can be viewed as a 'single-mode' of the general cosmolog-
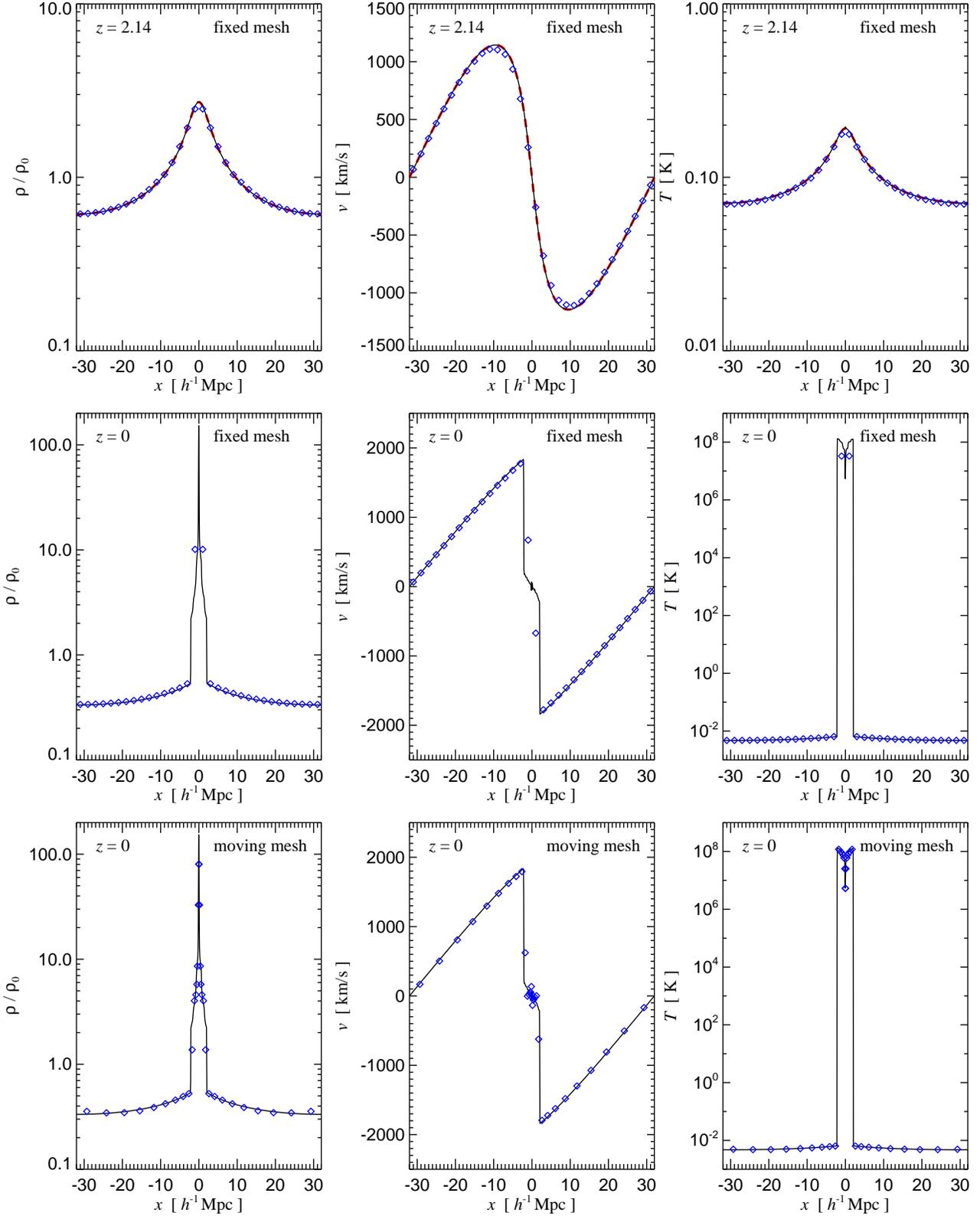
Figure 43. Zeldovich pancake test at two different times, and for two different ways to move the mesh. The top row of panels shows the pancake at $z = 2.14$ when it is still in the linear regime, before the collapse occurs at $z_c = 1$. We show the analytic solution as a thick dashed line in red, while a high-resolution calculation with 1024 cells is shown as a solid line and the blue symbols give a low-resolution result with 32 fixed cells, for comparison. The middle and bottom rows of panels give the state of the pancake at $z = 0$, well into the non-linear regime, once calculated with a fixed mesh and once with the moving mesh approach. Again, we compare with a high-resolution result based on 1024 fixed cells (solid line). Note in particular that the temperature in the unshocked parts of the flow is very accurate, thanks to the energy-entropy formalism that is applied by the code in very cold parts of the flow.

ical structure formation problem, it is a particularly useful test of any cosmological code. Furthermore, it is also a useful test-bed for the dual entropy-energy treatment described in subsection 3.5, as the initial gas temperature is negligibly small and drops further through the cosmic expansion.

The comoving position x corresponding to an initial unperturbed coordinate q at redshift z is given by (Zeldovich, 1970)

$$x(q,z) = q - \frac{1+z_c}{1+z} \frac{\sin(kq)}{k}, \tag{127}$$

where $k = 2\pi/\lambda$ is the wavenumber of the perturbation of wavelength λ. The comoving density corresponding to the displacement is given by

$$\rho(x,z) = \frac{\rho_0}{1 - \frac{1+z_c}{1+z}\cos(kq)}, \tag{128}$$

and the peculiar velocity is

$$v_{\text{pec}}(x,z) = -H_0 \frac{1+z_c}{(1+z)^{1/2}} \frac{\sin(kq)}{k}. \tag{129}$$

Here ρ_0 are the background density (equal to the critical density), and H_0 is the Hubble constant today. These equations describe the solution exactly up to the redshift z_c of collapse.

We follow Bryan et al. (1995) and Trac & Pen (2004), and choose $\lambda = 64\,h^{-1}\text{Mpc}$ and $z_c = 1$. Our test simulations are started at $z_i = 100$, with an initial gas temperature of $T_i = 100\,\text{K}$. As the pressure forces are negligible up to the formation of the pancake, the temperature should evolve adiabatically as

$$T(x,z) = T_i \left[\left(\frac{1+z}{1+z_i}\right)^3 \frac{\rho(x,z)}{\rho_0} \right]^{2/3} \tag{130}$$

until collapse. We carry out tests of the Zeldovich problem both using a moving mesh and a fixed mesh. This in particular serves as a useful test of the correct implementation of the cosmological time integration, and the coupling of the gasdynamics to self-gravity in an expanding background space. As our code AREPO has presently no one-dimensional gravity solver, we carry out the tests in two dimensions instead, and for simplicity, we use only the PM solver in two dimensions with a sufficiently large mesh.

In Figure 43, we show the density, velocity and temperature profiles of the Zeldovich pancake at two different times, briefly before collapse at redshift $z = 2.14$, and well into the non-linear evolution of the pancake at $z = 0$. In all panels, a high resolution result (based on 1024 fixed points per dimension) is shown with solid lines, and symbols of a low resolution calculation with initially 32 points per dimension are overlaid. In the high redshift result shown in the top panel, we also include the analytic solution of Zeldovich in terms of a thick-dashed line. Before the collapse of the pancake at $z = 1$, both the fixed mesh and the moving mesh calculation trace the analytic result with comparable accuracy, we therefore only show one of the results. In the middle row of panels, the fixed-mesh result at $z = 0$ is shown. Outside of the shock-fronts, the solution is still very accurate, but the lack of resolution inside the collapsed region leads to a poor representation of the structure of the pancake, even though its characteristic values of density and temperature are reasonably well reproduced. The moving mesh calcula-

tion shown in the lower row of panels does significantly better in this respect. Remarkably, even though only 32 points were available initially, the density- and temperature structure of the pancake, as well as the location of the two strong shocks, are represented very accurately.

Note that the temperature evolution in this Zeldovich pancake test is particularly difficult to get right, as there is a very large dynamic range between the initially cold gas and the shocked heated gas in the pancake, amounting to a difference of ~ 10 orders of magnitude. Before the gas is heated by the shocks, the flow is extremely cold and dominated by gravitational forces, meaning that the problems discussed in subsection 3.5 with respect to spurious heating of very cold flows in finite volume methods are bound to be present in this Zeldovich pancake test. Indeed, in the results shown in Figure 43 we have applied the entropy-energy scheme described in subsection 3.5. The ordinary treatment based on the total energy alone invariably leads to significant heating of the gas well outside of the shock-front prior to the collapse of the pancake. While this does not alter the motion of the gas (the resulting pressure forces remain way too small), the temperature evolution of the gas becomes inaccurate, especially when the resolution is comparatively low. However, with the entropy scheme, a very accurate solution is recovered in a robust way. We note that especially with respect to the temperature evolution, our results also compare favourably to those of Trac & Pen (2004) obtained with their moving-frame formalism. They also show much sharper shock fronts than obtained with SPH (Dave et al., 1997).

9.3   The Santa Barbara cluster

In the 'Santa Barbara Cluster Comparison Project' (Frenk et al., 1999) a large number of cosmological hydrodynamic codes were applied to the same initial conditions, set-up to produce a rich cluster of galaxies in an Einstein-de-Sitter universe. The inter-comparison of the results produced by a this set of different codes, which included both SPH and Eulerian AMR methods, allowed an assessment of the systematic uncertainties in such cosmological structure formation simulations. While a fair amount of scatter between the different results was found, there was still quite reasonable agreement in most of the cluster bulk properties (such as total mass, temperature, etc.), and in the radial cluster profiles (such as the radial run of density, baryon fraction, etc.), with typical code-to-code scatter of order 10%. The same initial conditions have also been regularly used as hydrodynamic code test in subsequent work (e.g. Wadsley et al., 2004; Springel, 2005; Thacker & Couchman, 2006).

It seems likely that the scatter in the results for the Santa Barbara cluster would be smaller if the experiment was repeated today with the most recent versions of the most commonly employed cosmological codes, thanks to the progress made in the numerical simulation techniques in recent years. However, at the same time there is little indication that arguably the most important systematic difference found by Frenk et al. (1999) between the Lagrangian SPH and the Eulerian AMR codes, namely the systematic difference in the entropy predicted for the central cluster gas, has gone away. This entropy was found to be lower in SPH than in the AMR calculations, which in turn also affects the
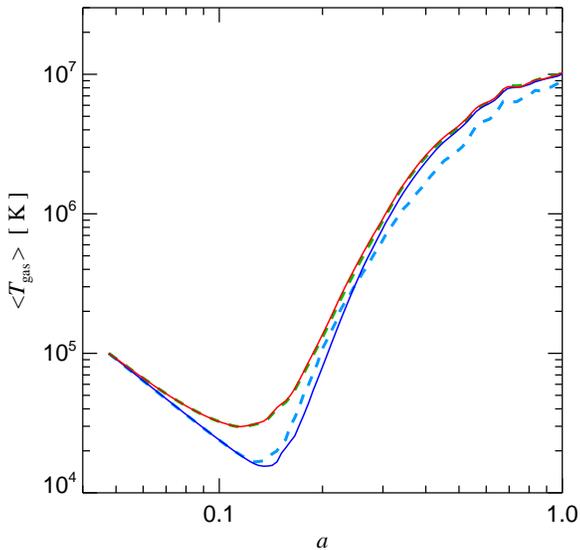
Figure 44. Evolution of the mean mass-weighted temperature in four low-resolution calculations (2×32^3) of the Santa Barbara cluster. The dashed green line shows the result of the moving-mesh approach when the ordinary total energy approach is applied. Here the gravitationally dominated cold flows at high redshift are clearly subject to some spurious heating. The red solid line shows the result when our entropy-energy scheme is used with a Mach-number threshold $\mathcal{M}_{\rm thresh} = 1.1$, which turns out to be ineffective in preventing the high redshift heating, as the Mach numbers responsible for it are very high. If we instead use our alternative scheme for deciding when to preserve the entropy (with $\alpha_S = 0.05$) we obtain the blue solid line, where now the heating in very cold, low-density gas is suppressed and the expected adiabatic decline of the mean temperature at high redshift is obtained. For comparison, the dashed lines gives an SPH result obtained with GADGET-2 at the same resolution.

temperature and gas density profiles in the inner parts of the cluster. This also has an impact on cluster cooling rates if radiative cooling is allowed, and on important observables such as the emitted X-ray luminosity.

In SPH, entropy is accurately conserved (Springel & Hernquist, 2002; Ascasibar et al., 2003), but it could be artificially low due to the absence of entropy production through mixing and to SPH's tendency to spuriously suppress fluid instabilities. On the other hand, the Eulerian codes may overestimate the central entropy as a result of numerical diffusivity and overmixing. Also, they are more prone to suffer from heating caused by the noisy gravitational field produced by the collisionless matter. Recently, the idea that the difference may ultimately arise from differences in the treatment of mixing has found some support in numerical experiments (Mitchell et al., 2009). Presently, it remains however unclear what the correct entropy profile for the Santa Barbara profile really is, even though this is an important question for numerical cosmology. Note that due to the absence of radiative cooling in this problem, the Santa Barbara cluster represents comparatively clean and 'easy' physics. If even this case cannot be calculated fully reliably, it is clear that the more demanding simulations that also account for radiative cooling are fraught with numerical uncertainties.

We here give first results for the Santa Barbara Cluster with our new moving mesh code, calculated at comparatively low resolution. All our simulations follow the original initial conditions in a periodic box of side-length $32 \, h^{-1}{\rm Mpc}$, using homogeneous sampling of the dark matter component, and an equal number of mesh-generating points as dark matter particles. The simulations are started at redshift $z = 50$, and use cosmological parameters of a critical density cosmology with dark matter content $\Omega_{\rm dm} = 0.9$, baryonic density $\Omega_b = 0.1$, and Hubble constant $H_0 = 100 \, h \, {\rm km \, s^{-1} Mpc^{-1}}$ with $h = 0.5$.

In Figure 44, we first show the evolution of the mean mass-weighted temperature of the whole simulation box, from the starting redshift to the present time. Initially, no structures have formed yet, so that the mean mass-weighted temperature should decline as $T \propto a^{-2}$ for a while. Eventually, the thermal energy content in the shock-heated gas of the first forming cosmic structures starts to dominate and the mean temperature begins to rise rapidly. This general evolution is reflected in the four simulation results depicted in Figure 44, albeit with interesting differences in detail. The green dashed line shows the result of the moving-mesh approach when the ordinary total energy approach is applied. The red line gives the result when the energy-entropy formalism is used with a Mach number threshold $\mathcal{M}_{\rm thresh} = 1.1$, while the solid blue line uses our alternative switch for deciding whether the entropy should be kept instead of updating it with the total energy equation. In the latter case, the entropy is used if the thermal energy is at most a small fraction $\alpha_S = 0.05$ of the local kinetic energy. This proves effective to yield the expected adiabatic decline of the mean temperature at high redshift. On the other hand, the Mach-number based switch does not make a difference in this regime, as the shock waves responsible for this high-z heating are typically quite strong. However, it can still effectively act against noise-induced heating in virialized structures at lower redshift. For comparison, the dashed light blue line gives an SPH result obtained with GADGET-2 at the same resolution. It yields a high-redshift evolution very similar to the moving-mesh code when the entropy scheme is used for the cold gas, but at low redshifts its gas ends up being noticeably colder on average. A substantial part of this difference in the final temperature is probably simply caused by the lower effective resolution of SPH, which tends to reduce the heating through shocks. Higher resolution SPH calculations yield a mean temperature that is 5-8% higher, quite close to the mesh based result.

Radial profiles of mean gas density, gas entropy, gas temperature and dark matter density of the final Santa Barbara cluster are given in Figure 45. We show results for the different numerical resolutions of 32^3, 64^3, and 128^3 with solid circles, in different colours as labelled. All these simulations use the entropy-energy formalism with a threshold Mach number $\mathcal{M}_{\rm thresh} = 1.1$ in order to suppress spurious heating from the noise in the gravitational field induced by the dark matter. The thermodynamic profiles converge reasonably well, but not nearly as well as the dark matter density. Interestingly, the central cluster entropy is actually quite close to the SPH result that is shown for comparison, but the innermost entropy profile shows a shallower slope that produces a temperature profile that keeps slowly rising to the very centre. If the total energy equation is applied
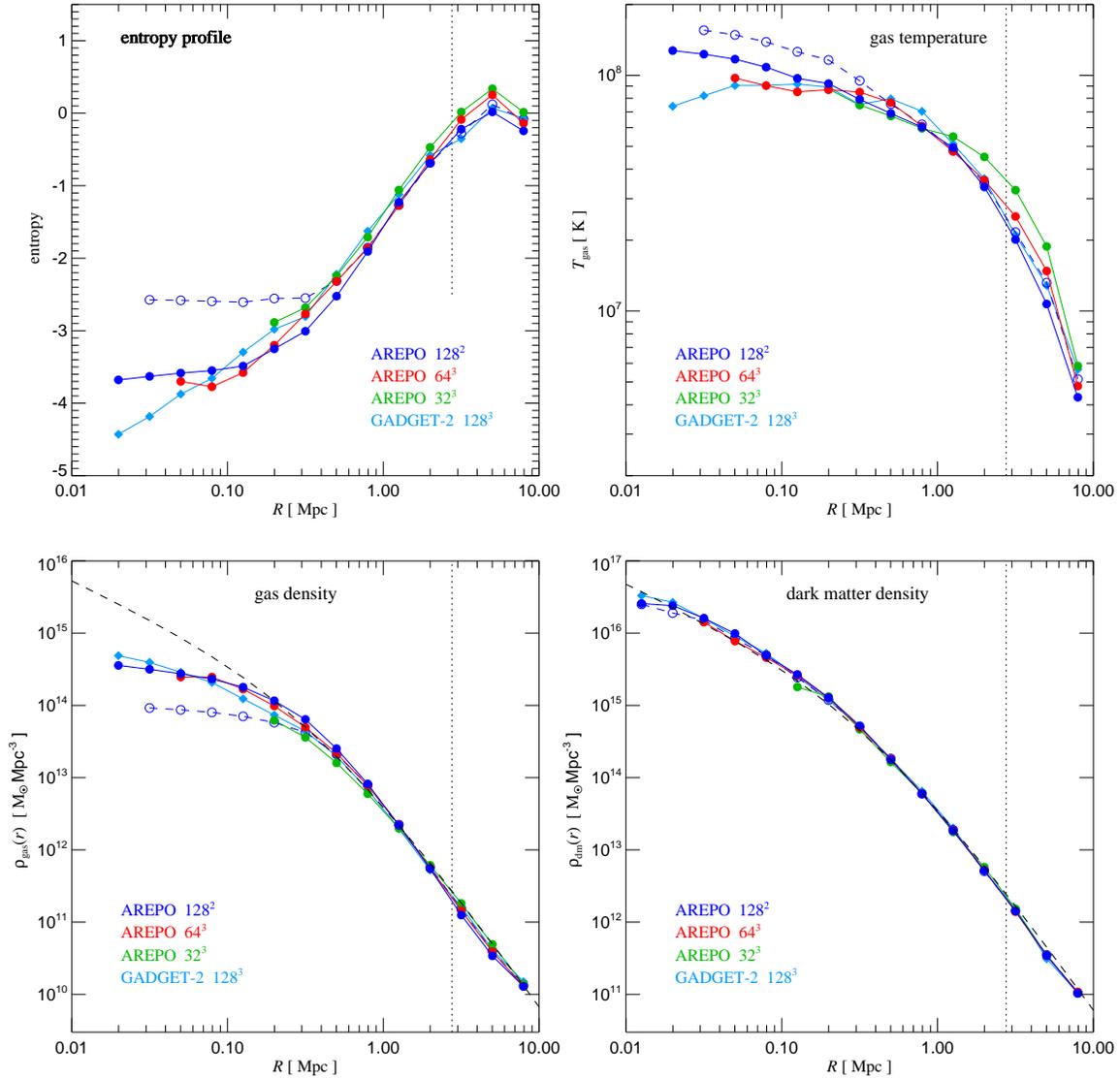
Figure 45. Radial profiles of the gas entropy (top left), gas temperature (top right), gas density (bottom left) and dark matter density (bottom right) of the Santa Barbara cluster, calculated with different resolutions and with different calculational methods. For our moving-mesh approach, results for the three resolutions 2×32^3, 2×64^3 and 2×128^3 are shown with solid circles. Here we applied our entropy-energy scheme with a Mach number threshold $\mathcal{M}_{\mathrm{thresh}} = 1.1$. The open circles show the result for the 2×128^3 run when only the total energy equation is used, and the gravitational work term is estimated based on the actual mass fluxes. However, the results at this high resolution show no difference when the gravitational work term is estimated with cell-centred fluxes instead. Finally, a high-resolution result obtained with the SPH code GADGET-2 is shown with diamonds. The vertical dotted lines mark the virial radius of the cluster ($R_{\mathrm{vir}} = 2.754\,\mathrm{Mpc}$), while for comparison the dashed line in the top left panel illustrates the shape of the dark matter density distribution in terms of the best-fit NFW profile (with concentration $c = 7.5$), scaled by the gas to dark matter mass ratio.

throughout the calculation in the 128^3 run, we obtain the result shown with hollow circles. It produces much higher core entropy and central gas temperature, as well as a lowered central gas density, when compared with our default mesh-based calculation. We think these results clearly show that the origin of the discrepancy found first in Frenk et al. (1999) between the central cluster entropy in SPH and AMR codes is caused by dissipation in extremely weak shocks and the production of mixing entropy in effectively smooth parts of the flow. Part of this dissipation is clearly artificial and caused by gravitational N-body noise, which has much more

drastic consequence in mesh-based calculations than in SPH. It therefore appears clear that mesh-based results that use the energy equation alone will overestimate the central entropy. Unfortunately, it is less clear how much suppression of dissipation is warranted, and where hence the true entropy level ultimately lies. This will be investigated further in future work.

We note that the dark matter density profiles found with AREPO converge very well, and are consistent with the ones found with GADGET-2. Also, we have found that at high resolution (64^3 and 128^3) it makes essentially no
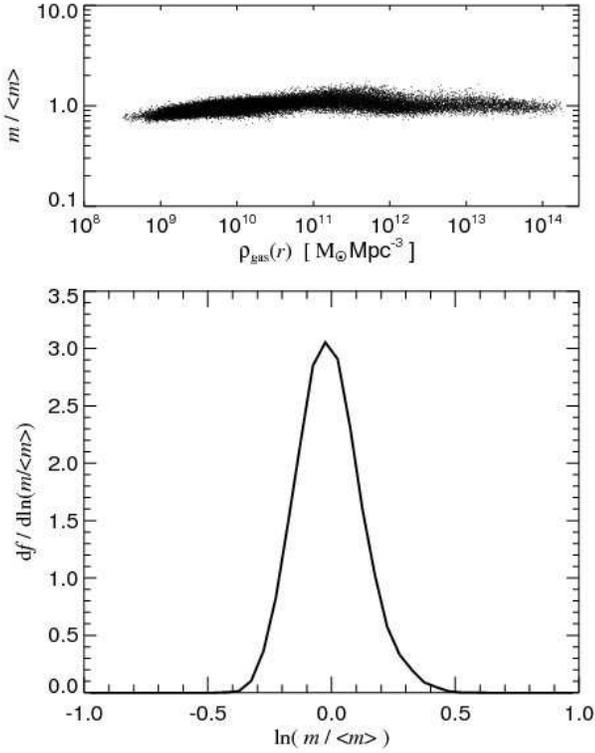
Figure 46. Scatter plot of the mass per cell as a function of local gas density (top panel). The mass is here expressed in units of the mean mass per cell, $\langle m \rangle$, and the measurement was made at $z = 0$ for our 2×32^3 run of the Santa Barbara cluster. The bottom panel shows the distribution function of $m / \langle m \rangle$, which has roughly log-normal shape.

difference to the results whether the 'standard' approach to treat the gravitational work term is employed, or our alternative scheme based on the actual mass fluxes at the surfaces of cells. Only at the low resolution of 32^3 we have found that the cell-centred approach gives slightly higher central cluster entropy and temperature.

It is also interesting to examine the final state of the Santa Barbara run with respect to statistical properties of the geometry of its Voronoi mesh. For example, we would like to know whether the calculation was able to maintain roughly constant mass per mesh-cell, and whether the final mesh consists mostly of 'roundish' cells, as desired. The first of these questions is addressed by Figure 46, where we show in the top panel a scatter plot of the gas mass per cell as a function of gas density. It is seen that roughly constant mass per cell has been maintained over a dynamic range of $\sim 10^5$ in density (and hence also in volume). The distribution function of the mass per cell is shown in the bottom panel of Figure 46. It has roughly log-normal shape, with a typical scatter of $\sim 20\%$. This small scatter is the direct result of our mesh-steering algorithm discussed in subsection 4.2.

In Figure 47, we show various statistics of the geometry of the final mesh at $z = 0$ in our 2×32^3 run of the Santa Barbara cluster. The top panel histograms the number of faces per cell and compares it to the same statistic for a Poisson distribution with the same number of points. The average number of faces is 14.6 per cell, meaning that on av-
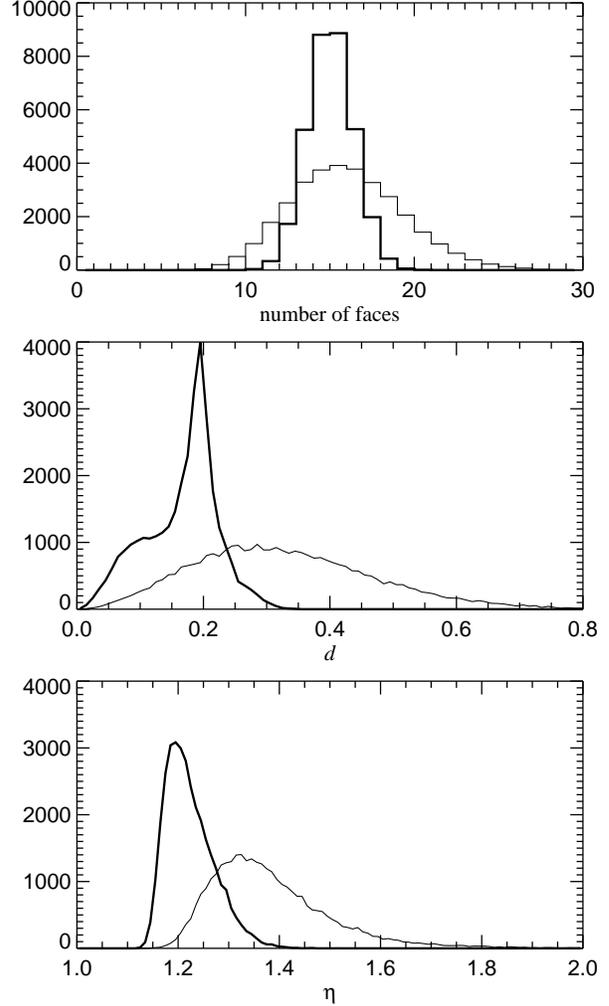

Figure 47. Geometry statistics of the final mesh at $z = 0$ in our moving-mesh calculation of the Santa Barbara cluster. The histogram in the top panel (thick line) counts the number of faces per cell; the average number is 14.6. The thin line is the same statistic for a Poisson sample (~ 15.5 faces per cell on average). The middle panel gives the distribution function of the distance d of mesh-generating points to their cell's centre-of-masses, in units of the cell radius. Again, we compare the cosmological simulation (thick line) to a Poisson sample (thin line). Finally, the bottom panel gives the distribution of the ratio $\eta = S^{3/2}/(6\sqrt{\pi} V)$ of the surface areas of cells to their volumes.

erage we need to calculate 7.3 Riemann problems per mesh-generating point. For a structured Cartesian mesh, a factor 2.43 fewer Riemann problems per cell need to be solved. The middle panel gives the distribution function of the distance d of a mesh-generating point to the centre-of-mass of its cell, in units of the fiducial radius $R = (3V/4\pi)^{1/3}$ of each cell. This quantity was used in our method to ensure reasonably roundish cells, as described in subsection 4.1. The parameter χ was set to $\chi = 0.2$, meaning that the algorithm tries to make cells with $d > 0.2$ rounder, something that clearly has worked well. Finally, another statistic that shows that our final mesh is significantly more regular than a Poisson mesh is given in the bottom panel. Here we show the distribution function of the ratio $\eta = S^{3/2}/(6\sqrt{\pi} V)$ of surface area S of

a cell to its volume V. For a sphere, $\eta = 1$ is reached, and cells with high aspect ratios will produce larger values. For our mesh, η peaks around ~ 1.2.

Finally, it is of interest to comment on the overall code speed of AREPO for such a real-world cosmological problem in comparison to an equivalent SPH simulation. In our present implementation, AREPO is a factor 1.6 slower than GADGET-3 (an updated version of GADGET-2, Springel, 2005) for the Santa Barbara cluster, using the same number of dark matter particles and cells/particles. This was measured for runs on 4 processors, for the 2×32^3 initial conditions. A full timestep of the moving mesh hydrodynamics takes about ~ 2.8 times as much CPU-time as the SPH calculations, and this cost is dominated by the mesh-construction, which weighs in with twice the cost of the SPH calculations, whereas the calculations for the finite-volume hydrodynamics itself (gradient estimation, flux estimation with Riemann solver, etc.) is slightly faster than SPH, as this requires no neighbour searches. However, the calculation of self-gravity is costly in high force-accuracy cosmological codes, and in fact makes up nearly two thirds of the cost in the GADGET-3 calculation. This cost stays roughly equal in AREPO, as expected, such that only a rather modest increase of the overall run-time in the new code remains. This additional CPU-time is well invested in our view, given that the new method yields a substantial improvement in accuracy. Furthermore, we note that so far comparatively little effort has been spent on optimizing the speed of AREPO, whereas GADGET-3 has been developed and tuned over many years. There is hence certainly room for substantial further performance improvements of AREPO in the future.

9.4   A galaxy collision simulation

The hierarchical bottom-up formation of structure from small building blocks is the leading theory of galaxy formation (White & Rees, 1978). In this scenario, galaxies frequently collide and merge to form bigger systems. In fact, according to the 'merger hypothesis' (Toomre & Toomre, 1972) galaxy collisions are a primary means to form large elliptical galaxies out of disk systems, and are hence one of the main drivers of the morphological evolution of galaxies.

Major mergers of spiral galaxies are observed in many spectacular systems in the local Universe. They have also been extensively studied with N-body and N-body/SPH simulations, leading to important insights for the nature of starbursts, the formation of spheroidal galaxies, and the secular evolution of galaxies (e.g Gerhard, 1981; Negroponte & White, 1983; Hernquist, 1989; Barnes & Hernquist, 1992; Mihos & Hernquist, 1996; Athanassoula & Misiriotis, 2002). In recent times, galaxy merger calculations were also used to study the growth of supermassive black holes at the centres of galaxies, and their energy feedback on the host systems (Di Matteo et al., 2005; Springel et al., 2005). This has led to important theoretical insights for the co-evolution of galaxies and supermassive black holes (Hopkins et al., 2006), and for the characterization of merger remnants and elliptical galaxies as two-component systems (Hopkins et al., 2008).

Interestingly, essentially all of the work thus far on isolated galaxy mergers has been carried out with the Lagrangian SPH technique. Not without reason. SPH can effortlessly deal with the large bulk velocities present in the colliding galaxies before they coalesce, and the large dynamic range in density and spatial scales that need to be resolved. At the same time, the resolution automatically follows the mass, and is concentrated where it is needed most, which in these calculations is naturally at the centres of the galaxies. Achieving this same set of features with AMR is technically and numerically substantially more challenging. This is certainly one of the primary reasons why this method has so far not been widely applied to this very important type of cosmological simulation. An added difficulty in the high-speed collisions of galaxies is that there is no convenient frame of reference where both galaxies are simultaneously at rest. In particular, the calculational hot spots where the AMR refinements are most needed are quickly moving, which invokes the problems of Galilean non-invariance inherent in the Eulerian approach. While a successful application of AMR techniques to galaxy mergers should certainly be possible in principle, AMR does not appear particularly well matched to the nature of the problem.

In this last subsection, we show that our new moving-mesh code can deal quite well with the particular challenges posed by simulations of pairs of colliding galaxies. We here focus on the technical aspects of carrying out such simulations with AREPO and give an illustrative example, deferring a scientific analysis of the results of moving mesh based galaxy mergers to future work.

We begin by briefly discussing the creation of appropriate initial conditions. SPH can easily deal with vacuum boundary conditions, and it is hence straightforward to represent isolated gaseous disks in otherwise empty space. In contrast, our moving-mesh code always requires a well defined total volume that is tessellated by the mesh. We therefore enclose the isolated galaxies with a large box that comfortably contains all the material of the galaxies and their tidal debris. The outer walls of this box have reflective boundary conditions for the gas, but collisionless particles are allowed to penetrate freely. Also, the calculation of gravity is not influenced by the presence of the box. Next, we need some sort of background grid to fill all of this empty space through which galaxies with their cells and gas can move. Ideally, we would like to be able to add this background grid automatically to existing initial conditions of SPH calculations, such that equivalent moving-mesh initial conditions result. This allows continued use of the same initial conditions codes and facilitates easy comparison of the results. We have implemented the following functionality in AREPO to produce appropriate initial conditions that fulfill these requirements:

(i) Starting with a set of gas particles from an existing SPH initial conditions, we first generate a new set of points for tessellating the whole volume of the simulation box. We want this set of points to produce cells of constant volume far away from the galaxy (or galaxies), but close to the original gas distribution, there should be cells of smaller size such that the original gas distribution stays well localized when the Voronoi mesh is constructed. We want to avoid that particles at the surface of the original SPH particle distribution end up having Voronoi cells that extend far out into empty space, which would cause a low-density leakage of the mass. We generate an appropriate set of additional points via a special Barnes & Hut (1986) oct-tree construc-
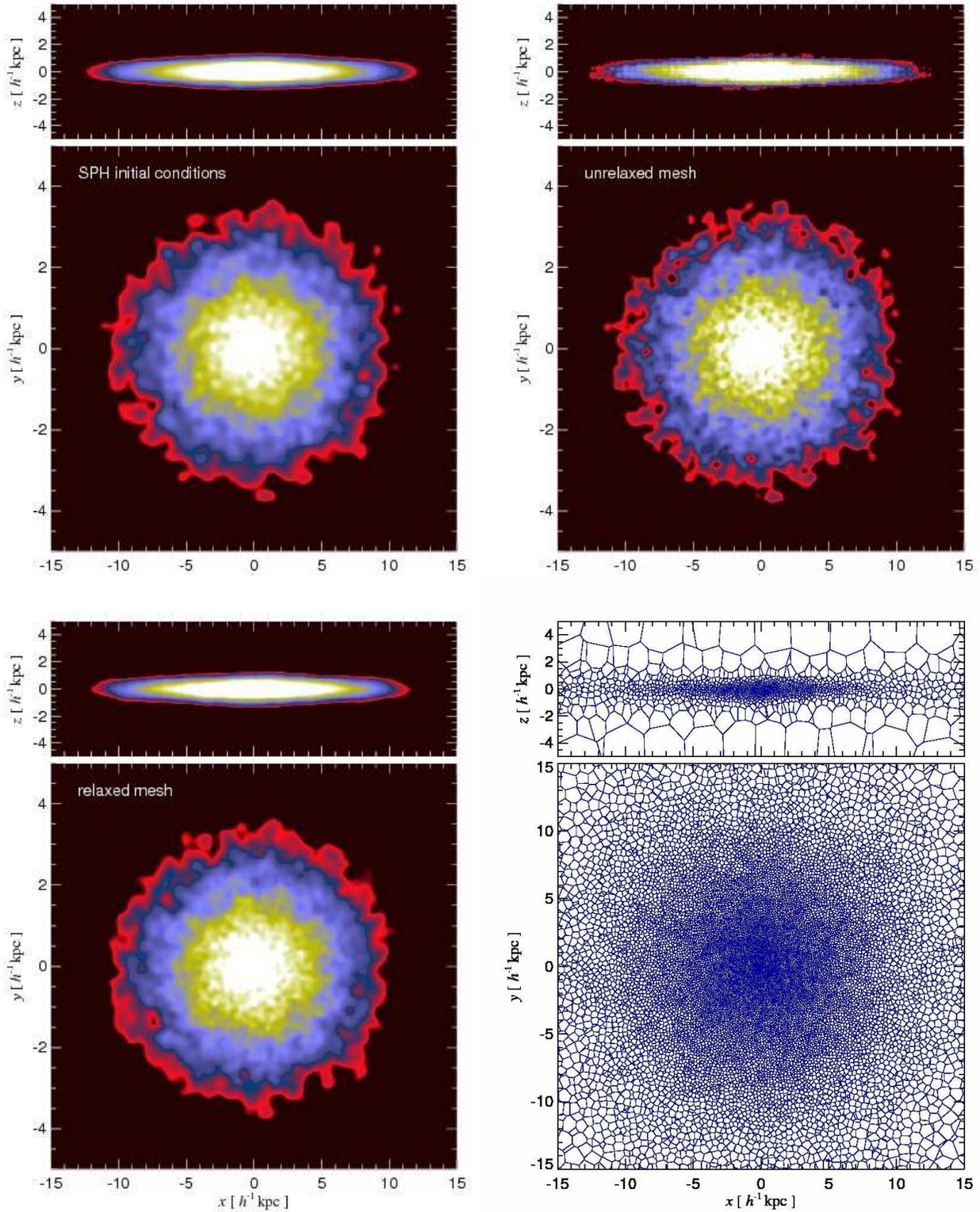
Figure 48. The top left panel shows the projected gas density in the original SPH particle distribution, which we adapt automatically to be used in the moving-mesh code. In the top-right panel, we show the resulting gas distribution in the Voronoi mesh that is created automatically based on the original SPH particle distribution. The lower left panel gives the density distribution after 32 mesh relaxation steps have been applied, which improves the mesh regularity and somewhat reduces the density fluctuations present in the original initial conditions. Finally, the lower right shows two sections through the three-dimensional Voronoi mesh corresponding to the lower left distribution.
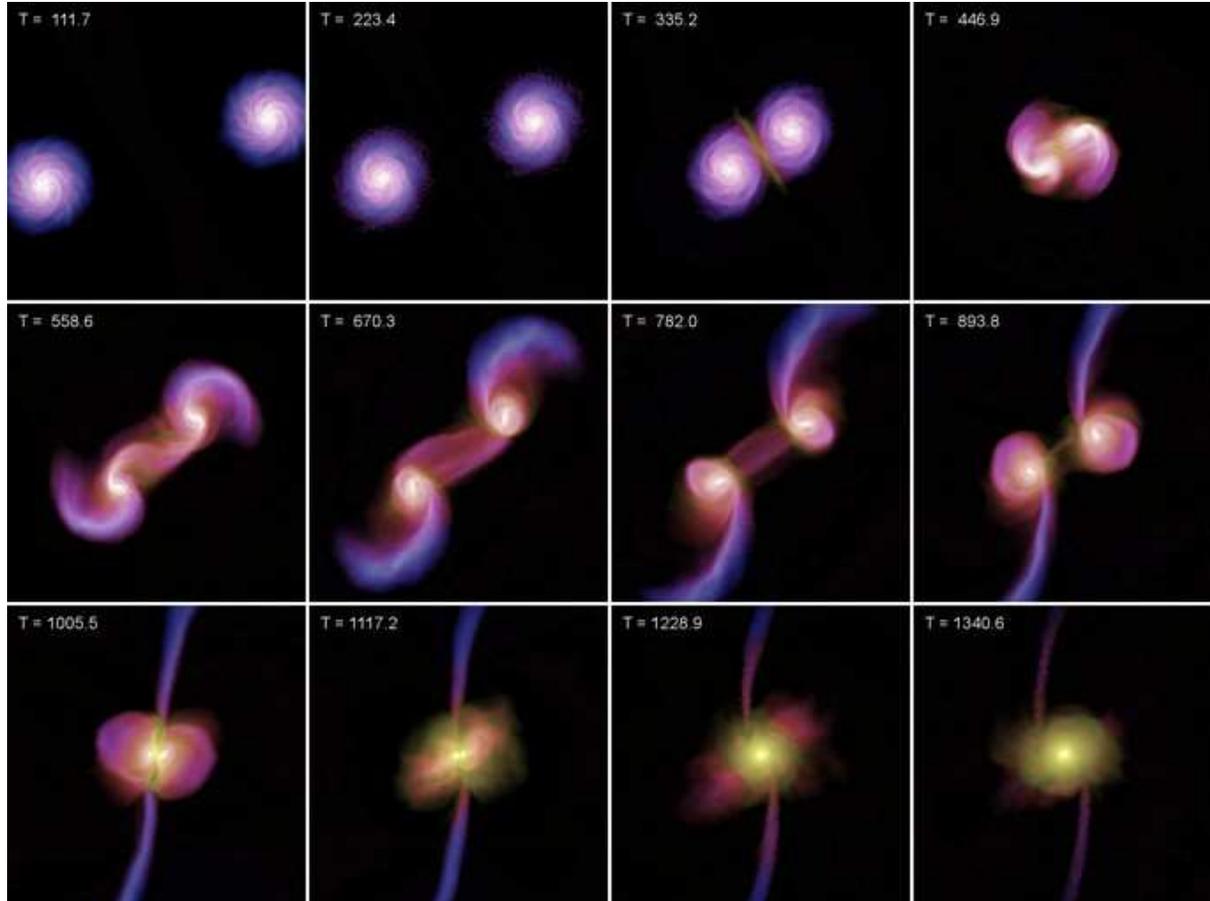
Figure 49. Time evolution of the projected gas density in a galaxy collision with non-radiative gas, calculated with the moving-mesh code AREPO. Each frame has a length of $160\,h^{-1}$kpc on a side, and the elapsed time since the start of the simulation is given in units of h^{-1}Myr. The brightness of each pixel encodes the projected gas surface density, and the colour hue the mass-weighted projected gas temperature.

tion. We start with a Cartesian grid with cells of size equal to the desired coarsest background resolution. We then fill in the gas particles of the SPH initial conditions one by one, requiring that a new set of 8 empty daughter cells is created whenever a particle falls into a leaf cell that already contains a particle. (Note that unlike in the ordinary tree construction of GADGET-2, the creation of empty cells is not prevented here.) Finally, we create mesh-generating points at the centres of all empty leaf cells. This procedure effectively creates an adaptively refined grid that follows the original SPH particle distribution.

(ii) We now assign the mass, momentum, and thermal energy of the original SPH particles to the new set of mesh-generating points. This is done by distributing these quantities to the new points in a conservative fashion, using the SPH kernel and the original SPH smoothing lengths, and by weighting each new point with the volume of its associated parent tree node. This produces new initial conditions that faithfully represent the gas distribution of the original SPH simulation, and which can be directly fed to the AREPO code.

(iii) As an optional step, we may now relax the created Voronoi mesh by moving the mesh-generating points with the technique described in subsection 4.2. If desired, this can also be used to downsample the mesh resolution to exactly match the particle number of the original SPH initial conditions. The spatial distribution of the mass density, momentum density and thermal energy density stays fixed in this step, only the mesh is moved by solving the advection equation. The mesh relaxes to a distribution where the factor $m_i/\tilde{m} + V_i/\tilde{V}$ is roughly constant for all the cells, see equation (69). Here $\tilde{m}$ is the original mean gas particle mass in the SPH initial conditions, and $\tilde{V}$ is the volume of the coarsest cell used in background grid. These values of $\tilde{m}$ and $\tilde{V}$ may then also be kept later on to steer the mesh motion during the dynamical evolution. We note that the numerical diffusion from the mesh advection in this step reduces Poisson noise in the initial particle set, if present, which is a welcome effect in this case.

In Figure 48, we illustrate the outcome of this procedure when applied to an isolated galaxy model. We selected SPH initial conditions created with the methods described in Hernquist (1993) and Springel & White (1999). The model has circular velocity $V_c = 160\,\mathrm{km\,s^{-1}}$, total mass $M_{200} = 9.52 \times 10^{11}\,h^{-1}\mathrm{M_\odot}$, and spin parameter $\lambda = 0.05$. Most of the mass is in an NFW-halo of concentration $c = 9.0$, represented with 50000 collisionless dark matter particles.
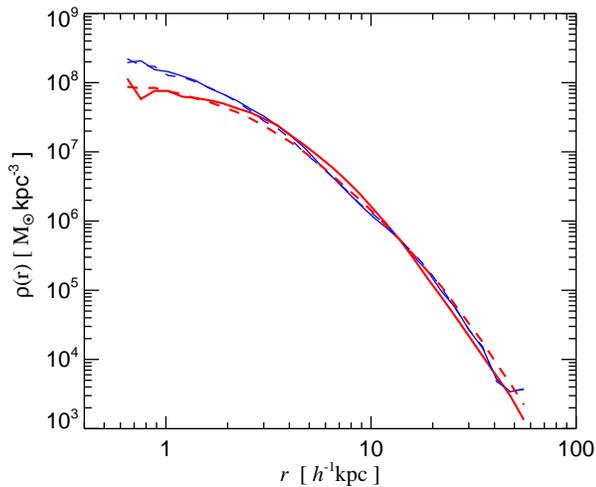
Figure 50. Spherically averaged density profiles of the remnant galaxy formed in the merger simulation carried out with the moving-mesh code AREPO, at time $2\,h^{-1}$Gyr after the start of the simulation. The thick red solid line is for the gas, the thin blue solid for the stars. Dashed lines give the result of a corresponding merger calculation carried out with the SPH-code GADGET-2. The fluctuation seen in the thick red line at small radii is due to counting statistics, as the number of cells there is small and each cell is counted in full towards the logarithmic bin in which its centre falls.

A fraction of $m_{\rm d} = 0.05$ of the mass is in a disk with an exponential surface mass profile with a scale-length of $R_d = 3.6\,h^{-1}$kpc, and a vertical scale height of $0.15 \times R_d$. Half of the disk mass is in a stellar disk, represented with 30000 collisionless particles, the rest in a gaseous disk of 30000 SPH particles. We enclosed the whole system in a box of size $1200\,h^{-1}$kpc on a side, and applied the initial conditions modification algorithm described above with a background grid of 32^3 cells. This increased the final number of mesh-generating points from 30000 to 109602.

In the top-left panel of Figure 48 we show the projected gas density in the original SPH particle distribution, projected with the adaptive SPH kernel. In the top-right panel, we show the gas distribution in the Voronoi mesh that is created after step (ii) in the above procedure has been completed. Here we projected the gas again with an SPH kernel, now seeking neighbours among the mesh-generating points. Clearly, the gas mass in the new mesh is localized well, as desired, but there is a large amount of high-frequency noise both in the local mesh structure and in the gas distribution. This noise is partially eliminated in step (iii), as shown in the bottom left panel, where we show the mass distribution after iterating the advection equation for 32 relaxation steps. Finally, in the bottom right panel we show planar sections through the three-dimensional Voronoi mesh corresponding to the relaxed initial conditions. The small pieces of cells that occasionally occur in these sections are corners from cells that are intersected far from their centres-of-mass.

The above procedures can also be readily applied to produce initial conditions that contain two galaxies on a collision orbit. We consider a prograde merger of two identical copies of the above galaxy model, placed at an initial sepa-

ration of $160\,h^{-1}$kpc, and set-up on a zero-energy orbit with impact parameter $2\,h^{-1}$kpc. In Figure 49 we show the time evolution of this galaxy merger simulated with the moving-mesh code. The baryons are treated as a non-radiative gas in this calculation. The galaxies freely fall together with increasing velocity until they undergo a first encounter. Tidal forces and shocks largely destroy the disks during this first passages, but the inertia of the galaxies lets them separate again. After sufficient braking from the dynamical friction of their dark matter halos, the galaxies turn around and fall together a second time. This is soon followed by complete coalescence, violent relaxation of the collisionless components, and virialization of the gas distribution. By time $\sim 2\,h^{-1}$Gyr, a reasonably relaxed spheroidal remnant galaxy has formed. We note that the images of Figure 49 have been created by ray-tracing through the Voronoi tessellation for each pixel, and integrating up the linearly reconstructed density field along all ray segments cells that intersect individual cells . This technique faithfully preserves the full information in the three-dimensional density field and does not rely on additional smoothing steps.

In Figure 50, we show the radially averaged density profiles of gas and stars of the final merger remnant, at time $2\,h^{-1}$Gyr. We compare the results with the outcome of the same merger calculation carried out with the SPH code GADGET-2. Interestingly, both the stellar and gas density profiles are extremely similar, even though there is a hint that the gas density profile is slightly more concentrated in the moving-mesh calculation in the outer parts of the halo, and the innermost gas density profile is a bit shallower. We have used our entropy-energy formalism with a Mach number threshold of $\mathcal{M}_{\rm thresh} = 1.1$ in this moving-mesh calculation, which has suppressed entropy production in very weak shocks. If this threshold is raised to $\mathcal{M}_{\rm thresh} = 1.3$, the central gas density increases somewhat, while without any such threshold it is substantially lowered, because in this case the cold gas in the disks already experiences significant heating from noise in the gravitational field prior to the actual collision of the two galaxies. Further work will be required to better understand the dissipation in the moving-mesh code in the presence of a collisionless particle component, and to establish the most accurate setting of $\mathcal{M}_{\rm thresh}$, or to find an alternative approach to suppress spurious dissipation in the finite volume approach when coupled to self-gravity and a collisionless N-body system.

10   DISCUSSION

We have introduced a novel moving-mesh hydrodynamical scheme that is second-order accurate both in space and time and does not require an artificial viscosity. The method is based on a finite volume discretization of the Euler equations on an unstructured mesh. The mesh is constructed as the Voronoi tessellation of a finite set of mesh-generating points, which are free to move during the time evolution. However, unlike in many other moving-mesh approaches, there are no mesh-tangling or mesh-twisting effects since the motion of the mesh-generating points induces a continuous deformation of the mesh, without the occurrence of 'bow-tie' cells or other topological artefacts. The freedom to move the mesh

with a nearly arbitrary flow field adds considerable flexibility to the method.

If the mesh-generating points are fixed, the method becomes effectively identical to an Eulerian code, formulated with an unsplit MUSCL-Hancock scheme on an unstructured grid. If the points are fixed and arranged on a Cartesian grid, the method becomes identical to an ordinary Eulerian code on a regular structured mesh. However, the most attractive mode of operation is obtained by tying the mesh motion to the local fluid velocity, in the simplest case making the velocities of the mesh-generators equal to the fluid velocities of the corresponding cells. In this Lagrangian mode, the dynamics becomes Galilean-invariant and benefits from the automatic adaptivity of Lagrangian approaches, which is advantageous for many problems of interest.

Conceptually, our method shares aspects of SPH and of Eulerian hydrodynamics. From SPH, it inherits the concepts of points as carriers of thermodynamic quantities and their spatial distribution sets the resolution in the flow. From Eulerian codes it inherits the concept of finite volume discretization of the Euler equations, and the Godunov approach to accurately estimate the exchange of conserved quantities across cell faces. On the other hand, our approach avoids some of the weaknesses of these two schemes. For example, it does not show the same level of noise and diffusiveness as SPH, and it avoids the Galilean non-invariance of Eulerian codes. In our view, this new synthesis of properties makes our new approach a very attractive technique, providing a better numerical accuracy for many problems compared with the alternative methods available thus far.

We note that our new method is significantly different from other approaches to improve SPH, such as, e.g. the approaches discussed by Inutsuka (2002), where SPH is combined with a Riemann solver. The important new concept in our method is the introduction of a well-defined mesh, while SPH by its very definition a mesh-free technique.

In this paper, we have described in detail the numerical and algorithmic approaches taken in our new cosmological code AREPO, ranging from parallel mesh-construction techniques in 2D and 3D, to spatial reconstruction and flux estimation techniques, as well as time integration with individual and adaptive schemes. We have shown that our new code performs very well on a wide range of test problems. We therefore consider it to be an attractive alternative to SPH or AMR codes used presently in cosmology, and argue that it has the potential to become the method of choice for a number of applications. We note, in particular, that our treatment of self-gravity should be more accurate and better suited for the problem of cosmic structure growth than that in the current generation of cosmological AMR codes.

We note that our new moving mesh method can also make use of many advanced concepts that have been developed for Eulerian codes, for example to deal with magnetic fields and radiative transfer. In particular, if constrained transport methods for ideal magnetohydrodynamics (MHD) can be adapted to a Voronoi mesh, this would provide the exciting possibility of constructing a Lagrangian MHD code. Another interesting idea is to apply the ideas outlined in this paper in the modelling of relativistic flows, which may yield a Lorentz invariant numerical scheme. Also, it seems possible to increase the order of our scheme by employing more sophisticated reconstruction steps, e.g. those known as weighted essentially non-oscillatory (WENO) schemes (e.g. Feng et al., 2004). However, the second-order approach followed here is probably best for cosmological structure formation, as the integration of the collisionless component is of second order only and involves a relatively noisy gravitational field.

ACKNOWLEDGEMENTS

REFERENCES

Agertz O., Moore B., Stadel J., et al., 2007, MNRAS, 380, 963
Ascasibar Y., Yepes G., Müller V., Gottlöber S., 2003, MNRAS, 346, 731
Athanassoula E., Misiriotis A., 2002, MNRAS, 330, 35
Balsara D. S., 1994, ApJ, 420, 197
Barnes J., Hut P., 1986, Nature, 324, 446
Barnes J. E., Hernquist L., 1992, ARA&A, 30, 705
Barth T., Ohlberger M., 2004, in Encyclopedia of Computational Mechanics, Volume 1, Fundamentals., edited by E. Stein, R. de Borst, T. Hughes, 439–474, John Wiley and Sons Ltd
Barth T. J., Jesperson D. C., 1989, AIAA Paper, 89-0366
Bate M. R., Burkert A., 1997, MNRAS, 288, 1060
Berger M. J., Colella P., 1989, Journal of Computational Physics, 82, 64
Bernardeau F., van de Weygaert R., 1996, MNRAS, 279, 693
Blandford D. K., Blelloch G. E., Cardoze D. E., Kadow C., 2005, International Journal of Computational Geometry & Applications, 15, 3
Blandford D. K., Blelloch G. E., Kadow C., 2006, in SCG '06: Proceedings of the twenty-second annual symposium on Computational geometry, 292–300, ACM, New York, NY, USA
Bowyer A., 1981, Comput. J., 24, 2, 162
Bryan G. L., Norman M. L., Stone J. M., Cen R., Ostriker J. P., 1995, Computer Physics Communications, 89, 149
Cignoni P., Montani C., Scopigno R., 1998, Computer-Aided Design, 30, 333
Clarkson K. L., 1992, in Proceedings of the 33rd Annual Symposium on Foundations of Computer Science, 387–395, IEEE Computer Society Washington, DC, USA
Colella P., Woodward P., 1984, Journal of Computational Physics, 54, 174
Cunningham A. J., Frank A., Varnière P., Mitran S., Jones T. W., 2009, ApJS, 182, 519
Dave R., Dubinski J., Hernquist L., 1997, New Astronomy, 2, 277
Di Matteo T., Springel V., Hernquist L., 2005, Nature, 433, 604
Dobkin D. P., Laszlo M. J., 1989, Algorithmica, 4, 3
Dolag K., Vazza F., Brunetti G., Tormen G., 2005, MNRAS, 364, 753
Dwyer R. A., 1987, Algorithmica, 2, 137
Edelsbrunner H., Mucke E. P., 1990, ACM Trans. Graph, 9, 66
Edelsbrunner H., Shah N. R., 1996, Algorithmica, 15, 223
Evrard A. E., 1988, MNRAS, 235, 911
Feng L.-L., Shu C.-W., Zhang M., 2004, ApJ, 612, 1
Frenk C. S., White S. D. M., Bode P., et al., 1999, ApJ, 525, 554
Fromang S., Hennebelle P., Teyssier R., 2006, A&A, 457, 371

Gerhard O. E., 1981, MNRAS, 197, 179

Gingold R. A., Monaghan J. J., 1977, MNRAS, 181, 375

Gnedin N. Y., 1995, ApJS, 97, 231

Goodman J., Hernquist L., 1991, ApJ, 378, 637

Gresho P. M., Chan S. T., 1990, International Journal for Numerical Methods in Fluids, 11, 621

Guibas L. J., Stolfi J., 1985, ACM Transactions on Graphics, 4, 74

Heitmann K., Lukić Z., Fasel P., et al., 2008, Computational Science and Discovery, 1, 1, 015003

Hernquist L., 1989, Nature, 340, 687

Hernquist L., 1993, ApJS, 86, 389

Hernquist L., Katz N., 1989, ApJS, 70, 419

Hopkins P. F., Hernquist L., Cox T. J., Di Matteo T., Robertson B., Springel V., 2006, ApJS, 163, 1

Hopkins P. F., Hernquist L., Cox T. J., Dutta S. N., Rothberg B., 2008, ApJ, 679, 156

Iapichino L., Adamek J., Schmidt W., Niemeyer J. C., 2008, MNRAS, 388, 1079

Iapichino L., Niemeyer J. C., 2008, MNRAS, 388, 1089

Inutsuka S., 2002, Journal of Computational Physics, 179, 238

Katz N., Weinberg D. H., Hernquist L., 1996, ApJS, 105, 19

Landau L. D., Lifshitz E. M., 1966, Hydrodynamik, Lehrbuch der theoretischen Physik, Berlin: Akademie-Verlag, 1966

Lee S., Park C.-I., Park C.-M., 2001, Parallel Processing Letters, 11, 341

LeVeque R. J., 1998, Journal of Computational Physics, 146, 346

LeVeque R. J., 2002, Finite volume methods for hyperbolic systems, Cambridge University Press

Liska R., Wendroff B., 2003, SIAM J. Sci. Comput., 25, 3, 995

Liu Y., Snoeyink J., 2005, Combinatorial and Computational Geometry, 52, 439

Lloyd S., 1982, IEEE Trans. Inform. Theory, 28, 129137

Lucy L. B., 1977, AJ, 82, 1013

Mavriplis D. J., 1997, Annual Review of Fluid Mechanics, 29, 473

Mignone A., Bodo G., Massaglia S., et al., 2007, ApJS, 170, 228

Mihos J. C., Hernquist L., 1996, ApJ, 464, 641

Mitchell N. L., McCarthy I. G., Bower R. G., Theuns T., Crain R. A., 2009, MNRAS, 395, 180

Monaghan J. J., 1992, ARA&A, 30, 543

Monaghan J. J., 1997, J. Comp. Phys., 136, 298

Mücke E. P., 1998, International Journal of Computational Geometry and Applications, 8, 255

Mücke E. P., Saias I., Zhu B., 1996, in SCG '96: Proceedings of the twelfth annual symposium on Computational geometry, 274–283, ACM, New York, NY, USA

Müller E., Steinmetz M., 1995, Computer Physics Communications, 89, 45

Murphy J. W., Burrows A., 2008, ApJS, 179, 209

Navarro J. F., Ludlow A., Springel V., et al., 2008, MNRAS, in press, ArXiv e-prints, 0810.1522

Negroponte J., White S. D. M., 1983, MNRAS, 205, 1009

Noh W. F., 1987, Journal of Computational Physics, 72, 78

Okabe A., Boots B., Sugihara K., Nok Chiu S., 2000, Spatial Tessellations, Concepts and Applications of Voronoi Diagrams, John Wiley & Sons Ltd, Chichester

Ollivier-Gooch C. F., 1997, Journal of Computational Physics, 133, 6

O'Shea B. W., Nagamine K., Springel V., Hernquist L., Norman M. L., 2005, ApJS, 160, 1

Owen J. M., Villumsen J. V., Shapiro P. R., Martel H., 1998, ApJS, 116, 155

Pelupessy F. I., Schaap W. E., van de Weygaert R., 2003, A&A, 403, 389

Pen U.-L., 1998, ApJS, 115, 19

Pfrommer C., Springel V., Enßlin T. A., Jubelgas M., 2006, MNRAS, 367, 113

Press W. H., Teukolsky S. A., Vetterling W. T., Flannery B. P., 1992, Numerical recipes in C. The art of scientific computing, Cambridge: University Press, 1992, 2nd ed.

Price D. J., 2008, Journal of Computational Physics, 227, 10040

Price D. J., Monaghan J. J., 2007, MNRAS, 374, 1347

Rasio F. A., Shapiro S. L., 1991, ApJ, 377, 559

Ryder W. J., 2000, Journal of Computational Physics, 162, 395

Ryu D., Ostriker J. P., Kang H., Cen R., 1993, ApJ, 414, 1

Saitoh T. R., Makino J., 2009, ApJL, 697, L99

Scannapieco E., Brüggen M., 2008, ApJ, 686, 927

Schaap W. E., van de Weygaert R., 2000, A&A, 363, L29

Schewchuk J. R., 1997, Discrete & Computational Geometry, 18, 305

Serrano M., Español P., 2001, Phys Rev E, 64, 046115

Shirokov A., Bertschinger E., 2005, ArXiv Astrophysics e-prints, astro-ph/0505087

Slyz A., Prendergast K. H., 1999, A&AS, 139, 199

Springel V., 2005, MNRAS, 364, 1105

Springel V., Di Matteo T., Hernquist L., 2005, MNRAS, 361, 776

Springel V., Hernquist L., 2002, MNRAS, 333, 649

Springel V., White S. D. M., 1999, MNRAS, 307, 162

Springel V., White S. D. M., Frenk C. S., et al., 2008, Nature, 456, 73

Springel V., Yoshida N., White S. D. M., 2001, New Astronomy, 6, 79

Stadel J., Potter D., Moore B., et al., 2009, MNRAS, 398, L21

Steinmetz M., Müller E., 1993, A&A, 268, 391

Steinmetz M., White S. D. M., 1997, MNRAS, 288, 545

Stone J. M., Gardiner T. A., Teuben P., Hawley J. F., Simon J. B., 2008, ApJS, 178, 137

Stone J. M., Norman M. L., 1992, ApJS, 80, 753

Strang G., 1968, SIAM Journal on Numerical Analysis, 5, 3, 506

Tasker E. J., Brunino R., Mitchell N. L., et al., 2008, MNRAS, 390, 1267

Thacker R. J., Couchman H. M. P., 2006, Computer Physics Communications, 174, 540

Toomre A., Toomre J., 1972, ApJ, 178, 623

Toro E., 1997, Riemann solvers and numerical methods for fluid dynamics, Springer

Trac H., Pen U.-L., 2004, New Astronomy, 9, 443

Trac H., Sills A., Pen U.-L., 2007, MNRAS, 377, 997

Truelove J. K., Klein R. I., McKee C. F., et al., 1998, ApJ, 495, 821

van de Weygaert R., 1994, A&A, 283, 361

van de Weygaert R., Schaap W., 2009, in Lecture Notes in Physics, Berlin Springer Verlag, edited by V. J. Martínez, E. Saar, E. Martínez-González, & M.-J. Pons-Bordería, vol. 665 of Lecture Notes in Physics, Berlin Springer Verlag, 291–413

van Leer B., 1984, SIAM J. Sci. Stat. Comput., 5, 1

van Leer B., 2006, Communications in Computational Physics, 1, 192

Wadsley J. W., Stadel J., Quinn T., 2004, New Astronomy, 9, 137

Wadsley J. W., Veeravalli G., Couchman H. M. P., 2008, MNRAS, 387, 427

Watson D. F., 1981, Comput. J., 24, 2, 167

White S. D. M., 1996, in Cosmology and Large-Scale Structure, edited by R. Schaefer, J. Silk, M. Spiro, J. Zinn-Justin, Dordrecht: Elsevier, astro-ph/9410043

White S. D. M., Rees M. J., 1978, MNRAS, 183, 341

Whitehurst R., 1995, MNRAS, 277, 655

Woodward P., Colella P., 1984, Journal of Computational Physics, 54, 115

Xu G., 1997, MNRAS, 288, 903

Zeldovich Y. B., 1970, A&A, 5, 84

Zingale M., Dursi L. J., ZuHone J., et al., 2002, ApJS, 143, 539